R1756

Final Report

A FUNDAMENTAL STUDY OF RESPIRATORY AIR FILTRATION

Grant # 1 RO1 OHO1485-01A1
Center for Disease Control
Public Health Service
U. S. Department of Health and Human Services

Volume 1

Report Prepared by:

Benjamin Y. H. Liu and Behzad Fardi
Particle Technology Laboratory
Mechanical Engineering Department
University of Minnesota
Minneapolis, Minnesota 55455

Submitted by:

Benjamin Y. H. Liu
Principal Investigator
Telephone: 612-625-6574

Particle Technology Laboratory Publication No. 680

September, 1988

50272-101

REPORT DOCUMENTATION PAGE	1. REPORT NO.	2.	3. Recipient's Accession No. PB89 152904/AS
4. Title and Subtitle A Fundamental Study of Respiratory Air Filtration, Volume 1			5. Report Date 88/09/00
			6.
7. Author(s) Liu, B. Y. H., and B. Fardi			8. Performing Organization Rept. No.
9. Performing Organization Name and Address Mechanical Engineering Department, University of Minnesota, Minneapolis, Minnesota			10. Project/Task/Work Unit No.
			11. Contract (C) or Grant(G) No. (C) (G) R01-OH-01485
12. Sponsoring Organization Name and Address			13. Type of Report & Period Covered
			14.

15. Supplementary Notes

16. Abstract (Limit: 200 words) The purpose of this grant was to study characteristics of particulate air filters used in respiratory protective devices. In particular, efforts were made to determine the overall efficiency of the filters as a function of particle size and as a function of the velocity of air flow through the filter. A determination was also made of the resistance of the filter media to the flow of air. This specific report contained the first four chapters of the full report and dealt with the history of respirator development (types of respirators, types of hazardous particulates, respirator approval tests, and previous work on respirator filter testing); reviewed electrostatic filtration; presented experimental work relating to this grant including a description of the test chamber, particle generation devices, particle size distribution measuring devices, test chamber performance and experimental procedure; and offered a theoretical study consisting of numerical calculations. An apparatus for testing respiratory air filters was designed. For all filters tested, a unique and well defined particle size was found at which the aerosol penetration through the filter was a maximum and the filter efficiency was a minimum. The particle size which had the most penetration varied between 0.1 and 0.4 micrometers with the corresponding efficiency ranging from 55 to 98.9 percent. Efficiency was dependent upon both the specific filter being studied and the flow rate through that filter.

17. Document Analysis a. Descriptors

b. Identifiers/Open-Ended Terms NIOSH-Publication, NIOSH-Grant, Grant-Number-R01-OH-01485, End-Date-08-30-1986, Respirators, Personal-protective-equipment, Respiratory-protective-equipment, Filter-materials

c. COSATI Field/Group

18. Availability Statement	19. Security Class (This Report)	21. No. of Pages 221
	22. Security Class (This Page)	22. Price

(See ANSI-Z39.18) *See Instructions on Reverse*

OPTIONAL FORM 272(4-77)
(Formerly NTIS-35)
Department of Commerce

Summary

This report is being submitted as the final report for grant # 1RO1 OHO1485-01A1 from the Center for Disease Control for a research project entitled "A Fundamental Study of Respiratory Filtration." The project covered the period of September 1, 1984 through December 31, 1987.

The objective of the program was to study the characteristics of particulate air filters of the type used in respiratory protection devices. The study was concerned with the theoretical and experimental investigation of respirator air filters to determine the overall efficiency of the filters as a function of particle size and as a function of the velocity of air flow through the filter. In addition, the resitance of the filter media to flow was also determined.

During the first year of the program, an apparatus for testing respiratory air filters was designed, constructed and partially tested. Further experimental development of the apparatus took place during the second year and the developed apparatus was then used to determine the efficiency characteristics of several commercially available respirator air filters. In addition to the complete respirator air filter units, measurement was als made on flat-sheet filter media in order to gain a better understanding of respiratory air filtration without the complication of the more complicated filter sturcture inherent in a completed unit. The methodology and the results of measurement are described in the report. The experimental results indicate that for all respirator filters tested, there is a unique and well defined particle size at which the aerosol penetration through the

filter is a maximum and the filter efficiency is a minimum. This most penetration particle size was found to vary between 0.1 and 0.4 μm. The corresponding efficiency was found to vary between 55% and 98.8% depending on the specific respiratory filter being studied and the flow rate through the filter.

In addition to the experimental measurements, a concurrent theoretical analysis of respiratory filtration was made. A numerical simulation model was developed and applied to the study of particle collection by electrically charged filter fibers. Calculations were made on a Cray 2 Supercomputer on the flow and particle collection characteristics of the filters. Particular attention was paid to the electret filter media consisting of rectangular electret fibers. Calculation was made on the particle collection characteristics of the filter fibers, taking into account various collection mechanisms including diffusion, interception and electrical forces, both Coulombic and induced forces.

i.e

A Fundamental Study of Air Filtration For Respiratory Protection

A THESIS

SUBMITTED TO THE FACULTY OF THE GRADUATE SCHOOL

OF THE UNIVERSITY OF MINNESOTA

BY

BEHZAD FARDI

IN PARTIAL FULFILLMENT OF THE REQUIREMENTS

FOR THE DEGREE OF

DOCTOR OF PHILOSOPHY

AUGUST, 1988

Abstract

An experimental study of filtration performance of several commercially available, disposable respirators was conducted in conjunction with a theoretical study of filtration characteristics of charged rectangular (electret) fibers.

The experimental study involved measuring penetration of monodisperse DOP and NaCl Aerosols through five different respirators and a flat filter medium at a flow rate of 16, 28, or 48 liters per minute. The respirators were all approved by NIOSH for protection against dust, mist, and/or fume particulate hazards. The test particles ranged in diameter from 0.035 to 4.0 μm.

The penetration measurements were made by a condensation nucleus counter, an aerodynamic particle sizer, and a laser optical particle counter for purposes of comparing measurement results of different instruments. The penetration measurements obtained by the above instruments were found to be in reasonable agreement in the overlapping region of the particle size range of the instruments.

The peak penetration through the repirator filters was found to range from approximately 1.2% to 30% at 16 L/m, 3.5% to 37% at 28 L/m, and 6% to 45% at 48 L/m. The most penetrating particle size was found to lie in the 0.1 to 0.4

μm diameter range. Further, no significant difference in penetration characteristic of NaCl and DOP particles was found.

On the other hand, the theoretical study consisted of numerical calculation of flow field in a staggered array of rectangular fibers arranged perpendicular to the flow direction followed by calculation of collection efficiency of a single electret fiber of different aspect ratios by the diffusion and interception mechanisms as well as Coulombic and induced forces. The values considered for the rectangular fiber aspect ratio ranged from 0.1 to 10.

Collection efficiency of a single electret fiber was found to be proportional to -2/3, 1.55, 0.92, and 0.47 powers of Peclet number, interception parameter, and Coulombic and induced force parameters, respectively, when individual collection mechanism prevailed. Further, the single electret fiber collection efficiency due to pure diffusion was found to be proportional to the square root of the fiber aspect ratio while, that due to interception was found to decrease as the fiber aspect ratio was increased to a value of 5, beyond which the efficiency became virtually independent of the fiber aspect ratio. The Coulombic and induced single fiber efficiency calculations were carried out for fiber aspect ratios of 1/4 and 4/1 which are common values for manufactured electret fibers.

The viscous drag on rectangular fibers was also calculated and expressed in dimensionless form. It was found that the dimensionless drag values on rectangular fibers with aspect ratios greater than 1 were virtually independent of the fiber aspect ratio and could be approximated closely by the Kuwabara expression for cylindrical fibers while, for values below or equal to 1, the dimensionless drag was found to be a strong function of the fiber aspect ratio.

Further, the dependence of the single electret fiber efficiency on the solid-volume fraction of the staggered model was investigated also and the calculation results indicated that the single fiber capture efficiency was proportional to 0.778, 0.54, and 0.15 powers of the solid-volume fraction for the diffusion, interception and Coulombic force interaction mechanisms, respectively, when individual mechanism prevailed.

Acknowledgements

I would like to express my gratitude to my advisor, Professor Benjamin Y. H. Liu, for his support and guidance throughout the course of my thesis work. Dr. Liu allowed me to grow from an inexperienced researcher to an independent, confident, and capable researcher and for that, I am very grateful to him.

I would also like to thank Mr. Reza Sadjadi for assisting me in designing and Mr. Karl Lovgren for building the experimental apparatus. Special thanks are due to Professor Suhas V. Patankar for the use of his numerical program and Dr. Kanchan Kelkar for assisting me with the program.

A very special thanks is extended to my family whose support, love, and encouragement made the pressure and frustrations associated with a thesis work more bearable.

The support of this work by the Center for Disease Control-National Institute of Occupational Safety and Health is greatly appreciated.

TABLE OF CONTENTS

List of Tables

List of Figures

Nomenclature

a_c	Radius of Kuwabara cell, cm or μm
a_E	Coefficient of discretization equation
a_f	Fiber radius, cm or μm
a_N	Coefficient of discretization equation
a_p	Particle radius, cm or μm
a_P	Coefficient of discretization equation
a_S	Coefficient of discretization equation
A	Dimensionless parameter defined by equation (2.15)
A_i	Surface area of the ith control volume adjacent to the fiber
A_k	Coefficient as defined by equation (4.7a)
$A_1 \ldots A_N$	Dimensional quantities
b	Length of a rectangular fiber, cm or μm
b	Constant term in discretization equation
B_k	Coefficient as defined by equation (4.7b)
B_m	Particle mechanical mobility as defined by equation (2.17), cm/dyne.s
c	Slip correction
C	Volumetric concentration
C_k	Coefficient as defined by equation (4.7c)
d	Characteristic length, cm or μm

d_c	Cylinder diameter, cm or μm
d_f	Fiber diameter, cm or μm
d_p	Particle diameter, cm or μm
D	Particle diffusion coefficient, cm^2/s
D_d	Droplet diameter, cm or μm
D_f	Cylindrical fiber diameter, cm or μm
D_{gn}	Geometric number mean diameter
D_h	Hydraulic diameter of a rectangular fiber as defined by equation (4.38)
D_k	Coefficient as defined by equation (4.7d)
e	Elementary unit of charge = 4.8×10^{-10} stC
E_o	Electric field of uniform intensity
E_r	Radial electric field component
E_θ	Circumferential electric field component
E	Electric field intensity function
E_{r_i}	Radial electric field intensity due to the ith line charge
E_{x_i}	Electric field intensity component along the x-axis of the cartesian coordinate system due to the ith line charge
E_x	Electric field intensity component along the x-axis

$\mathcal{E}_{y_i}$ Electric field intensity component along the y-axis of the cartesian coordinate system due to the ith line charge

E_y Electric field intensity component along the y-axis

f Frequency, Hz

f_m Figure of merit

F Drag per unit lenght of fiber, dyne/cm

F_C Coulombic force, dyne

F_{C_x}, F_{C_y} x- and y- components of Coulombic force

F_d Drag on a particle, dyne

F_{d_x}, F_{d_y} x- and y- components of particle drag

F_{form} Net form or pressure drag on a cylindrical fiber, dyne

F_I Induced force, dyne

F_{I_x}, F_{I_y} x- and y- components of induced force

F_r Electric force between a point charge and an infinite plane

F_{shear} Net shear force on a cylindrical fiber, dyne

F^* Dimensionless drag as defined by equation (4.23)

Fu Fuchs number = $\frac{2a_f}{l}$

G Dimensionless parameter as defined by equation (2.16)

h	Half the distance between centers of two successive fibers along the flow direction, cm or μm
H_r	Radial electric force component between an uncharged particle and a fiber in the presence of an external electric field, dyne
H_θ	Circumferential electric force component between an uncharged particle and a fiber in the presence of an external electric field, dyne
i, j	Integer variables
J	Total number of particles deposited on a fiber due to pure diffusion per unit time
j_D	Number of particles deposited on a fiber due to pure diffusion per unit time and fiber surface area
K	Hydrodynamic factor of Kuwabara flow field as defined by equation (2.41)
K_m	Mass transfer coefficient
Kn	Knudsen number = $\frac{\lambda}{a_f}$
k	Boltzmann's constant = 1.38×10^{-16} dyne.cm/K^0
κ	Particle dielectric constant
l	Distance between centers of two successive fibers, cm or μm
l_t	Total length of fibers per unit filter area, cm^{-1}
L'	Length of the precipitating electrode in the electrostatic classifier, cm
L_f	Filter thickness, cm
L	Periodic length, cm or μm
m	Integer variable

$\mathcal{N}$	Dimensionless parameter as defined by equation (2.25)
n	Integer variable
n_c	Number of line charges on half of an electret fiber
n_p	Number of elementary unit charges on a particle
n	Total particle count
N	Particle number concentration, #/cm^3
N_o	Free stream particle number concentration, #/cm^3
N_C	Dimensionless Coulombic force parameter as defined by equation (4.116)
N_I	Dimensionless induced force parameter as defined by equation (4.117)
N_i	Indicated particle number concentration, #/cm^3
N_{0q}	Dimensionless image force parameter as defined by equation (2.3)
N_{Qq}	Dimensionless electrostatic force parameter as defined by equation (2.29)
N_{Q0}	Dimensionless electrostatic force parameter as defined by equation (2.30)
N_{pq}	Dimensionless electrostatic force parameter as defined by equation (2.37)
N_{p0}	Dimensionless electrostatic force parameter as defined by equation (2.38)
N_R	Interception parameter = $\frac{a_p}{w/2}$

N_t	True particle number concentration, #/cm^3
p	Perimeter of half of an electret fiber
p	Pressure
p_∞	Constant of integration
P	Periodic pressure
P'	Pressure correction function
Pe	Peclet number = $\frac{U_o D_h}{D}$ or $\frac{u_o R}{D}$ or $\frac{u_o w}{D}$
Δp	Pressure drop across fibrous filter
Δp_c	Pressure drop across clean respirator filter
Δp	Pressure drop across a flow metering nozzle, lbf/ft^2
q	Particle charge, C
q_a	Polydisperse aerosol flow rate entering the electrostatic classifier, cm^3/s
q_c	Clean sheath air flow rate, cm^3/s
q_s	Monodisperse aerosol flow rate exiting the electrostatic classifier, cm^3/s
Q	Charge per unit length of fiber, C/cm
Q_s	Aerosol sampling flow rate, cm^3/s
Q_t	Total aerosol flow rate, L/m
ℓ	Liquid flow rate, cm^3/s
r	Radial position

r_1, r_2 Inner and outer radii of the electrostatic classifier, cm

r_{p_i} Radial position from the ith positive line charge

r_{n_i} Radial position from the ith negative line charge

r^* Dimensionless radial position = r/w

R Cylinder radius, cm or μm

Re Reynolds number based on the hydraulic diameter of a rectangular fiber = $\frac{U_o D_h}{\nu}$

Re_D Reynolds number based on the cylindrical fiber diameter = $\frac{U_o D_f}{\nu}$

Re_h Reynolds number based on h = $\frac{U_o h}{\nu}$

s Position coordinate along an electret fiber contour

s^* Dimensionless position coordinate along an electret fiber contour = s/p

S Source term in discretization equation

S_C Constant of linearized source term expression

S_P Slope of linearized source term

Sh Sherwood number = $\frac{K_m D_h}{D}$

t Time parameter

t^* Dimensionless time parameter = $\frac{t}{w/U_o}$

t_s	Sampling time, s
T	Absolute temperature, K^o
u	x- component of fluid velocity
u_r	Radial velocity component
u_θ	Circumferential velocity component
u^*	Guessed velocity field
u^*	Dimensionless x- component of fluid velocity $= u/U_o$
u'	Correction velocity field
U_o	Mean fluid velocity at the calculation domain entrance
u_o	Free stream fluid velocity
V	Voltage, volt
v	y- component of fluid velocity
v^*	Guessed velocity field
v'	Correction velocity field
v_p	Particle velocity
v_{px}	x- component of particle velocity
v_{py}	y- component of particle velocity
v^*	Dimensionless y- component of fluid velocity $= v/U_o$
v^*_{px}	Dimensionless x- component of particle velocity $= v_{px}/U_o$

v^*_{py}	Dimensionless y- component of particle velocity $= v_{py}/U_o$
W	Coefficient as given in equation (2.43)
w	Width of a rectangular fiber, cm or μm
x	Position coordinate in the cartesian coordinate system
X	Coefficient as given in equation (2.42)
x^*	Dimensionless position coordinate = x/w
x_{p_i}, y_{p_i}	Position coordinates as shown in Figure 4.18
x_{n_i}, y_{n_i}	Position coordinates as shown in Figure 4.18
y	Position coordinate in the cartesian coordinate system
Y	Coefficient as given in equation (2.42)
y^*	Dimensionless position coordinate = y/w
y_c	Starting y-coordinate of particle critical trajectory
Z	Coefficient as given in equation (2.42)
Z_p	Particle electric mobility, $cm^2/V.s$
ϵ_c	Cylinder dielectric constant
ϵ_f	Fiber dielectric constant
ϵ_p	Particle dielectric constant
ϵ_o	Permittivity of free space
α	Solid-volume fraction
β	Dimensionless parameter as defined by equation (2.20)

$\bar{\beta}$	Dimensionless parameter as defined by equation (2.21)
$\hat{\beta}$	Pressure drop gradient
λ	Mean free path of gas molecules
λ'	Function of rectangular fiber aspect ratio
δ	Diffusion boundary layer thickness
ν	Kinematic viscosity
μ	Dynamic viscosity
ϕ	General dependent variable
δx	Distance between adjacent grids in the x-direction
δy	Distance between adjacent grids in the y-direction
σ	Charge per unit surface area of fiber, C/cm^2
σ_g, σ_{gn}	Geometric standard deviation
σ_r	Relative standard deviation
ρ	Fluid density
ρ_a	Air density at atmospheric conditions, lbm/ft^3
Γ	General diffusion coefficient
ϕ	General dependent variable
ψ	Stream function
ψ_{cr}	Streamline value of the critical streamline

ω	Vorticity function
τ_d	Particle residence time in the viewing volume of the condensation nucleus counter = 35 μs
$\tau_{r\theta}$	Shear stress
$\pi_1 \ldots \pi_n$	Dimensionless π parameters
η	Fiber or cylinder capture efficiency
η_D	Single electret fiber efficiency due to pure diffusion
η_{D_h}	Modified single electret fiber capture efficiency as defined by equation (5.3)
η_E	Single electret fiber efficiency due to electrostatics
η_E^C	Single electret fiber efficiency due to Coulombic forces
η_E^I	Single electret fiber efficiency due to induced forces
η_R	Single electret fiber efficiency due to interception
η_s	Single fiber capture efficiency
$\aleph$	Function of α

Chapter 1

HISTORY OF RESPIRATORS DEVELOPMENT

Respirators, designed to protect the wearer from inhalation of harmful dust, gas, and vapors, have been used in various forms for many centuries. According to the brief review of the history of respirator development given by Pritchard (1976), the earliest reference to the use of a face cover for protection against lead-oxide fumes was made by Pliny the Elder who lived 23 to 79 A.D. But the ancestors of the today's modern respirators started to appear in the 1700's as people began to realize the need for protection against various harmful dusts. It was, however, the industrial revolution of the 1800's which led to a rapid progress in the design and development of more sophisticated respirators to provide a safer protection to the miners.

In 1814, Brise' Fradin recorded the first filter respirator as a box filled with cotton and attached to a breathing tube which would go into the mouth. The respirator was tested against mercury fumes which were known to be dangerous to gilders. In 1823, C.A. Deane developed a "smoke jacket" for firemen, by which the clean air could be supplied with bellows attached to a breathing hose. A great improvement in the design of the fibrous filters was

achieved by the discovery of the Brownian motion of small airborne particles by Robert Brown in 1827. In 1849, a dust respirator designed to filter dusts or harmful substances from the inhaled air was patented in the United States. The filter was made of woolen fabric and was fitted to either the nose or the mouth. In 1870, John Tyndall ,the famous English physicist, constructed a "fireman's respirator" similar in many ways to the gas masks used during World War I. The respirator consisted of a leather smoke cap to cover the head and a brass canister to hold the filter materials for cleaning the inhaled air. However, the most rapid advances in the respirator and filter design were made during World War I in an attempt to counter the German use of poisonous gases and highly toxic particulate matter on the battlefield (Pritchard (1976)).

After the war the research continued toward more scientific understanding of the filtration mechanisms and thus, making better use of them in the filter designs.

The first efforts to study filtration scientifically were made in Germany, where Albrecht in 1931 and Kaufmann in 1936 made original approaches to the theory of the mechanism of aerosol filtration by fibrous pads. However, a major breakthrough in the filter design was the development of the wool resin-impregnated filter by Hansen in 1930. He found great improvement in the collection efficiency of a wool

filter after the filter was powdered with charged resin particles. The advantage of his filter over the others was its high efficiency and low breathing resistance in comparison with the standards of that time.

These filters were later used in the military respirators by Danish, Dutch, French, and Italians by 1933 and the British used them in the civilian respirators in 1943. Since then, resin filters have been used a great deal in various applications.

The recent discovery of the so-called electrets, permanently charged dielectrics, and their development in the form of fibers have resulted in the production of new types of filters, commonly known as the electret filters. These filters contain fibers with much higher charge density than the resin-impregnated wool fibers and give stable performance at high temperature and humidity environments. On account of their high efficiency and low breathing resistance, the electret filters are increasingly used as the respirator filters. A detailed discussion on the characteristics and construction of the electret filters is given later.

Recent developments in respirators have been more associated with prevention of seal leakage and general wearing comfort than with the intrinsic efficiency of the filter itself, since this is no longer the limiting factor

in performance. Today, respirators come in a variety of shapes and designs to provide protection against variety of hazardous solid or liquid particulates as well as, different gas and/or vapors. Below, an overview of the types of available respirators and their intended applications is presented.

1.1 Types of Respirators

Modern respirators come in a variety of shapes and configurations to protect the wearer against inhalation of harmful particulates, as well as gas and/or vapors. In general, the repirators can be divided into two major categories, the air purifying and the atmosphere supplying respirators. In the case of the former, the contaminated surrounding air is drawn through the air purifying media, filter pads in the case of particulates and/or gas and vapor absorbing agents in the case of hazardous gas and vapors, prior to being supplied to the face mask. This type of respirator can be further divided into powered and non-powered type. With powered air purufying respirators, the surrounding air is drawn by a battery-operated blower through an absorbing medium and supplied to the face mask under a positive pressure, thus minimizing the amount of air leaking through the face seal during inhalation. With the

non-powered air purifying respirators, however,the purified air is supplied to the face mask by the negative pressure created during inspiration. Because of this negative pressure, maintaining a good seal between the face and the respirator mask is essential to providing adequate protection to the wearer. A common example of this type of respirator is the single-use or disposable respirator which is primarily used for protection against various kinds of particulates. Some of the air purifying respirators are also equipped with an exhaust valve to facilitate the passage of exhaled air back to the atmosphere.

In the case of the atmosphere-supplying respirator, the respirable air is supplied to the face mask under positive pressure from a source other than the surrounding atmosphere which may be oxygen-deficient and/or contain contaminants of great hazard to the human health even in small dosages. These respirators come in variety of designs and configurations depending on the nature of the contamination and intended application and like the air purifying respirators, can be divided into two categories, self-containing breathing apparatus and air supplied. In the case of the former, the whole system of the respirable air supply is carried by the wearer, while in the case of the latter, the air is supplied to the face mask by means of a hose from a blower or a compressed air reservoir under

controlled pressure and flowrate.

There are further sub-classifications for each of the above respirators according to their design and intended applications. A detailed review of the types of the respirators and their classification, as shown in Table 1.1, is given by Liu and Japuntich (1987).

1.2 Types of Hazardous Particulates

Most of the commercially-available respirator filters have been recommended for use against specific type(s) of the hazardous particulates. Liu and Japuntich (1987) have defined the general types of the particulate hazards, against which protection is necessary, as follows:

"Dust: Solid, mechanically produced (grinding, drilling, sanding, blasting, etc.) particles of sizes from sub-micrometer to tens of micrometers which can cause lung disease such as silicosis (silica), chronic irritation (acids) and allergies (pollen spores), including systemic poisons (cadmium) and carcinogens (asbestos, radioactive particles).

Mists and Sprays: liquid particles produced by condensation (mists) or mechanical means (spray). The particles may

Table 1.1 General classification of respirators according to their design and intended application (Liu and Japuntich (1987))

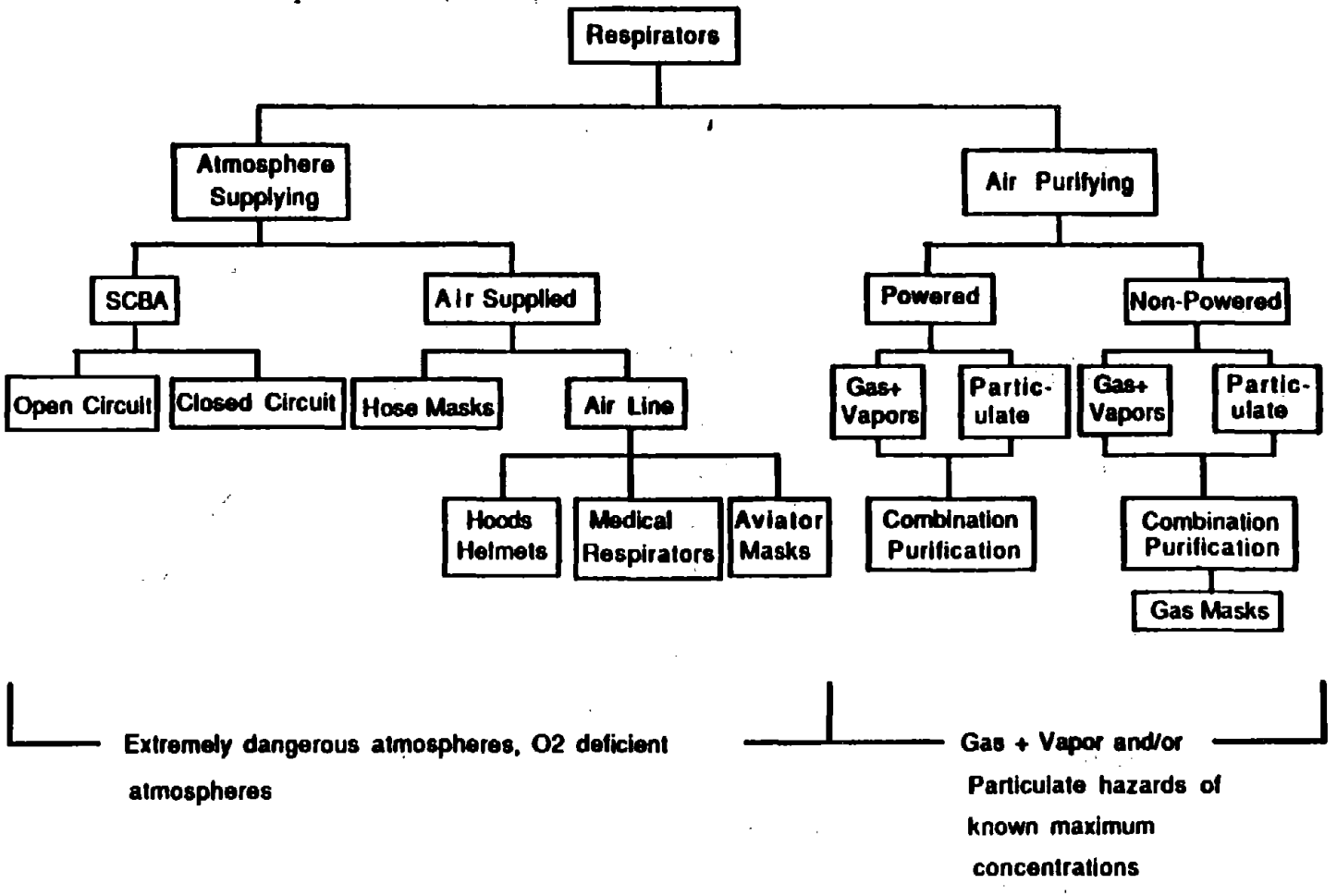

range in size from the sub-micrometer to a few micrometers and can cause respiratory illness such as major chemical irritation (smoke containing acidic condensate), systemic poisoning (spray paint) and chronic respiratory ailments (cigarette smoke, smog).

Fumes: solid particles produced by condensation, generally of metal or metal oxides with diameters in the sub-micrometer range and can cause systemic poisoning (lead welding fumes) or chills followed by fever (zinc or copper fumes)."

The respirator filter media used for removal of the above mentioned particulate matter from the inhaled air are typically made of fine fibers, approximately 2 μm in diameter or smaller depending on the type of particulate hazard, to provide moderate to high filtration efficiency. Besides, fibers of some respirator filter media are charged so that the filter mats can be made much less dense than the conventional fibrous mats, thus offering less resistance to air flow without loss of efficiency in capturing submicron particles.

1.3 Respirator Approval Tests

Prior to the designation of the Bureau of Mines in 1918, as the agency responsible for testing and approving satisfactory respiratory protection devices, there were no reliable data available on the performance of such devices at the time and the workers in the mines and other hazardous industrial atmospheres could risk their health and life by using these devices whose level of protection was not known.

On March 5, 1919, the Bureau initiated the use of Test Schedule 13, which covered testing and approval of self-contained Breathing Apparatus. The first Bureau approval was granted for this type of respirator on January 15, 1920. The Bureau played an important role in the development of the army gas mask and on the basis of this experience, the Bureau issued Schedule 14 for gas masks in May, 1919. Subsequently, the demands for performance requirements for other types of respiratory protection devices led to the issuance of Schedule 19 for hose masks in 1927; Schedule 21, for filter type dust, mist, and fume respiratiors in August, 1934; and Schedule 23 for chemical cartridge organic vapor respirators in November, 1944. These Schedules have been reviewed and revised as necessary to correlate with advancing respirator technology. The

latest revisions of the schedules are covered in Title 30, code of federal regulations, Part 11.

In 1971, the responsibility for testing and approving respirators was shifted to the National Institute of Occupational Safety and Health (NIOSH), which performs the tests according to the procedures and criteria presented in Part 11. The results are then reviewed by the Mine Safety and Health Administration (MSHA) and NIOSH, which may grant an approval. The approval label on a respiratory protective device is a guarantee that the device, if maintained in approved conditions will offer safety and protection to the wearer in its intended application.

Since the focus of the present study is on the filtration characteristics of the single-use filter media used in manufacturing of disposable dust, mist and/or fume respirators, only those NIOSH test procedures related to such respirator filters are briefly described here as follows (for detail description, reference is made to the sub-part K of Part 11 (Appendix A)):

The NIOSH approval testing of the air-purifying respirator filters, in general, involves a special mask holder inside a test chamber containing a known concentration of a test aerosol and drawing air through a respirator filter at continuous or cyclic flowrates for a

fixed period of time. The total amount of unretained test suspensions in samples taken during the test is measured and the resistance to the air flow is determined before and after the test. If the penetration and the resistance values are within allowable limits, the filter will be approved for protection against hazardous particulates of type similar to that of the test aerosol. A respirator submitted to NIOSH by its manufacturer for approval against more than one particulate hazard should comply with test requirements of each particulate hazard requested in order to be approved.

The test aerosols include silica dust, silica mist, lead-oxide fumes and DOP mist, each with specific size distribution. The silica dust and mist aerosols in the test chamber are required to have a geometric mean diameter of 0.4 to 0.6 μm with a geometric standard deviation of approximatley 2. The concentration of the silica dust or silica mist inside the chamber is maintained at about 55 or between 20 to 25 milligrams per cubic meter of air, respectively, over duration of the test. As for the size distribution of fume particles, there is no information given by NIOSH but Japuntich and Johnson (1983) generated lead-oxide fume particles in a test set-up similar to that of NIOSH and measured and presented results on the effect of air relative humdity in the test chamber on the geometric mean diameter and standard

deviation of the fume particles. Their measurements showed an average geometric mean diameter and a σ_g of approximately 0.05 μm and 2.0, respectively, over relative humidities ranging from 30% to 65%. The concentration of the lead-oxide fume particles in the NIOSH filtration test is maintained between 15 to 20 milligrams per cubic meter of air over duration of the test.

The DOP test which is designed for testing of high efficiency filters, involves sampling air from an atmosphere containing a DOP concentration of about 100 microgram per liter of air through non-powered air purifying respirators at 32 and 85 liters per minute and powered air-purifying respirators at 115 and 170 liters per minute. The maximum penetration of DOP aerosol should not exceed 0.03% for each test.

The sampling time for each test is different for non-powered and powered air-purifying respirators. For the case of the former, the sampling time is 90 minutes for the silica dust test, 312 minutes for the silica mist and lead-oxide fume tests, and 5 to 10 seconds for the DOP test. For the case of the powered respirators, the sampling time is 4 hours for the silica dust and mist and lead-oxide fume tests.

A summary of the NIOSH approval procedures and criteria for the air-purifying respirator filters has been given by

Luxon (1973) in a tabulated form.

1.4 Previous Work on Respirator Filter Testing

One of the earliest and most extensive evaluations of the filter efficiency of dust respirators was done by Katz et al. (1926a) in the Bureau of Mines, where a number of firmly sealed dust respirators made of different filter material including cheese cloth, cotton flannel, unbleached muslin, closely woven bleached muslin, filter paper and absorbent cotton were tested against tobacco smoke and silica dust. The efficiency of filters against tobacco smoke ranged from 5% for the cheese cloth filter to 97% for the dense woolen filter while, against silica dust, the efficiency values varied from 9% for the sponge filter to 96% for absorbent cotten filters. In general, the filters with higher efficiency also presented higher resistance to the airflow. It was also found that the silica dust particles, mostly 1 μm in diameter, had a tendency to quickly clog filters as compared to the tobacco smoke particles with a mean diameter of 0.27 μm which showed no tendency to clog any of the filters. Some materials were found to be more resistant to clogging than others. For example, filters of loose texture like cheese cloth or absorbent cotton clogged the least while, the dense filters

of paper or closely woven muslin clogged very rapidly.

Katz et al. (1926b) tabulated the test conditions and characteristics of each respirtor and its filter in another report and summarized the main results of the tests described above and the conclusions drawn from them.

A quantitative method for evaluating the over-all performance of respirators was developed by Burgess et al. (1961), which involved sealing a respirator on the face of a manikin in a test chamber containing a known concentration of uranine particles. A mechanical breathing pump was used to simulate the human breathing pattern through the respirator. The amount of uranine inside the face piece was determined by a flurometric analysis which was able to show penetration values as low as 0.05%.

Revoir and Yurgilas (1968) tested six Bureau of Mines approved respirators with replaceable filter elements and six non-approved respirators, all available commercially. The respirators were tested against aerosols of seven metallic and non-metallic particulates including silica dust, silicate polishing compound, cement, sulfur, lead, iron and zinc which were generated by an apparatus similar to that employed by the Bureau of Mines for generation of silica dust (Schrenk (1939)). The respirators were sealed against special holders in a test chamber and the filter efficiency and the pressure drop were measured. The

experimental parameters such as flowrate, particle concentration etc. were kept similar to the specifications of the Bureau of Mines for approval test. The results showed that the approved respirators were much more efficient in removing the particulates, while offering acceptable resistance to the air flow, than the non-approved respirators whose performances was found to vary widely.

Ferber et al. (1970) measured the penetraton of a number of dust, mist, fume and high efficiency respirator filters using sodium chloride aerosol with a count median diameter of 0.23 μm and σ_g of 2.3. The penetration measurments were made by a flame photometer at three flow rates of 16, 32, and 42.5 liters per minute. Their tabulated penetration results show that the high efficiency filters were more than 99.98% efficient and the fume filters made of organic and asbestos fibers were more efficient than those made of fiber glass and treated paper. Meanwhile, the dust and mist filters made of organic and asbestos fibers and resin-impregnated wool fibers generally showed higher penetrations than the fume filters. When compared with the DOP results obtained for the same filters, the resin-impregnated wool filters were found to be significantly more efficient against NaCl aerosol than against DOP particles.

The performance of same type of respirator filters as

above was also evaluated by Mitchell et al. (1971) using a polydisperse NaCl aerosol and a monodisperse 0.3 μm DOP aerosol. The NaCl aerosol had a count median diameter of 0.05 μm and a σ_g of 2.22. The penetration measurements were made for the flow rates of 16 and 42.5 liters per minute. Again, the tested high efficiency filters were found to have similar filtration characteristics, while the fume filters made of fiber glass, treated paper, and organic and asbestos fibers gave significantly different penetration values for the same aerosol. The efficiency of the dust and mist filters containing resin-impregnated wool fibers was found to degrade rapidly against DOP aerosol.

Ferber et al. (1972) determined the penetration of a polydisperse NaCl aerosol having count median diameter of 0.15μm and σ_g of 1.9 through high efficiency, fume, and dust and mist respirator filters at flow rates of 16 and 42.5 liters per minute. A comparison of the results with those obtained by the Los Alamos Scientific Laboratory (LASL) for the same type of filters showed significant differences for the dust and mist respirator filters. The differences were attributed to the smaller mean diameter as well as lower concentration of the NaCl particles used by the LASL.

Hyatt et al. (1972) evaluated the over-all performance of five half-mask and six full-face particulate respirators for their filter efficiency, leakage and fitting comfort

using a monodisperse DOP aerosol as the test aerosol. The respirators were worn by human test subjects, with various facial size and shape, who performed a number of different excerises in a DOP test chamber. The air inside the face piece was continuously sampled and the amount of penetration of DOP particles during each excercise was determined. Their study also considered the effects of the tightness of the headband straps and the facial hair on the degree of protection provided by the respirators. It was concluded that DOP aerosol respirator test would provide an accurate and meaningful evaluation of the performance of respirators.

Lowry et al. (1977) completed a detailed evaluation of over-all characteristics of single-use or disposable respirators considering their ability to fit a wide range of facial sizes, degradation of their filter efficiency after storage in a humid atmosphere and consistency of their protection when worn in a six-hour work shift. The penetration of a polydisperse sodium chloride aerosol through six different disposable respirators was determined as they were worn by ten people representing a variety of facial dimensions. The results indicated that only two of the six models tested provided a protection factor of 5 (protection factor is defined as the ratio of the contaminant concentration in the ambient air to that inside the face piece) to all ten members of the test panel. It was

also found that storage of respirtors in humid environment for about three weeks and constant exposure of respirator filters to the humid exhalation air in a six-hour work shift had no detectable effect on the efficiency of the filters.

Another study involving the single-use respirators was carried out by Harris and DeSieghardt (1977) in which three models of disposable respirators were worn by 97 coal miners who were asked to report the acceptability, as well as, disadvantages and advantages of this type of respirators. The collected data was basically qualitative showing that the miners were more concerned with the comfort of respirators than the level of protection provided by the respirators.

Lowry and Revoir (1978) compared a NaCl aerosol filter test method developed at the Los Almos Scientific Laboratory (LASL) to the silica dust and mist filter test methods used by NIOSH for respirator approval testing. The LASL NaCl aerosol test set-up was used to measure the penetration of NaCl particles through two types of resin-impregnated felt filter materials. Samples of both filters were also sent to four respirator manufacturing companies which performed the silica dust and mist tests. Meanwhile, one set of filters was sent to NIOSH where the materials were to be evaluated again for NaCl aerosol penetration. NIOSH performed the tests using NaCl aerosol test system identical to that of

the LASL. The purpose of NIOSH tests was to determine the reproducibility of the the NaCl aerosol penentration results. It was found that the penentration values obtained at the LASL were significantly different from those obtained at NIOSH. The cause of the difference was attributed to the loss of the electrostatic charge on the filter material during the time interval between the LASL and NIOSH NaCl aerosol tests. Also, the silica dust and mist tests did not consistently differentiate between the penetration level of the two types of filters as opposed to the LASL sodium chloride test method which did. The silica dust and mist penetration values for each filter as obtained by the four respirator manufacturers were different indicating, once again, the absence of agreement between penetration measurements of respirator filters obtained by the current test methods.

Smith et al. (1979) determined the efficiency of eight different respirator filters or filter/sorbent combinations against benzene soluble fraction and Benzo(a)pyrene (Bap) as found in the coke oven environment. The results showed that the filters which are approved against all three types of particulate hazards namely, dust, mist, and fume are significantly more efficient than those approved only against dust and mist particulates. Meanwhile, the penetration tests using NaCl aerosol revealed that the

filters which have already been exposed to the coke oven atmosphere, had higher NaCl aerosol penetrations than the fresh filters.

Willeke et al. (1981) recommended the use of a continuous flow Condensation Nuclei Counter (CNC) for fit testing instead of conventional techniques in which the particle concentrations inside and outside the face mask are determined by photometers or gravimetrical methods. A comparison of CNC versus photometer measured fit test with DOP aerosols has also been presented.

Cooper et al. (1983) measured the efficiency of fabric materials such as cotton fabric, thick and thin toweling, shirt material, bed sheet, and a single use respirator (3M Model # 8710) which are readily available in the emergency situations, as a function of particle diameter over the range of 0.4 to 5 μm using an optical particle counter. The test particles were generated by atomizing mineral oil using a nebulizer. The measurements were made for face velocities of 1.5, 5.0 and 15.0 cm/sec under dry and wet conditions of some of the materials. The results were presented in terms of the quality factor defined as the ratio of negative of the natural logarithm of penetration to the pressure drop across the filter at a given face velocity. The disposable respirator performed the best, showing higher effective factors than any of the fabrics. Among the fabrics, however,

the thick toweling material performed better than the rest. It was also found that the wet toweling generally had lower penetration values than the dry toweling while, the bed sheet and cotton fabric performed better in dry conditions than in wet conditions.

Fergin (1984) carried out tests to evaluate the performance of several disposable respirators against airborne particulates found in potroom environment of a pre-bake aluminum reduction plant. The disposable respirators tested were models 9910, 8706, and 9906 manufactured by the 3M Company. The respirators were worn by 38 non-bearded and 22 bearded workers while performing their duties. All three respirators showed acceptable performance (<10% penetration on the average) for both bearded and non-bearded workers.

Tuomi (1985) evaluated the over-all penetration characteristics of two half-mask respirators equipped with gas or particle filters, and two surgical masks (3M Aseptex and Johnson & Johnson Surgine II) using corn oil aerosol with a particle size range of 0.3 to 10 μm. The flow through the respirators was cyclic with only inhalation taking place at a mean flow rate of 102 liters per minute. The penetration values were measured by an optical particle counter. The fitler efficiency of the 3M surgical mask was remarkably low (a few percent) for particle diameters below

1 μm while that of the Johnson & Johnson mask varied from 30% to 55% for particles ranging in diameter from 0.3 to 1 μm. Both respirators were more than 95% efficient against particle diameters above 5 μm. Meanwhile, one of the half-mask respirators was of high efficiency type and the other one had efficiency values comparable to those of the Johnson & Johnson surgical masks.

Chapter 2

REVIEW OF ELECTROSTATIC FILTRATION

The removal of sub-micron particles from the environment where they can damage human health or the manufacturing of high technology products of very fine tolerance has recently been receiving much attention. Among various means for removing harmful airborn particles, such as percipitators, cyclons, etc., perhaps the most effective is filtration by fibrous filters.

Filters which rely solely on the mechanical collection mechanisms- diffusion, interception, inertia, and gravity- will capture the very small particles if their fibers are fine and closely packed (Dorman (1974), Dorman and Pich (1966), Davies (1973)). Such filters, however, have the great disadvantage of imposing a high resistance to the air that passes through them. By contrast, filters containing fibers at some charging state, act mainly by long range electrostatic forces to attract and remove the particles from the air flow. These filters have the advantage that they can be made much less dense than the mechanical fibrous filters, thus offering less resistance to air flow without loss of efficiency in capturing submicron particles. The fibers of an electrostatic filter may carry unipolar charges

to attract charged particles of opposite polarity as well as uncharged particles by induction. They may also carry permanently induced positive and negative charges in the form of permanent electric dipoles to attract charged particles of both polarities as well as uncharged particles. The fibers carrying permanent dipoles are commonly referred to as the electret fibers.

Electrostatic effect may be employed to improve (under proper conditions) the filtration performance of a relatively low efficiency mechanical filter by placing the filter in an external electric field. As a result, the fibers of the filter media become polarized and an inhomogeneous electric field is produced within the filter to influence the motion of both charged and uncharged particles towards or away from fibers depending on the operating conditions as will be explained below.

In addition, it is found that a mechanical filter is more efficient in capturing charged particles than uncharged particles since a charged particle in approaching a fiber induces charges of opposite polarity in the fiber which, in turn, attract the particle towards the fiber. This type of electrostatic force between a charged particle and an uncharged fiber is called the image force as an image of particle charge with opposite polarity is formed in the fiber.

The literature review of the electrostatic filtration given below begins with studies dealing with the case of uncharged fibers and charged particles followed by those considering the effect of an external electric field on the collection efficiency of a single fiber. Also, a review of the filtration performance of charged fibers, in particular the electret fibers, is given at the end.

The effect of various electrostatic forces on the capture efficiency of charged and uncharged particles by an isolated cylinder was considered by Natanson (1957) assuming both potential and viscous flows around the cylinder. In the case of a small charged particle approaching an uncharged cylinder, the electric force was approximated by that between a point charge and an infinite plane as following

$$F_r = \frac{\epsilon_c - 1}{\epsilon_c + 1} \cdot \frac{q^2}{4(r - R)^2} \qquad (2.1)$$

where ϵ_c is the dielectric constant of the cylinder, q is the particle charge, and R is the radius of the cylinder. The particle trajectory equations were solved and an approximate analytical solution was obtained using Lamb's expressions (1932) for the viscous flow around the cylinder. The cylinder capture efficiency of particles, η, was then

expressed by

$$\eta = \frac{2.0}{(2.002 - \ln Re)^{\frac{1}{2}}} \cdot (N_{oq})^{\frac{1}{2}} \qquad (2.2)$$

where $Re = \frac{u_o (2R)}{\nu}$ is the Reynolds number, u_o is the free stream velocity, ν is the kinematic viscosity, and N_{oq} is the dimensionless image force parameter defined as the ratio of the electrostatic image force to the drag on a particle,

$$N_{oq} = \frac{\epsilon_c - 1}{\epsilon_c + 1} \cdot \frac{q^2 c}{12\pi^2 \epsilon_o d_c^2 \mu d_p u_o} \qquad (2.3)$$

Where

ϵ_o = permittivity of free space

d_c = cylinder diameter

μ = gas viscosity

d_p = particle diameter

c = slip correction

Lundgren and Whitby (1965) measured the penetration of charged aerosol particles through three different uncharged filters to determine the influence of image force on

filtration efficiency. The single fiber efficiency values were calculated from the penetration data and the results were found to be well correlated by the following equation

$$\eta_s = 1.5 \, (N_{0q})^{\frac{1}{3}} \qquad (2.4)$$

Where η_s is the single fiber efficiency.

The case of charged particles approaching an uncharged, isolated cylinder was also considered by Yoshioka et al. (1968) who obtained numerical solutions to the particle trajectory equations using Lamb's expression for flow field around the cylinder and equation (2.1) for the image force acting on particles. The collection efficiency values were determined from plots of particle trajectories for each value of the Reynolds numbers equal to 0.2, 0.5, and 1. It should be mentioned that the Lamb's equations should not be used up to such high values of Re. They also carried out experiments on the filtration efficiency of monodisperse 0.5 μm particles carrying 0 to 70 electronic units. The filters were mats of glass fiber with fiber radii 5.9, 9, and 23 μm and porosities of 0.96 and 0.98. The filters were 1 cm and 3 cm thick and the face velocity was varied between 8 and 50 cm/sec. Their

experimental results correlated well with the equation

$$\eta_s = 2.3\ (N_{0q})^{\frac{1}{3}} \tag{2.5}$$

To take into account the influence of neighboroing fibers on the flow field around a fiber, Stenhouse (1974) considered a model filter consisting of a staggered array of parallel cylinders (fibers) arranged normal to the flow. Using the Kuwabara's equations (1959) for viscous flow around each fiber and neglecting the particle inertia, Stenhouse numerically solved the particle trajectory equations considering several electrostatic interactions. The values of the single fiber efficiency were then obtained from the critical trajectory calculations and the results for the case of image forces (uncharged fiber and charged particle) were found to be expressed well by

$$\eta_s = 1.5\ (N_{0q})^{\frac{1}{3}} \tag{2.6}$$

It is interesting to note that equations (2.2), (2.4), (2.5), and (2.6) all show the same functional relationship between the collection efficiency of an isolated fiber or a single fiber (η or η_s, respectively) and the dimensionless image force parameter N_{0q}, thus suggesting that the above relationship in the case of the image force interactions is

unaffected by the interference effects of neighboring fibers on the flow and electric fields around a typical fiber in a filter media.

Aside from the influence of image forces, the efficiency of a mechanical filter can be greatly enhanced also by applying an electric field across the filter during the filtering operation. As a result, the fibers of the filter become polarized and act as linear dipoles. The total electric field intensity around a typical fiber would then be the intensity of the external field plus the sum of intensities of the polarized fiber and its neighboring fibers. The resulting electric field is inhomogeneous causing both charged and uncharged particles to be attracted toward the fiber.

Let's consider an isolated dielectric cylinder with radius R and dielectric constant ϵ_c placed normal to the direction of an applied uniform electric field with an intensity E_o. The components of the total electric field around the cylinder due to E_o plus the induced field are expressed by

$$E_r = \left(\frac{\epsilon_c - 1}{\epsilon_c + 1} \cdot \frac{R^2}{r^2} + 1\right) E_o \cos\theta \qquad (2.7)$$

$$E_\theta = \left(\frac{\epsilon_c - 1}{\epsilon_c + 1} \cdot \frac{R^2}{r^2} - 1\right) E_o \sin\theta \qquad (2.8)$$

where r and θ are polar coordinates with their origin being at the center of the cylinder. A charged particle in this electric field will be drawn toward or repelled away from the cylinder depending on the polarity of particle charge and direction of the applied field. The components of the electric force acting on the particle can be written as

$$F_r = qE_r \tag{2.9}$$

$$F_\theta = qE_\theta \tag{2.10}$$

On the other hand, an uncharged particle in the above electric field becomes polarized and is pushed toward region of higher intensity i.e. toward the cylinder. The electric force acting on the particle is always attractive since the polarity of the charge induced in the particle is opposite to that of the cylinder. The force components, H_r and H_θ, on a particle of radius a_p and dielectric constant ϵ_p are expressed as

$$H_r = -\frac{\epsilon_p - 1}{\epsilon_p + 2} \cdot 2a_p^3 \left(\frac{\epsilon_c - 1}{\epsilon_c + 1} \cdot \frac{R^2}{r^2} + \cos 2\theta\right) \cdot \frac{\epsilon_c - 1}{\epsilon_c + 1} \cdot \frac{R^2}{r^3} E_o^2 \tag{2.11}$$

$$H_\theta = -\frac{\epsilon_p - 1}{\epsilon_p + 2} \cdot 2a_p^3 \left(\frac{\epsilon_c - 1}{\epsilon_c + 1} \cdot \frac{R^2}{r^3} \cdot \sin 2\theta\right) E_o^2 \tag{2.12}$$

Provided that a_p << R. In deriving the above equations the influence of the polarized field of the particle itself on the existing electric field was neglected.

Zebel (1965) worked out a theory for particle deposition on an isolated, uncharged cylinder in an electrical field considering both charged and uncharged particles. For the case of charged particles, he found that the cylinder capture efficiency was independent of the type of fluid flow, viscous or potential, and could be expressed by

$$\eta = G \frac{A + 1}{G + 1} \qquad (2.14)$$

provided that $G>0$ .In this equation,

$$A = \frac{\epsilon_c - 1}{\epsilon_c + 1} \qquad (2.15)$$

and

$$G = \frac{E_o q B}{u_o} \qquad (2.16)$$

where B is the mechanical mobility of particles given by

$$B = \frac{c}{3\pi\mu d_p} \qquad (2.17)$$

assuming Stokes law for the particle drag. For $\beta<0$, it was found that no particle deposition would take place and a dust-free region is formed around the fiber.

For the case of uncharged particles polarized by the combined electric field of the cylinder and the external source, Zebel was able to obtain an exact solution to the particle trajectory equations for the limiting case of $A \to 0$ ($\epsilon_c \to 1$) for both viscous and potential flows. The cylinder collection efficiency was then determined as

$$\eta = \frac{\beta}{2} \qquad \text{for } \beta \leq \sqrt{2} \qquad \text{potential flow} \qquad (2.18)$$

and

$$\eta \approx \frac{\beta}{2} \qquad \text{for } \beta \ll 1 \qquad \text{viscous flow} \qquad (2.19)$$

where

$$\beta = \frac{\epsilon_p - 1}{\epsilon_p + 2} \cdot \frac{\epsilon_c - 1}{\epsilon_c + 1} \cdot \frac{2a_p^3}{R} \cdot \frac{E_o^2 B}{u_o} \qquad (2.20)$$

is the ratio of particle velocity due to the influence of drag and electrical forces to the free stream velocity and

$$\overline{\beta} = \beta \left(2.002 - \ln Re \right) \qquad (2.21)$$

The terms inside the paranthesis come from the use of the Lamb's equations for the viscous flow around an isolated cylinder.

Subsequently, Zebel (1969) took a boundary layer approach to formulate the combined effects of the electrostatic forces and Brownian diffusion of particles in the form of the steady state boundary layer equation for particles with no inertia,

$$u \frac{\partial N}{\partial x} + v \frac{\partial N}{\partial y} = \frac{1}{Pe} \cdot \frac{\partial^2 N}{\partial y^2} \qquad (2.22)$$

where x and y are the spatial coordinates along and normal to the surface of the cylinder, respectively, u and v are the velocity components of particles parallel and perpendicular to the surface, respectively, N is the particle concentration within the boundary layer, and Pe is the Peclet number defined as $Pe = \frac{u_o R}{D}$ where D is the diffusion coefficient of particles. The above differential equation was approximated by the integral equation of Karman and Pohlhausen method which basically expresses the same conservation principles for a finite control volume bounded

by the cylinder and the edge of the boundary layer. The integral equation was evaluated assuming linear and fourth order profiles for the particle concentration in the boundary layer and the results were used to determine the deposition rate of particles. Expressions for the cylinder collection efficiency under various electrostatic interactions were obtained.

Hochrainer (1969) carried out experiments to verify the theoretical results of Zebel (1969). He found that particle trajectories agreed qualitatively with the Zebel's Theory, but the lack of satisfactory agreement between theory and experiment was attributed to inability to incorporate the theoretical conditions in the experiments.

Walkenhorst (1970) proposed and tested a new method for producing an inhomogeneous electric field inside a filter by considering a membrane filter between two oppositely charged wires. The filter and the wires were exposed to a flow of coal dust aerosol and a dust shadow picture was formed on the filter. A comparison of the shadow graph of charged and uncharged wires indicated the great influence of the electrical forces in attracting and capturing particles passing at distances far from the wires. The charge polarity on the wires was then reversed and the effect on the particle deposition was observed. These ideas were then applied in a filter consisting of few layers of wound

frames. The winding of each layer was a pair of mutually insulated wires. By applying 600V across each pair of windings, a much improved filtration efficiency was obtained in comparison to the efficiency of ordinary fibrous filters.

Kirsch (1972) conducted an extensive experimental study of filtration performance of real and model filters under the influence of an applied external electric field at small Reynolds numbers. The model filters were made as : 1) a staggered array of long parallel cylinders placed normal to the flow direction; 2) parallel rows of long cylinders with each row oriented at random similar to the "fan" model introduced by Kirsch and Fuchs (1968). Obviously, the important advantage of either of these models over Zebel's isolated cylinder model is the inclusion of the interference effects of neighboring fibers on the flow field and electric field around each individual fiber. The experimental values of the single fiber efficiency as defined by Kirsch were found to be well correlated by the following equation for both model filters assuming $\epsilon_c = \epsilon_p = \infty$,

$$\eta_s = m\beta^n \qquad (2.23)$$

where m and n are constants equal to approximately 1 and $\frac{2}{3}$, respectively, for the staggered model and approximately 0.8 and $\frac{2}{3}$, respectively, for the fan model

and β is given by equation (2.20).

Rao et al. (1973) studied theoretically the deposition of charged dust particles on a single fiber as part of a model consisting of three parallel fibers arranged vertically normal to the air flow in a homogeneous electric field. Assuming potential flow, the velocity and electrostatic potentials were corrected for the interference effects of the neighboring fibers. Also, the particles were assumed small enough so that the effect of polarization of particles themselves as well as image, gravity and inertia forces acting on particles could be neglected. For the case of negligible interference effects (isolated fiber) an analytical solution was obtained to the particle trajectory equations, which resulted in the following expression for the fiber capture efficiency of charged particles,

$$\eta = 1 + N \tag{2.24}$$

where

$$N = \frac{AG - 1}{1 + G} \tag{2.25}$$

Note that equation (2.24) is identical to equation (2.14) obtained by Zebel. For $N < -1$, no particle deposition takes place and the fiber is surrounded by a cylinder shaped "dust-free" space in agreement with the Zebel's findings.

For the case of non-negligible interference effects as

determined by the value of the Fuchs number not being much less than one (The Fuch number, Fu, is defined as Fu = $\frac{2a_f}{l}$ where l is the distance between centers of two succesive fibers and a_f is the fiber radius), the particle trajectory equations had to be solved numerically by the Runge-Kutta method to obtain the critical trajectory for the calculation of the single fiber efficiency. It was found that for $N_R > 0$ the inclusion of the interference effects in the calculations gave lower single fiber efficiency values than those obtained from the Zebel's isolated fiber theory. For $N_R < 0$ the three-fiber model and the Zebel's model gave nearly same efficiency values.

Ariman and Tang (1975) using the same three-fiber model as described above determined the collection efficiency of uncharged particles by charged fibers placed normal to the air flow in a homogeneous electric field. The particle trajectory equations were solved numerically and the critical trajectories and hence, the single fiber effeciency values were determined for different values of A, Fu, and β. The dependence of the fiber efficiency on each of the above parameters was presented graphically.

Henry and Ariman (1981) used the Kuwabara (1959) cell model instead of the three-fiber model to take into account the interference effects of neighboring fibers more effectively than the three-fiber model. Moreover, the use of

potential flow in the three-fiber model seriously limits the application of the results to the filtration problems which almost always deal with the Reynolds numbers much below one.

For the case of charged particles, the particle trajectory equations were solved and a formula expressing the single fiber efficiency was obtained as following

$$\eta_s = \frac{G(A + 1)}{G(A\alpha + 1) + 1} \qquad (2.26)$$

where A and G are expressed by equations (2.15) and (2.16), respectively, and α is the solid volume fraction defined as the fraction of the cell volume occupied by the fiber. A comparison with the Zebel's equation (equation (2.14)) indicated the efficiency values given by the isolated fiber theory of Zebel are always greater than those given by the cell theory.

For the case of uncharged particles, the particle trajectory equation was solved numerically and the critical trajectory was determined. The single fiber efficiency values were calculated for various values of α and Kn, where Kn is the Knudsen number defined as $Kn = \frac{\lambda}{a_f}$ and λ is the mean free path of gas molecules. The inclusion of Kn allowed the effect of slip flow on the fiber collection efficiency to be investigated. A comparison of results for Kn = 0 (no slip) with the Zebel's theory indicated again that the

isolated fiber theory would give higher values for the collection efficiency of uncharged particles in comparison to the cell theory. It was also found that the occurrence of slip flow on the surface of the fiber increases its collection efficiency.

Henry and Ariman (1981) also studied the influence of neighboring fibers on the electric field around a typical fiber in a cell model filter under the influence of an external uniform electric field. It was found that taking into account the electrical interference effects reduces the single fiber efficiency compared to the case of no interference effects. Also, the influence of neighboring fibers was shown to be more significant when the Coulombic forces were dominant. In general, however, it was suggested that the neighboring fibers have a larger effect on the flow field than the electric field around a typical fiber. But it was mentioned also that this concept may not be applicable to the case of highly charged fibers.

Thus far, the effects of image forces and the influence of an external uniform electric field upon the collection efficiency of an isolated fiber or a single fiber have been considered. In both cases, some charge is induced in an otherwise uncharged fiber resulting in enhancement of the fiber collection efficiency.

Another group of electrostatic filters which have been

widely used in many different applications are those containing charged fibers in the absence of any external field. These fibers like those in a homogeneous electric field generate a strong inhomogeneous electric field in their vicinity and act upon the oncoming particles by strong electrical forces. The filters containing charged fibers can therefore be made less dense than conventional filters, offering less resistance to the airflow. The combination of high efficiency and low air resistance has made such filters very attractive for use in the particulate-removing respirators.

It is important to note that the high filtration efficiency offered by the charged filters is obtained in the absence of any external electric source which means cost and energy savings in the filtering operations.

The charges on the fibers could result from either direct charging such as impregnation of a wool filter by negatively charged resin particles or a charging technique which places a permanent line dipole on a thin sheet of filter material which will be processed later into fibers. This type of bipolar fibers is commonly referred to as electret fibers and will be described in detail later. Both unipolar and bipolar charged fibers generate a very strong inhomogeneous electric field around themselves, which cause the attraction of charged particles by Coulombic forces and

uncharged particles by polarization or induction forces.

Gillespie (1955) determined the charge level on fibers of a wool-resin filter and gave a value of 0.003 nC/cm of fiber. Since the fiber diameters were about 22 μm, this amounts to a charge denisty of 0.4 nC/cm^2 in comparison to the electret fibers which have a charge density of 90 nC/cm^2 (Van Turnhout et al. (1979)), a factor of almost 200 times the charge density of a wool resin-fiber. Thus, the electric field intensity around an electret fiber is much stronger than that around a wool resin-fiber resulting in higher collection efficiency for the electret fibers. Moreover, the charges on electret fibers are bipolar making them capable of capturing particles of both polarities.

The electrets are usually made by heating a dielectric material under the influence of a strong electric field to facilitate the separation of negative and positive ions. While separated, a rapid cooling of the material reduces the mobility of ions so much that they will be virtually frozen in their position, thus giving rise to permanent dipoles in the material. The electrets can be made also by injecting positive and negative ions, produced by corona discharge, onto a thin film of the electret material. A review of the types of electret materials and their charge-storing capabilities and applications in a variety of products has been given by Van Turnhout (1975). In addition

to his review, Van Turnhout determined the penetration of the liquid DBP (dibutyl phthalate) and solid NaCl aerosols through two types of the electret filter materials, namely, PET (polyethylene terephthalate) and PP (polypropylene). The results of both filters indicated a very low penetration initially followed by an increase in penetration as more material was being loaded on the filters. This was probably caused by the shielding effect of the deposited particles on the electric field around fibers. The increase in penetration was more dramatic for the DBP aerosol as the liquid particles may have formed a conductive film around the fiber. The loss of the electrostatic efficiency, however, was compensated at some point by an increase in the mechanical efficiency as the filter was being loaded. A comparison of the performance of the electret filters with high efficiency, uncharged filters showed about the same initial penetration values while the pressure drop for the electret filters was about ten times lower than that for the high efficiency filters at the same flow rate. One year later, Van Turnhout et al. (1976) described a method for producing electret filters on an industrial scale. The electret fibers produced by this method attained rectangular cross-section with average dimensions of 9μm thick and 39μm wide. It was also shown that relatively high environmental temperature and relative humidity did not have any

significant effect on the performance of the electret filters. Van Turnhout et al. (1979) also reviewed properties of the electret filters and their various applications in detail.

Kraemer and Johnstone (1955) in a basic study of electrostatic forces considered the collection efficiency of charged and uncharged particles by a spherical and a cylinderical charged collector in the absence of any external electric field. For the cylindrical collector, the displacement of the flow streamlines by the cylinder was ignored and a uniform flow was used for calculation of particle trajectories. Approximate equations for the collection efficiency of the charged cylinder were obtained as following

$$\eta = \pi N_{Qq} \qquad \text{charged particles} \qquad (2.27)$$

$$\eta = \left(\frac{3\pi}{2} N_{Q0}\right)^{1.33} \qquad \text{uncharged particle} \qquad (2.28)$$

where

$$N_{Qq} = \frac{Q\, q\, c}{3\pi^2 \mu \epsilon_o d_p d_f u_o} \qquad (2.29)$$

and

$$N_{Q0} = \frac{\epsilon_p - 1}{\epsilon_p + 2} \cdot \frac{Q^2 d_p^2 c}{3\pi^2 \mu \epsilon_o d_f^3 u_o} \qquad (2.30)$$

where Q is the amount of charge per unit lenght of the cylinder.

Gellespie (1955) measured the penetration characteristics of resin-wool filters using charged and uncharged aerosol and compared the results with his filtration theory which considered both mechanical and electrostatic capture mechanisms. Both theory and experiment indicated that the most penetrating particle diameter for the case of uncharged aerosol was smaller than that for the case of the charged aerosol with the difference depending on the charge density of fibers as well as the charge distribution of the test aerosol. This result can be explained by the fact that the Coulombic forces become stronger with decreasing particle size in contrast to the induction forces which become stronger with increasing particle size. Therefore, in the case of uncharged particles polarized by fibers, the peak of the penetration-vs.-particle diameter curve tends to fall around relatively small particles against which the induction forces are weak, whereas, in the case of charged particles, the curve tends to shift towards relatively larger particles against which the Coulombic forces are weak.

Natanson (1957) considering an isolated charged cylinder transverse to viscous flow obtained approximate solutions to the trajectory equations of charged and

uncharged particles and determined the capture efficiency of the cylinder for each case. The results were expressed as

$$\eta = \pi N_{Qq} \qquad \text{charged particles} \qquad (2.31)$$

$$\eta = \pi N_{Q0} \qquad \text{uncharged particles} \qquad (2.32)$$

Notice that equation (2.31) is the same as equation (2.27) obtained by Kraemer and Johnstone (1955) who used a uniform flow field as opposed to the Lamb's flow field used by Natanson. This similarity suggests that the efficiency of capturing small charged particles by a uniformly charged fiber is independent of the type of the flow field assumed around the fiber.

Using the Kuwabara cell model, Stenhouse (1974) numerically solved the trajectory equations of charged and uncharged particles as being attracted toward a charged fiber. The particle size was also taken into account in the calculations by increasing the cylinder capture radius by the radius of the particle. The calculations were made for the solid-volume fraction or packing density $\alpha = 0.03$ and an interception parameter $N_R = 0.05$ where N_R is defined as the ratio of the particle diameter to the fiber diameter. The calculated single fiber efficiency values were found to be

well expressed by the following relationships,

$$\eta_s = 2.8\ N_{Qq} \qquad \text{charged particles} \qquad (2.33)$$

$$\eta_s = 0.84\ N_{Q0}^{1.75} \qquad \text{uncharged particles} \qquad (2.34)$$

Again, equation (2.33) except for its coefficient is similar to equations (2.27) and (2.31). The results of calculations for several values of α indicated that in the case of charged filters, increasing the filter packing density had little or no effect on the single fiber efficiency.

Due to the complex nature of the electric field and unavailability of an analytical solution for the flow field around a rectangular electret fiber carrying permanent dipoles, Brown (1981) considered a circular line dipole fiber instead, and determined its single fiber efficiency in capturing both charged and uncharged particles by solving the trajection equation of particles. The flow field around the fiber was expressed in a general form as a function of a parameter called the hydrodynamic factor, K, whose exact form depends on the theoretical flow field assumed around the fiber. Simple, but general power-law equations were obtained approximating the single fiber efficiency as a

function of appropriate dimensionless parameters as follows,

$$\eta = 0.55\ K^{-1.27}\ N_{pq}^{1.83} \qquad \text{charged particles} \qquad (2.35)$$

$$\eta = 0.41\ K^{-1.61}\ N_{p_0}^{1.41} \qquad \text{uncharged particles} \qquad (2.36)$$

where N_{pq} and N_{p_0} are dimensionless force parameters expressing the ratio of the appropriate electric force to the drag on a particle,

$$N_{pq} = \frac{-\sigma q c}{3\pi\mu(1+\epsilon_f)u_o\epsilon_o d_p} \qquad (2.37)$$

$$N_{p_0} = \left(\frac{\epsilon_p - 1}{\epsilon_p + 2}\right) \frac{2\sigma^2 d_p^2 c}{3\epsilon_o(1+\epsilon_f)^2 d_f \mu u_o} \qquad (2.38)$$

where σ is the charge density on the fiber surface. It must be mentioned that the coefficients of equations (2.35) and (2.36) (0.55 and 0.41, respectively) are different from those given by Brown in his paper (0.59 and 0.54, respectively) because the Brown's coefficients do not yield the specific equations obtained by him for the case of K = 0.797 (equations (16) and (24) in the Brown's paper) while, the present coefficients do.

Brown (1982) developed a theory for the collection efficiency of charged and uncharged particles by uniformly

charged and line-dipole fibers arranged parallel to the direction of flow. The resistance to the air flow in such configuration of fibers was shown to be exactly half the resistance of a system of fibers arranged normal to the air flow. Meanwhile, if the particles were charged and the fibers were uniformly charged, the capture efficiency of a parallel fiber system was shown to be consistently higher than that of a perpendicular fiber system of similar structure.

In the capture of charged or neutral particles by line-dipole fibers or of neutral particles by uniformly charged fibers, the parallel fiber system was shown to be more efficient over short distances.

It was also mentioned that the mechanical efficiency of parallel fibers is low and cannot compensate for the loss of electrostatic efficiency caused by deposition of particles, especially those of organic materials.

Jodeit and Loffler (1984) conducted experiments to investigate the penetration characteristics of fibrous filters when loaded with charged and uncharged aerosols. It was shown that the efficiency of an uncharged filter made of monodisperse polyacetate fibers increased with time as the filter was being loaded with uncharged quartz particles. A similar but a more rapid increase in the filter efficiency was observed when the loading was performed with charged

quartz particles. In addition, the filtration efficiency of two different electret filters was also evaluated. One of the filters made of very fine charged fibers (micro-fiber fleece) was loaded with uncharged quartz particles and the results indicated a continuous increase in efficiency with loading time for the particle size range considered. However, the other filter made of relatively coarse polypropylene fibers with dipole characteristics and rectangular cross-section (Maximum area of 10 X 200 μm^2) showed an increase in penetration with the loading time for a considerable period. Only after a considerable amount of dust had been deposited on the filter, the penetration began to decrease as the mechanical filtration became dominant.

Schurmann and Fissan (1984) determined the penetration characteristics of a charged filter as a function of particle diameter using uncharged and neutralized DOP aerosols containing particles ranging from 0.03 to 1 μm in diameter. The experimental results indicated a rather rapid loss of filter efficiency down to about 60% where it finally leveled off as the filter was loaded with the neutralized aerosol particles. The increase in penetration with loading time was assumed to be due to discharging of fibers by the charged particles in the neutralized DOP aerosol. Based on this assumption, they estimated the number of charges per unit length of fiber by calculating the number of charges

transported to the filter by the aerosol until the collection efficiency leveled off.

Similarly, the efficiency of the same type of filter was measured as the filter was loaded with the uncharged DOP aerosol. The results indicated a nearly constant filter efficiency at about 96% over duration of the test which lasted about an hour. This, of course, suggests that the deposition of uncharged DOP particles had no significant effect on the filter efficiency in contrast to the findings that the liquid particles such as DOP depositing on a charged fiber can coalesce and shield off the electric field around the fiber, thus weakening the effect of the electrostatic forces. Nevertheless, one can attribute the results of the above experiment with the uncharged aerosol to a combination of increasing effects of the mechanical collection mechanisms and slowly weakening electrostatic forces, which results in a rather constant collection efficiency for the filter.

Lathrache et al. (1986), Lathrache and Fissan (1986), and Fissan and Lathrache (1986) obtained theoretical expressions for the collection efficiency of two types of charged fibers, namely, spun and split fibers used in the electret filters. The spun fibers are circular and carry unipolar charges while, the split fibers are more rectangular in their cross-section and carry bipolar

charges. The theoretical results were examined experimentally as the penetration values of monodisperse solid and liquid aerosols through filters containing the spun or split fibers were measured. The theoretical expressions for the single fiber capture efficiency of both charged and uncharged particles by dipole fibers were obtained from the critical trajectory calculations and are expressed as following for the case of charged particles,

$$\eta_s = \left(\frac{1 - \alpha}{K}\right)^{1/8} \frac{\pi N_{pq}}{1 + 2\pi N_{pq}^{1/4}} \qquad \text{for } N_{pq} > 10^{-4} \tag{2.39}$$

and for the case of uncharged particles,

$$\eta_s = \left(\frac{1 - \alpha}{K}\right)^{2/5} \frac{\pi N_{p_0}}{1 + 2\pi N_{p_0}^{2/3}} \qquad \text{for } N_{p_0} > 10^{-4} \tag{2.40}$$

where K is the hydrodynamic factor corresponding to the Kuwabara flow field and given by

$$K = -0.5 \ln \alpha - \frac{3}{4} - 0.25 \alpha^2 + \alpha \tag{2.41}$$

and N_{pq} and N_{p_0} are given, respectively, by equations (2.37) and (2.38).

The experimental and theoretical results were found to

be in good agreement with both indicating a considerable enhancement in the filter efficiency due to the electrostatic forces. In addition, it was shown both theoretically and experimentally that a charge-equilibrated polydisperse aerosol had a bimodal penetration characteristics through the electret filters.

All the theoretical studies of the collection efficiency of charged fibers, which have been reported so far, consider circular fibers even for the electret filters which are typically composed of rectangular fibers carrying permanent positive and negative charges. The filtration performance of electret fibers has not yet been studied theoretically because of the complexity of electric field and unavailability of an analytical solution for the flow field around such fibers. But recently, Japanese investigators have begun both theoretical and experimental work on the collection efficiency of the rectangular electret fibers. One such study has been conducted by Emi et al. (in press) to determine the efficiency of a single electret fiber in capturing both charged and uncharged particles by solving the equation of particle motion taking into account the effects of the Coulombic and induced forces simultaneously. The flow field around the fiber was approximated by the analytical expressions for the

viscous flow around an isolated elliptic body with zero thickness and the electric field intensity around the fiber was approximated by the sum of the electric field intensities of sufficiently large number of imaginary line charges of both polarities assumed on two opposite sides of the fiber while, neglecting the effect of the polarization field within the fiber. The calculated fiber efficiencies were compared with the experimental values obtained from the penetration measurements of monodisperse NaCl particles through an electret filter with the same physical properties as those assumed in the theoretical calculations. The particle diameters ranged from 0.01 to 0.4 μm and were conditioned to carry no charge, single or double charges or charges according to the Boltzmann charge equilibrium. The results showed that a small change in the charging state of particles would greatly influence the filter efficiency and that both Coulombic and induced forces affect the collection of charged particles simultaneously. Also, both theory and experiment predicted the same dependency on the dimensionless force parameters for both Coulombic and inductive interactions.

Based on the theoretical and experimental results, a semi-empirical expression for the collection efficiency of a single electret fiber was obtained with the coefficients being dependent on the magnitude of the fiber charge. The

equation expressed in a general form is

$$\eta_s = X\, N_{Q0}^{1.4} + Y\, N_{Qq}^{1.75} - Z\, (N_{Q0} \cdot N_{Qq})^{1.5} \qquad (2.42)$$

where constants X, Y, and Z are the fiber charge dependent coefficients which according to the experimental results were found to be 0.06, 0.067 and 0.017, respectively, and N_{Qq} and N_{Q0} are the respective Coulombic and Induced dimensionless force parameters given by equations (2.29) and (2.30), respectively, with the exception that the fiber diameter d_f in those expressions should be replaced with the width of the electret fiber for the case of the rectangular fibers.

Kanaoka et al. (1987) measured the penetration characteristic of an electret filter using monodisperse NaCl particles ranging in diameter from 0.02 to 0.4 μm and at different charging states. The experimental results of the single fiber collection efficiency of charged and uncharged particles were compared to those obtained theoretically from equation (2.42) and a fairly good agreement was obtained.

To determine the single fiber capture efficiency of the rectangular fibers due to the Brownian diffusion of particles, the theoretical values of the single fiber efficiency due to the induction forces were subtracted from the experimental values obtained for the case of uncharged

particles and small values of N_{Q0} and the results were found to be well correlated by the following equation,

$$\eta_s = W\, Pe^{-2/3} \tag{2.43}$$

where W is a numerical constant whose values depend upon the charge density of fibers and Pe is the Peclet number defined as $Pe = \frac{u_o\, w}{D}$ for the case of a rectangular fiber with w being the width of the fiber facing normal to the flow direction. Notice that the dependency of η_s upon Pe for the case of rectangular fibers is the same as that for the case of circular fibers. Adding the above equation to equation (2.42), the single fiber collection efficiency due to the combined effects of Brownian diffusion and electrostatic mechanisms was experessed, in general, as

$$\eta = X\, N_{Q0}^{1.4} + Y\, N_{Qq}^{1.75} - Z\, (N_{Q0}\, N_{Qq})^{1.5} + W\, Pe^{-2/3} \tag{2.44}$$

This expression was found to give good correlation to the experimental results. Meanwhile, the theoretically determined values of the most penetrating particle size were also found to agree well with the experimental data. The most penetrating particle diameter in the case of uncharged particles was slightly larger than 0.1 μm and was found to increase with the particle charge in the case of charged

particles.

Also, experiments with particles in charge equilibrium indicated that the penetration of such particles through the electret filters showed a bimodal dependency on the particle diameter at high filtration velocities. This characteristic was observed also by Fissan and co-workers as mentioned previously.

2.1 Present Work

The main objectives of the present work are to conduct: 1- an experimental study of filtration characteristics of disposable respirator filters and 2- a theoretical study of filtration characteristics of charged rectangular fibers.

In the case of the experimental study, the penetration values of monodisperse liquid and solid particles ranging in diameter from 0.035 to 4 μm through filters of several commercially-available disposable respirators are to be measured. The measurements are to be made by three commonly used aerosol instruments for purposes of comparing their reponse when used in the filtration studies. In addition, the penetration characteristics of several monodisperse aerosols through one of the filters under various loading conditions will also be investigated.

In the case of the theoretical study, the viscous flow

field in a staggered array of rectangular fibers is to be determined numerically and used to obtain the values of the single fiber efficiency due to the Brownian diffusion, interception, and electrostatic capture mechanisms. The calculations are to be made for a wide range of values of the parameters involved.

Chapter 3

EXPERIMENTAL STUDY

The filtration performance of several commercially available respirator filters are to be evaluated using monodisperse liquid and solid aerosols at each of the flow rates 16, 28, and 48 liters per minute. The penetration values are to be measured by three commonly-used aerosol instruments for purposes of comparing their response when used in the filtration studies. A detailed description of the experimental apparatus composed of the test chamber, aerosol generators and measuring instruments used is given below. The apparatus performance and experimental procedures are described at the end of the chapter.

3.1 Test Chamber

A schematic diagram of the test chamber is shown in Figure 3.1. For ease of description, the chamber has been divided into three sections: The mixing section at the top, the filter holder setup in the middle and the exhaust section at the bottom.

The function of the mixing section is to provide a uniform distribution of the particle concentration across

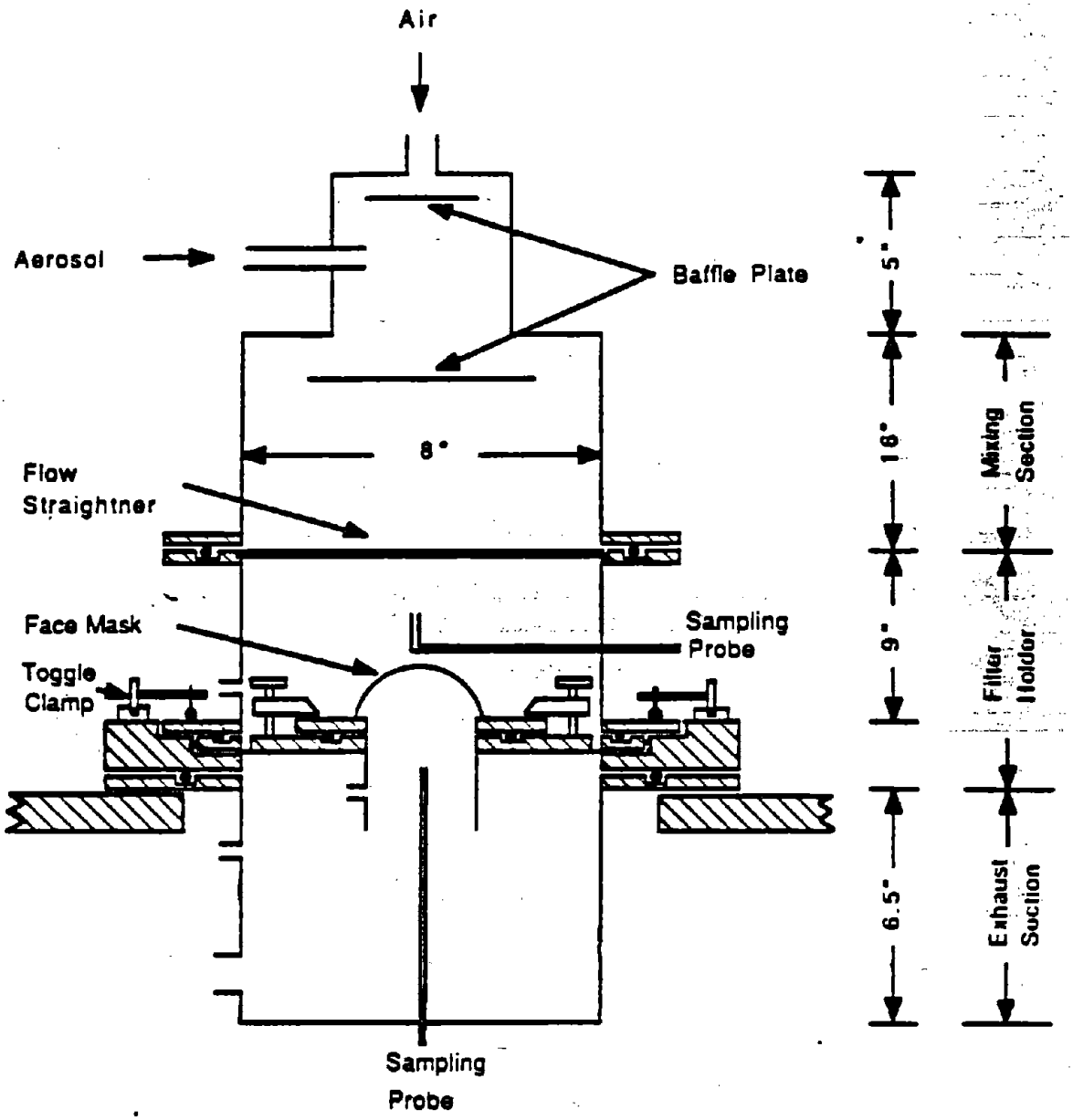

* Dimensions not to scale.

Figure 3.1 Schematic diagram of the test chamber for testing disposable respirators as well as flat filter media

the cross-section of the chamber upstream of the filter being tested. This is assumed to be accomplished by the large eddies generated behind the baffle plates placed perpendicular to the aerosol flow. The success or lack thereof this approach will be discussed later in the chapter. The clean air flow supplied at the top is used not only to dilute the aerosol for controlling the particle concentration upstream of the filter, but also to increase the flow rate to the desired value in case the aerosol flow rate itself is not sufficient.

The aerosol flow then enters the second part of the chamber, The filter holder, through a bank of honeycomb shaped pores which are used to dissipate the energy of the eddies and straighten the flow prior to its passage through the filter. The effectiveness of this approach will also be discussed. This part was designed to be replaceable so that the chamber could be used for testing of not only disposable face masks but also 4 and 8 inch flat filter media in the future. For example, the holders for 8" and 4" flat filters are shown respectively in Figures 3.2 and 3.3. As shown in Figure 3.2, an 8" filter placed on a perforated plate is compressed between the base of the holder and a tightly-fitting ring upon which the upper portion of the chamber rests during operation. As seen, various contact points are sealed by rubber "o" rings to prevent air

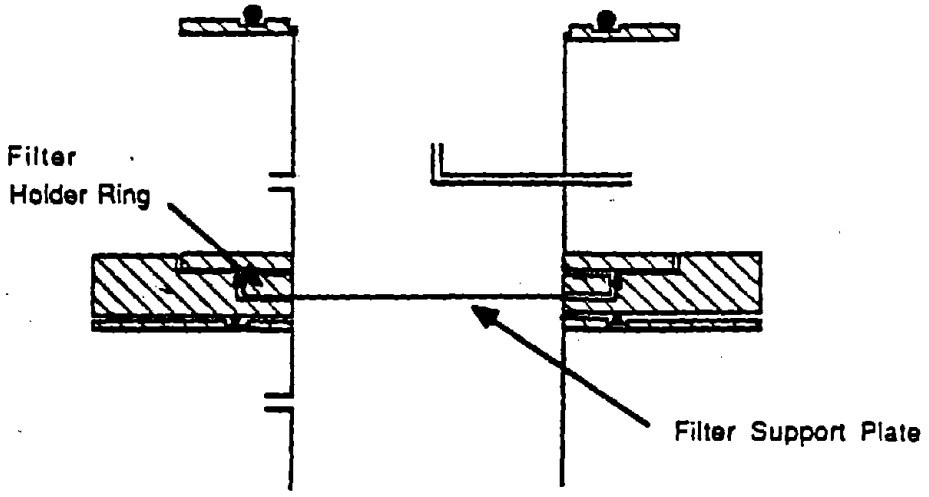

Figure 3.2 Filter holder for 8" flat filter media

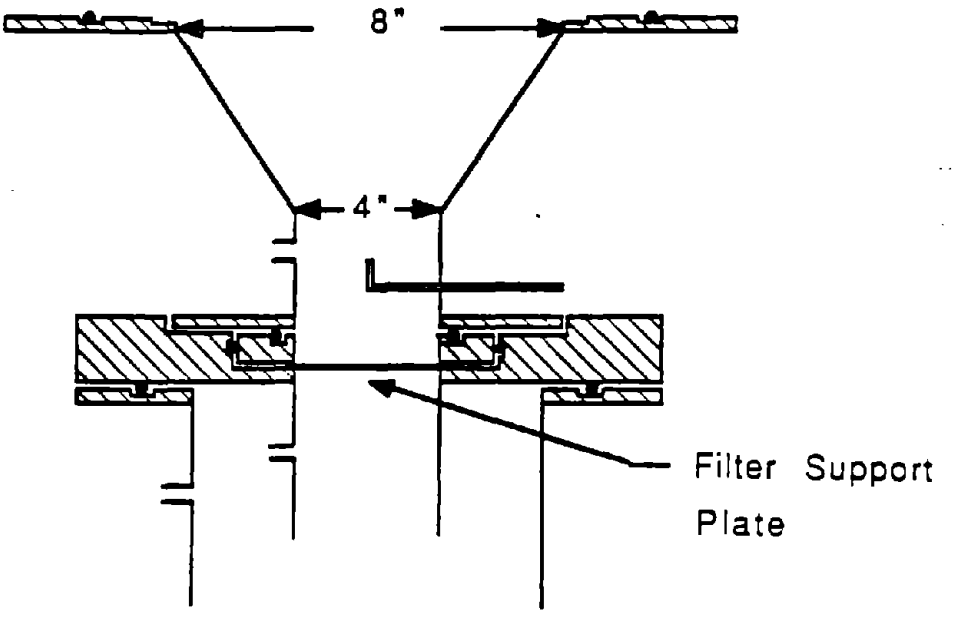

Figure 3.3 Filter holder for 4" flat filter media

leakage. Six toggle clamps provide additional reinforcement for better seal. Similar features are considered also for 4" filter holder as shown in Figure 3.3, in addition to the converging section of the holder which causes the aerosol flow to converge onto surface of the filter.

As for the design of a face-mask holder which is of main interest to the present study, it seemed to be impractical to design a universal holder for all the variable shape and size single-use respirators available on the market. Therefore, the approach taken here was to glue each selected face-mask onto the surface of a flat plate with a concentric hole and then design a holder for holding the plate in the test chamber. A expanded diagram of the face-mask holder of Figure 3.1 is shown in Figure 3.4. The face-mask plate made of aluminum contained a concentric hole of 3" in diameter which was smaller than the face coverage area of the available face-masks. The plate was fastened to a concentric disk having the same hole diameter as the plate by several adjustable clamps. The disk was designed and made compatible with the 8" filter holder in such a way that it could be held in place around its edge between the holder base and the filter ring just like an 8" flat filter would have as described above. Notice that the perforated plate used for supporting filters is removed for this application. Figure 3.5 illustrates pictorially the face-mask holder as

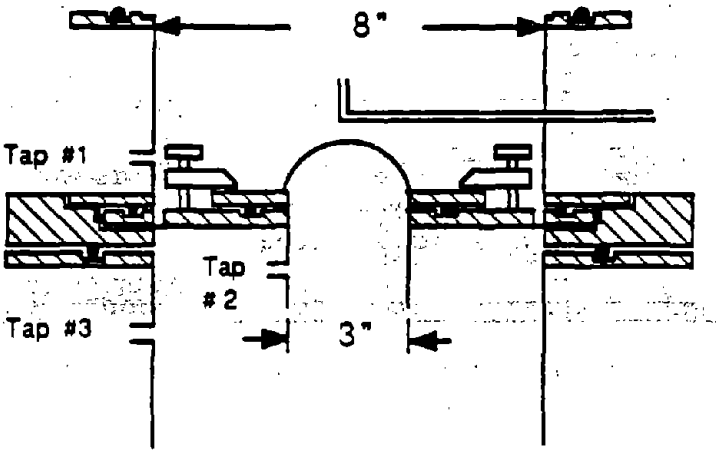

Figure 3.4 Face-mask holder contained in the 8" flat filter holder

Figure 3.5 Photograph of a disposable respirator as glued onto a supporting plate which is held in place by adjustable clamps

mounted in place. The white-appearing substance around the edge of the respirator is the "hot melt" type of glue used to glue the face-mask to the plate.

In addition, this section of the chamber contains also a sampling probe and two pressure taps (#1 and #2) as shown in Figure 3.4 to measure the particle size distribution upstream of and the pressure drop across a respirator filter, respectively. The upstream probe was held normal to the aerosol flow and could be moved in and out of the chamber to collect aerosol samples at various locations for determining the degree of spatial uniformity of the particle number concentration.

Finally, the bottom section of the chamber contains a probe for sampling the aerosol downstream of the face-mask, a pressure tap (#3), and an exit port. The port was connected to a HEPA filter using a big tube connector which was mounted on the port. A small nozzle was built and placed inside the connector to measure the total flow rate through the apparatus. Figure 3.6 shows position of the nozzle. As the tube connector is tightened, the nozzle comes in contact with the port and is pushed against a rubber ring which is placed under the nozzle to prevent air leakage. The measurements of pressure at tap #3 and a point downstream of the nozzle at various known flow rates can be subsequently used for calibration of the nozzle.

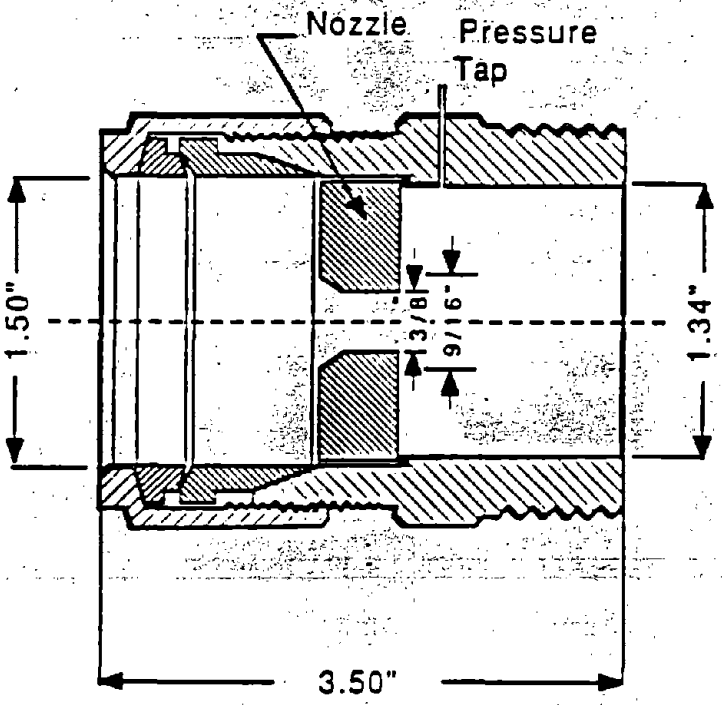

Figure 3.6 Position of the flow metering nozzle in the tube connector mounted at the exit port

Before describing the performance of the chamber in general, the monodisperse aerosol generators and the instruments used for the filter penetration measurements will first be discussed.

3.2 Particle Generation Devices

In the case of generating monodisperse submicron particles, the desired aerosol material, DOP for the liquid particles and NaCl for the solid particles, is first dissolved in a suitable solvent-usually alcohol in the case of DOP and water in the case of NaCl, and placed in an atomizer to generate a polydisperse spray of droplets. The droplets are then allowed to evaporate to remove the volatile solvent and obtain a polydisperse aerosol of the dissolved aerosol material in the solvent. A portion of the produced polydisperse aerosol is then passed through a Differential Mobility Analyzer (DMA) or Electrostatic Classifier to generate monodisperse particles of a size determined from the operating conditions of the DMA.

Meanwhile, in the case of generating monodisperse particles equal or larger than 1μm in diameter, use was made of the vibrating Orifice Aerosol Generator which operates on the basis of controlled disintegration of a liquid jet of the aerosol solution through a small vibrating orifice to

produce uniform droplets.

A detailed description of the above generators and their operation is given below.

3.2.1 Condensation Aerosol Generator

A polydisperse aerosol of DOP particles is produced by an atomization condensation aerosol generation technique. A schametic diagram of the generator is shown in Figure 3.7. In this technique, as described by Liu and Lee (1975), a stream of volatile solution of DOP and alcohol is disintegrated into a polydisperse spray of droplets by a high velocity air jet. The atomizer is of the collison atomizer design except that the waste liquid is accumulated in a waste reservoir instead of being allowed to drain back into the feed liquid reservoir.

The aerosol is then passed through a glass tube whose upper part is heated by a heating tape to vaporize the droplets. The vapor subsequently condenses to form moderately monodisperse droplets. In order to provide nucleation sites for condensation, a small amount of anthracene (0.01% of DOP concentration by weight) was added to the DOP solution. The anthracene particles do not vaporize in the heating section since their boiling point is much higher than that of DOP and remain as the condensation

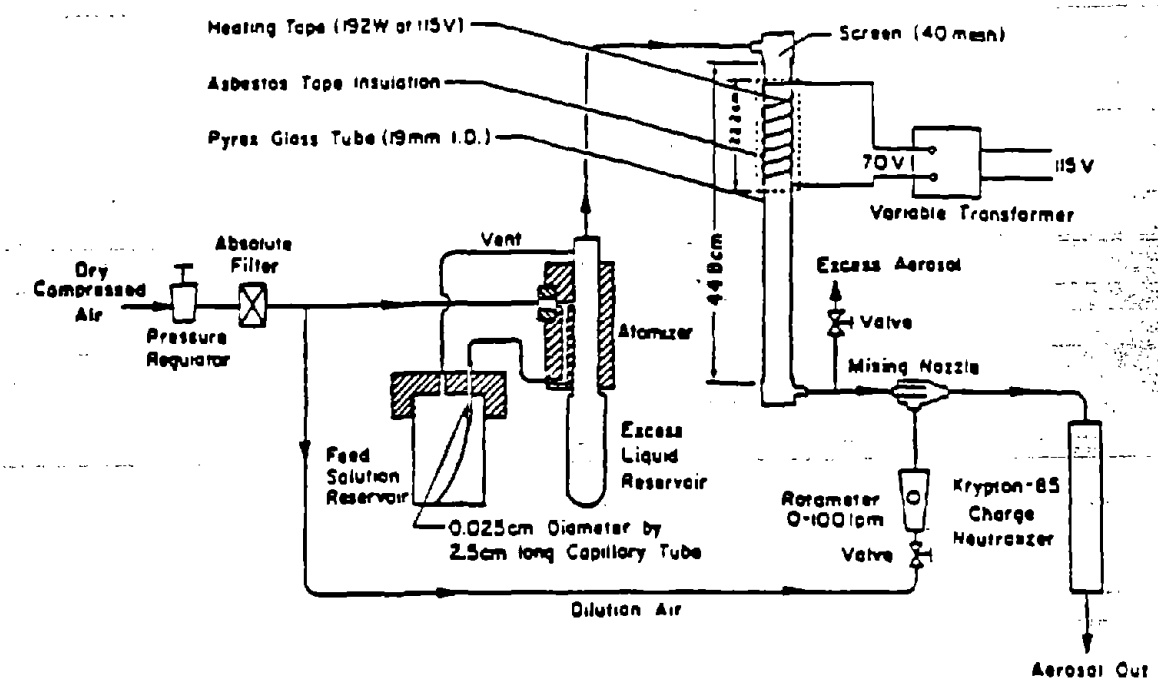

Figure 3.7 Schematic diagram of the condensation aerosol generator used for generating submicron DOP particles

nuclei for the DOP vapor.

Because of the very high particle concentration of the generated aerosol (of the order of 10^7 particles/cm^3), only a small fration of the aerosol flow was used and the remaining flow was exhausted through the "excess aerosol" line. The output aerosol was then passed through a neutralizer to attain Boltzmann charge equilibrium. The neutralizer contains a 2mCi Kr-85 source whose performance has been investigated by Liu and Pui (1974a).

The size distribution of particles in the aerosol is a function of the DOP concentration in the feed solution. Several solutions with various DOP concentrations were prepared according to the experimental measurements of Lee (1977) who determined the size distribution of the generator output aerosol as a function of the DOP concentration. Lee's experimental results are presented in tabulated form in Table 3.1 with D_{gn} and σ_{gn} being the aerosol geometric number mean and standard deviation, respectively.

Table 3.1

Particle Size Produced by Condensation Aerosol Generator as a Function of DOP Concentration (Lee (1977))

DOP Volume Concentration %	Geometric Number Mean Diameter μm	Geometric Standard Deviation
0.005	0.035	1.69
0.013	0.05	1.54
0.037	0.07	1.52
0.1	0.1	1.42
0.3	0.15	1.37
0.67	0.2	1.39
2.1	0.3	1.37
8.3	0.5	1.34
20.0	0.7	1.19
55.0	1.0	1.18
100.0	1.3	1.15

3.2.2 Electrostatic Classifier

This instrument was used in conjunction with the condensation aerosol generator to produce monodisperse submicron particles. A schematic diagram of the classifier is shown in Figure 3.8. The polydisperse, charge-equilibrated aerosol from the generator is introduced into the differential mobility analyzer where singly charged particles within a narrow mobility range are extracted. Liu and Pui (1974b) and Knutson and Whitby (1975) have shown that the mean aerosol electrical mobility of the extracted aerosol is related to the operating conditions and dimensions of the classifier by the following equation,

$$Z_p = [q_c + \frac{1}{2}(q_a - q_s)] \frac{\ln (r_2/r_2)}{2\pi V L'} \qquad (3.1)$$

where q_c is the flow rate of clean sheath air in the classifier, q_a and q_s are the polydisperse and monodisperse aerosol flow rates, respectively, r_1 and r_2 are the inner and outer radii of the classifier, L' is the length of the precipitating electrode between aerosol inlet and outlet, and V is the voltage difference between the inner and outer electrodes. Having obtained the electric mobility of a particle from equation (3.1), its diameter can be determined

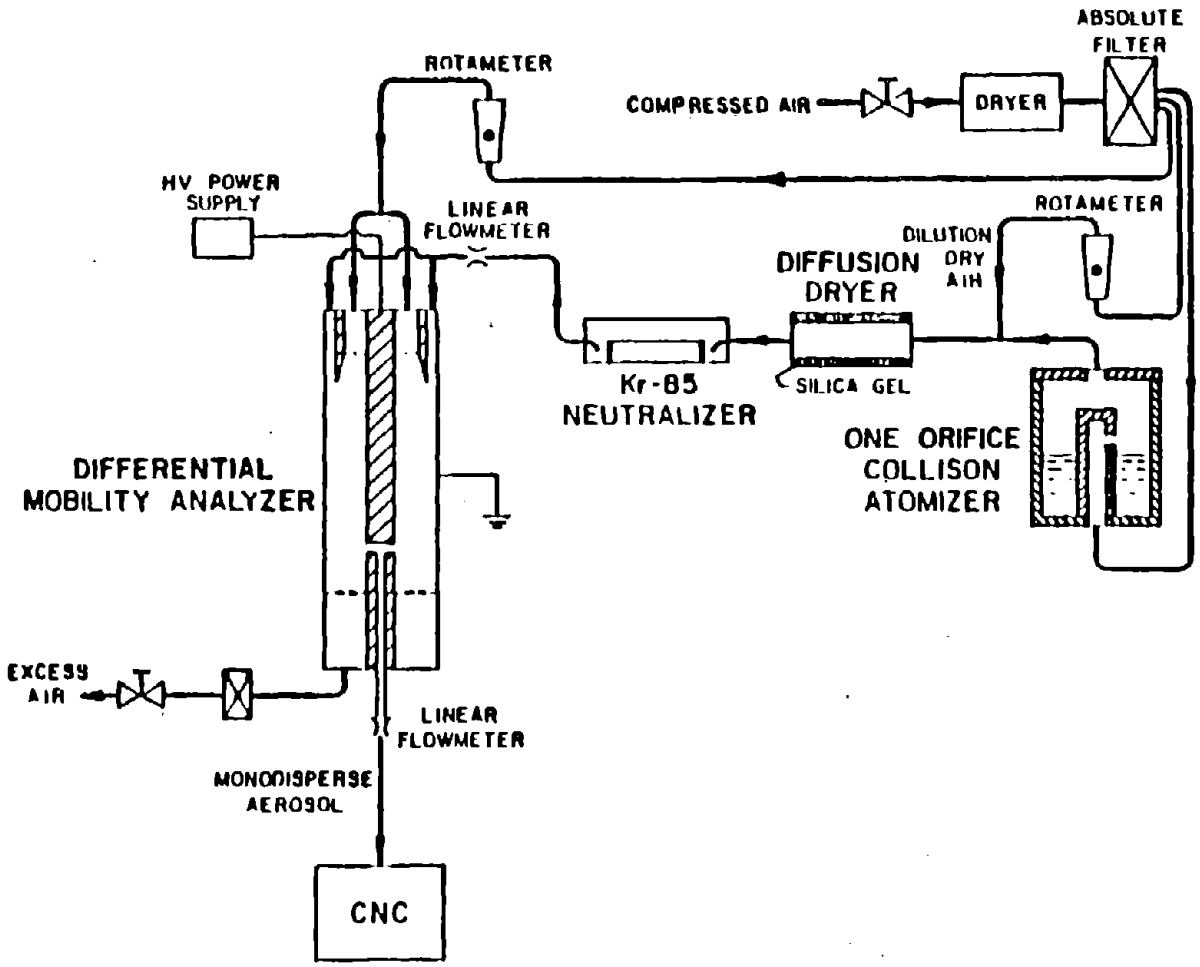

Figure 3.8 Schematic diagram of the differential mobility analyzer

from the following equation assuming Stokes drag on the particle,

$$Z_p = \frac{n_p e c}{3\pi\mu d_p} \tag{3.2}$$

where n_p is the number of charges on the particle and e is the elementary unit of charge. The uncertainty in the calculated particle diameter can be reduced to less that 2% if the flow rates, voltage and dimensions of the classifier are accurately known. The electrostatic classifier used in this study was a prototype designed in and made for the Particle Technology Laboratory of the University of Minnesota. The pertinent dimensions of this particular unit are

$$r_1 = 0.95 \text{ cm} \tag{3.3a}$$

$$r_2 = 1.90 \text{ cm} \tag{3.3b}$$

$$L' = 45.48 \text{ cm} \tag{3.3c}$$

if the polydisperse aerosol flow rate at the classifier inlet, q_a, is kept constant and equal to that of the extracted monodisperse aerosol, q_s, equation (3.1) can be simplified as

$$Z_p = \frac{q_c \ln (r_2/r_2)}{2\pi V L'} \tag{3.4}$$

Substituting the values of r_1, r_2, and L' from equations (3.3a)-(3.3c) in equation (3.4) gives

$$Z_p = 0.0406 \frac{q_c}{V} \qquad (3.5)$$

or

$$V = 0.0406 \frac{q_c}{Z_p} \qquad (3.6)$$

where q_c is in liters per minute, V is in volts, and Z_p is in $cm^2/v.s$. Note that the rod voltage necessary for extracting singly charged monodisperse particles of desired size is independent of the aerosol or sample flow rate as long as they are maintained equal to one another. In the case of particles below 0.1 μm in diameter, the clean air and the aerosol or sample flow rates were maintained at 20 and approximately 2 liters per minute, respectively, while in the case of particle diameters in the range of $0.1 < d_p \leq 0.5$ μm , the flow rates were respectively 7 and 0.7 liters per minute. Similarly, monodisperse particles of 0.7 μm in diameter were also generated by maintaining the clean air flow and aerosol or sample flow rates at 4 and 0.4 liters per minute, respectively. The above clean air flow rates were chosen so that the calculated values of the rod voltage were within the range of the available DC power supply which was from 0 to 12,000 volts. Tables 3.2 and 3.3

Table 3.2 DMA rod voltage setting for extracting monodisperse singly-charged particles of diameter Dp<0.1 um with qc=20 Lpm and qa=qs

Dp,μ	V, volt
0.035	444.7
0.040	572.7
0.045	714.2
0.050	868.4
0.055	1035.6
0.060	1214.6
0.065	1405.0
0.070	1606.0
0.075	1817.2
0.080	2038.4
0.085	2268.4
0.090	2507.2
0.095	2754.7
0.100	3010.0

Table 3.3 DMA rod voltage setting for extracting monodisperse singly-charged particles ranging in diameter from 0.15 to 0.5 um with qc=7 Lpm and qa=qs

Dp,μ	V, volt
0.15	2062.7
0.20	3235.4
0.25	4507.1
0.30	5840.0
0.35	7213.9
0.40	8617.5
0.45	10039.0
0.50	11476.1

list values of V against D_p for singly charged particles below and above 0.1 μm in diameter, respectively.

As shown by equation (3.2), a doubly charged particle can have the same electric mobility as a singly charged particle of half its size. Therefore, these larger particles are also extracted by the mobility analyzer along with the smaller single charged particles. As a result, the monodispersity of the extracted aerosol can be reduced considerably if the concentration of these doubly charged particles is significant. An experimental method for reducing the number concentration of these doubly or multiply charged particles in the monodisperse aerosol of singly charged particle is described below in section 3.5.

3.2.3 Vibrating Orifice Mondisperse Aersosl Generator

This generator, described by Berglund and Liu (1973), was developed to provide a means for generating highly monodisperse aerosols of accuratley known particle size in the range of 0.5 to 50 μm diameter with an average geometrical standard deviation of 1.014. The device is shown in Figure 3.9. It makes use of the controlled disintegration of a liquid jet through a small vibrating orifice to produce uniform droplets. The droplets are then dispersed with a small turbulent jet and mixed with a much larger volume of

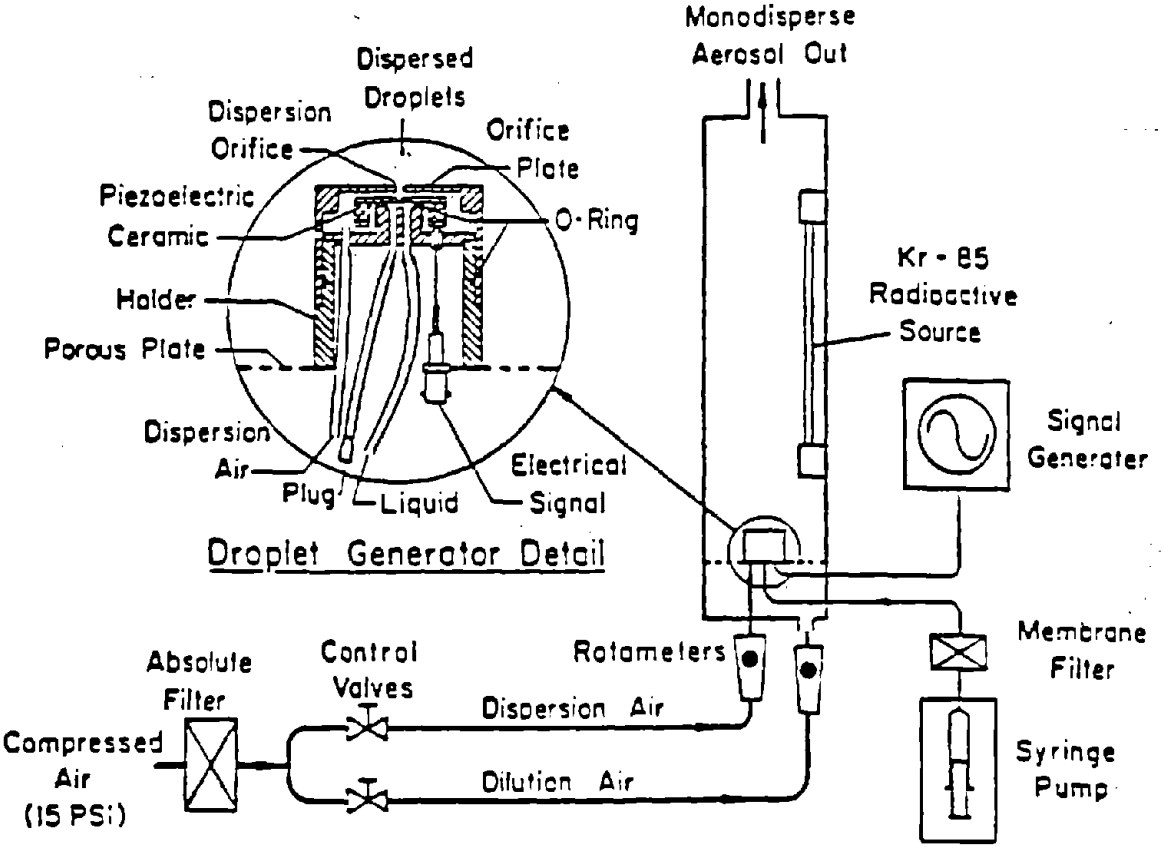

Figure 3.9 Schematic diagram of the vibrating orifice monodisperse aerosol generator used for generating DOP particles larger than 1μ in diameter

filtered air to form a monodisperse aerosol. The diameter of the liquid droplet particles from the vibrating orifice generator can be calculated from the liquid flow rate, Q, and the disturbance frequency, f, by the following formula:

$$D_d = \left(\frac{6Q}{\pi f}\right)^{2/3} \qquad (3.7)$$

when the liquid droplet is non-volatile, the aerosol particle diameter is equal to the droplet diameter; however, when a nonvolatile solute is dissolved in a volatile solvent, the aerosol particle diameter is given by

$$D_p = C^{2/3} D_d \qquad (3.8)$$

where C is the volumetric concentration of a non-volatile solution in a volatile solvent. Table 3.4 below summarizes the operating characteristics of the aerosol generator.

Table 3.4 Operating characteristics of the vibrating orifice aerosol generator (Liu (1977))

Diameter of Liquid Orifice μ	Nominal Frequency KHZ	Droplet Diameter μ	Particle Diameter μ	Nominal Concentration #/cc
5	450	15	0.6-15	273
10	225	25	1.0-25	137
20	60	40	1.8-40	36

The vibrating orifice generator was used in the present study to generate monodisperse DOP particles equal or larger than 1μm in diameter. The electric charge on particles, resulting from disintegration of the liquid jet was reduced to the Boltzmann charge equilibrium by passing the monodisperse aerosol through a Kr-85 neutralizer that could be mounted vertically on the device.

3.3 Particle Size Distribution Measuring Devices

Since the particle penetration through any filter depends stronly on the particle size and its upstream and downstream concentrations, any error in the true measurement of the these quantities would lead to incorrect penetration values. Therefore, it is very important for the measuring instruments to be well calibrated so that the true particle size and concentration could be obtained from the measurements. But as often is the case in Aerosol Science, it is quite possible for two different instruments to give distinctively different size distributions for the same aerosol. This behavior, however, could yield different penetration curves for the filter depending on the instrument used.

Therefore, as one of the objectives of the present study, a comparison of penetration characteristics of monodisperse particles through respirator filters as measured by two commonly-used instruments, namely, a laser optical particle counter and an aerodynamic particle sizer was conducted. Although these instruments are able to measure the size as well as concentration of particles in an aerosol, but in this study only their concentration measuring capability was utilized as the test aerosol was monodisperse of known particle size. The penetration

measurements made by the two instruments were also compared to those obtained by a condensation nucleus counter which is capable of measuring only the particle concentration.

In addition to the above measuring devices, another instrument which was used extensively only in the preliminary test runs was an electrical aerosol detector to measure the particle concentration in the test chamber for evaluating its performance.

Below, a detailed description of the above instruments is given.

3.3.1 Condensation Nucleus Counter (CNC)

This instrument is often used to measure the number concentration of submicron aerosol particles which are too small to be detected by other instruments. It accomplishes this by passing the submicron aerosol aerosol through a vapor which condenses on the tiny particles to form droplets. The droplets are large enough to scatter a detectable amount of light when they pass through a light beam. The final size of a droplet is nearly independent of its original size over a wide range of particle sizes so that the light scattered is a function of number concentration only and not of size distribution.

The CNC used was the TSI Model 3020 (TSI Incorporated, 500 Cardigan Road, St. Paul, MN 55164). Figure 3.10 shows a schematic diagram of the instrument. It consists of a saturator kept at 35^{o}C. The aerosol stream containing the particles to be detected is first passed through this saturator to cause the air stream to be saturated with the vapor of butyl alcohol. The air stream is then passed through a condenser kept at 10^{o}C within which the alcohol vapor becomes supersaturated and condenses on the aerosol particles. By this means, the aerosol particles of a size below the range that can be detected by light scattering i.e. below approximately 0.1 μm in diameter can be grown to a large enough size (approximately 10 μm) to allow easy detection by light scattering. The instrument has been described in detail by Agarwal and Sem (1980).

The condensation nucleus counter has two operating modes ; single particle counting and photometric modes. In the single particle counting mode, the droplets are counted individually as they pass through the light beam. This mode is activated when the particle concentration is in the range of 0.01 to 1000 particles/cm^{3}. The photometric mode is used for particle concentrations from 10^{3} to 10^{6} particles/cm^{3}. In this mode, the total amount of light scattered by all particles in the viewing volume is measured, analyzed and

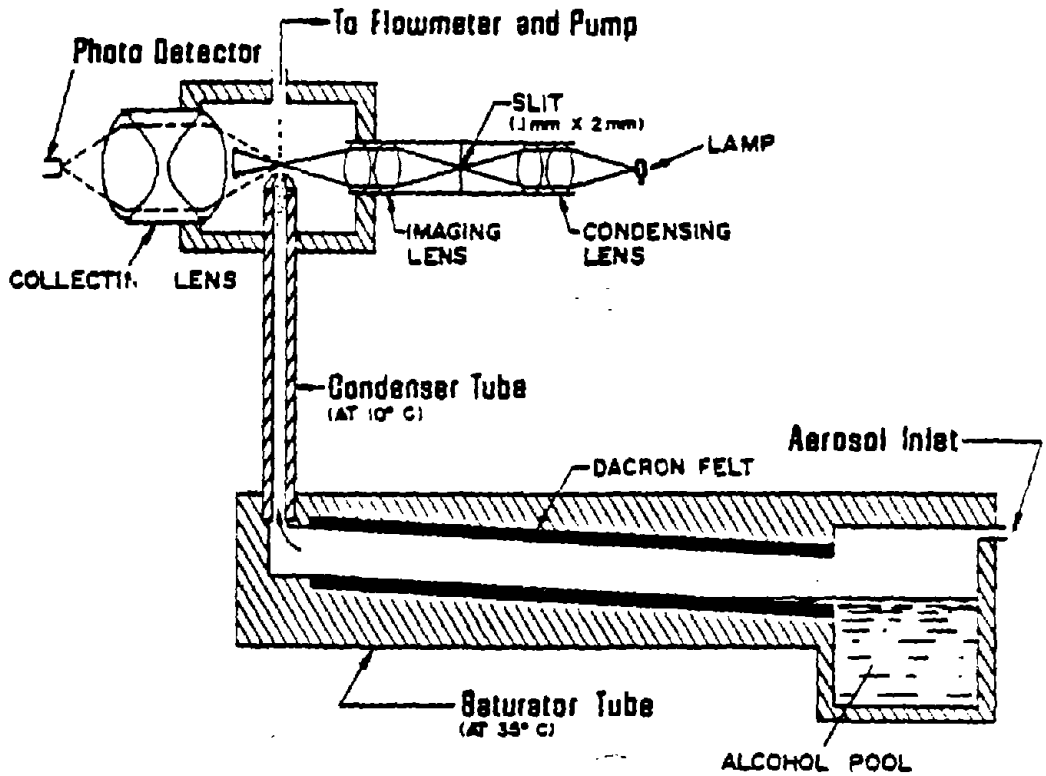

Figure 3.10 Schematic diagram of the condensation nucleus counter

displayed digitally in terms of the number concentration based on the calibration values already implemented in the electronics of the instrument. In the present experiments, the aerosol concentration upstream of a given filter was maintained below 1000 particles/cm^3 so that the single counting mode could be used.

Meanwhile, to account for the presence of two or more particles in the viewing volume at the same time when operating in the single particle counting mode, the indicated concentration can be corrected by the following equation given by Willeke and Liu (1976)

$$N_i = N_t \exp(-N_t Q_s \tau_d) \qquad (3.9)$$

where

N_i : Indicated particle number concentration

N_t : True particle number concentration

Q_s : Aerosol sampling flow rate equal to 5 cm^3/s

τ_d : Particle residence time in the viewing volume equal to 35 μsec according to the manufacturer.

Notice that the true concentration can be obtained only by an iterative procedure. However, one can obtain an approximation to the above equation by replacing N_t in the

paranthesis by N_i as follows,

$$N_i = N_t \exp(-N_i Q_s \tau_d) \tag{3.10}$$

which can be easily solved for N_t.

3.3.1.1 Counting Accuracy

The accuracy of the concentration measurements is strongly dependent upon the total number of particles counted. The fractional uncertainty in particle count, n, is given by the relative standard deviation, σ_r, expressed as

$$\sigma_r = 1/\sqrt{n} \tag{3.11}$$

where $n = NQ_s t_s$

and

N : Particle concentration

Q_s : Aerosol sampling flow rate which is equal to 5 cm^3/s for the condensation nucleus counter

t_s : Sampling time

Note that the percent uncertainty in measurements decreases as more particles are counted. For the case of CNC, the particle count can be enhanced by increasing the sampling time as the sampling flow rate is fixed for CNC.

The longest automatic sampling time on the available Model (3020) is 200 seconds which was used frequently in this work for the concentration measurements downstream of filters.

3.3.2 Laser Optical Particle Counter

The use of single optical particle counters in the filtration studies is becoming attractive because of their capability to make in-situ measurements of the size distribution of particles suspended in gases. In these instruments, a beam of light focused onto a viewing volume is intercepted by passing particles. The amount of light scattered or absorbed by each particle or several particles is measured by a photosensitive detector which generates an electric signal proportional to the amount of the scattered or transmitted light. The analog signal is further analyzed by a Multi-Channel Analyzer (MCA) which transforms the raw data into particle size information and stores it in the appropriate size channel. A detail description of the OPC's principle and application is given by Willeke and Liu (1976).

The laser optical counter used in this study is PMS Model ASAS-300X (Particle Measuring Systems Incorporated, 1855 South 57th Court, Boulder, Co 80301) which is an open cavity, active scattering aerosol spectrometer and uses a

2mw He-Ne laser (wavelength = 632.8nm) operating in the TEM_{00} mode. A schematic diagram of the instrument is shown in Figure 3.11. The aerosol particles surrounded by a clean sheath air are passed through the laser beam and the light scattered by a particle is collected by collecting optics in a narrow angle, 4 to 22 degrees, in the forward direction and focused onto a photodetector module which generates an electric pulse with an amplitude proportional to the amount of the collected scattered light. The pulse is then amplified and transmitted to the Multi-Channel Analyzer for storage and further analysis. A reference signal proportional to the illuminated light intensity is also generated by the reference photodetector module from the light transmitted to the black mirror (99.9% reflectivity).

The sampling flow rate of the ASAS-300X is 1-3 cm^3/s, while the clean sheath air confining the particles to a narrow column before the laser beam flows continously in a closed loop at the rate of 20-30 cm^3/s.

The instrument is designed with four overlapping size range with each divided into fifteen linear size intervals providing up to sixty size channels. Table 3.5 shows the boundaries of each size range and interval of each channel. The measured particle size distribution in any of the four size ranges can be displayed as a histogram on a CRT located

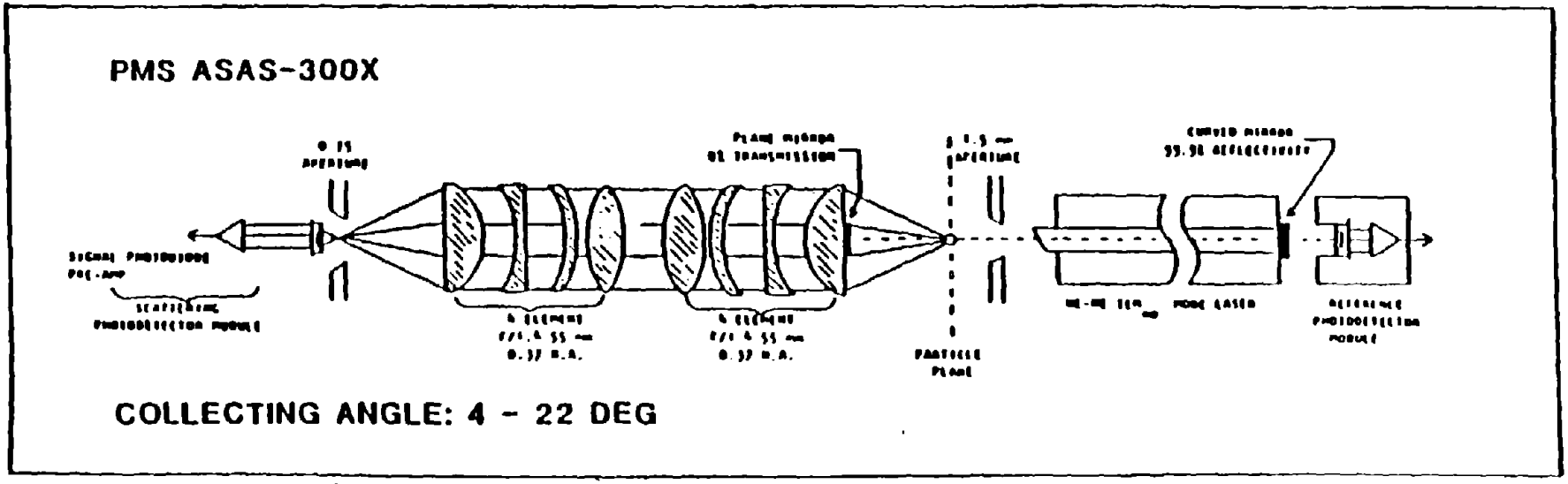

Figure 3.11 Schematic diagram of the PMS ASAS-300X laser optical particle counter

on the front panel of the instrument.

Table 3.5 Particle size boundaries and channel width associated with each size range setting for the PMS ASAS-300X laser optical particle counter

Range Setting	Size Range μ	Interval μ
0	0.60-3.00	0.160
1	0.40-1.00	0.040
2	0.23-0.60	0.025
3	0.15-0.30	0.010

It should be mentioned that the intensity of the scattered light by a particle is a function of not only its size but also the index of refraction of its material, wavelength of the incident light, geometry of the particle and its orientation relative to the incident light. Willeke and Liu (1976) and Liu et al. (1984, 1985) experimentally investigated the response of ASAS-300x to particles of different materials and shapes and Szymanski and Liu (1985) investigated the sizing accuracy of the laser optical particle counters including ASAS-300X.

3.3.3 Aerodynamic Particle Sizer (APS)

This instrument is capable of measuring the aerodynamic size distribution of aerosol particles in real time (the aerodynamic diameter of a particle is the diameter of a unit density sphere having the same settling velocity

as the particle).

The aerodynamic particle sizer used was the TSI Model 3010 (TSI Incorporated, 500 Cardigan Road, St. Paul, MN 55164). A schematic diagram of the instrument is shown in Figure 3.12. A vacuum pump controlled by a feed back loop draws aerosol samples at the rate of 5 liters per minute through an outer nozzle. One liter per minute of the sample aerosol is received by an inner nozzle, while the remaining aerosol flow is filtered and reintroduced as sheath air to confine the aerosol particles to the central portion of the exiting jet where the velocity is uniform. The velocity of particles exiting from the nozzle is measured by a laser velocimetry technique which involves dividing a laser beam (2 mw He-Ne laser) into two beams. A particle passing through the beams generates two light pulses which are transformed into two electric pulses by a photomultiplier tube. The time between pulses is a funtion of the particle velocity which, in turn, depends on the particle aerodynamic diameter. Wilson and Liu (1980) performed experimental and theoretical studies on the particle velocity near the exit of a converging nozzle.

The calculation of the particle aerodynamic diameter from the raw data was performed by a microcomputer (Apple II) which can display the results in terms of the number, surface area, or volume size distribution of

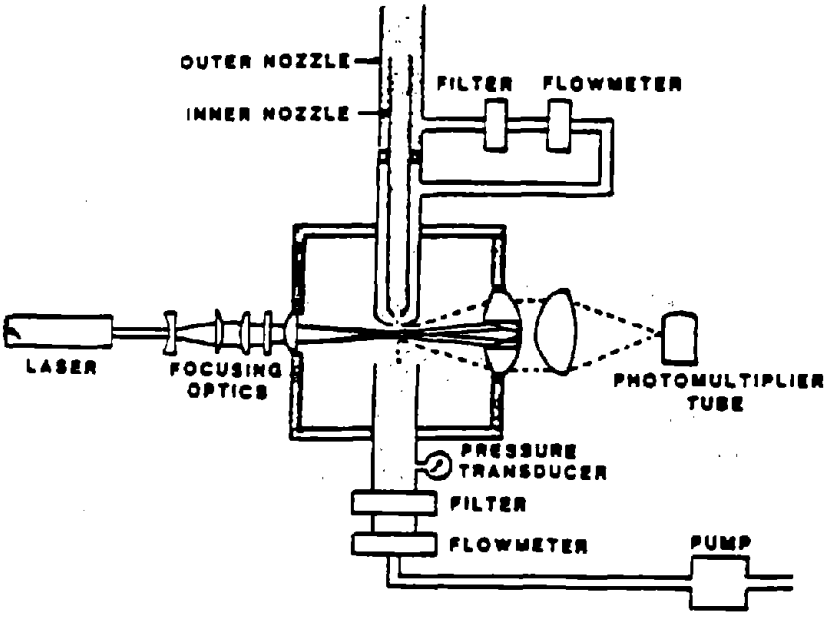

Figure 3.12 Schematic diagram of the aerodynamic particle sizer

particles in the sample aerosol. This instrument is capable of measuring particle aerodynamic diameters from 0.5 to 15 μm.

The coincidence error (presence of more than one particle in the viewing volume) in the concentration measurements can be determined from equation (3.9) with the residence time and aerosol sampling flow rate being 200 nsec and 1 liter per minute, respectively. It was found, however, that the coincidence error in the measurements made by APS in the present study was neglgible. Remiarz et al. (1983) describe the instrument in detail.

3.3.4 Electrical Aerosol Detector (EAD)

A schematic diagram of the TSI Model 3070 EAD (TSI Incorporated, 500 Cardigan Road, St.Paul, MN 55164) which was used in the present study is shown in Figure 3.13. It basically consists of an aerosol diffusion charger and an electrometer current sensor. The aerosol particles surrounded by inside and outside sheath air flows are passed through the diffusion charger where they are positively charged by unipolar ions. The charged particles are then collected by filtration in a Faraday cup where the particle charge is sensed by the electrometer whose output is

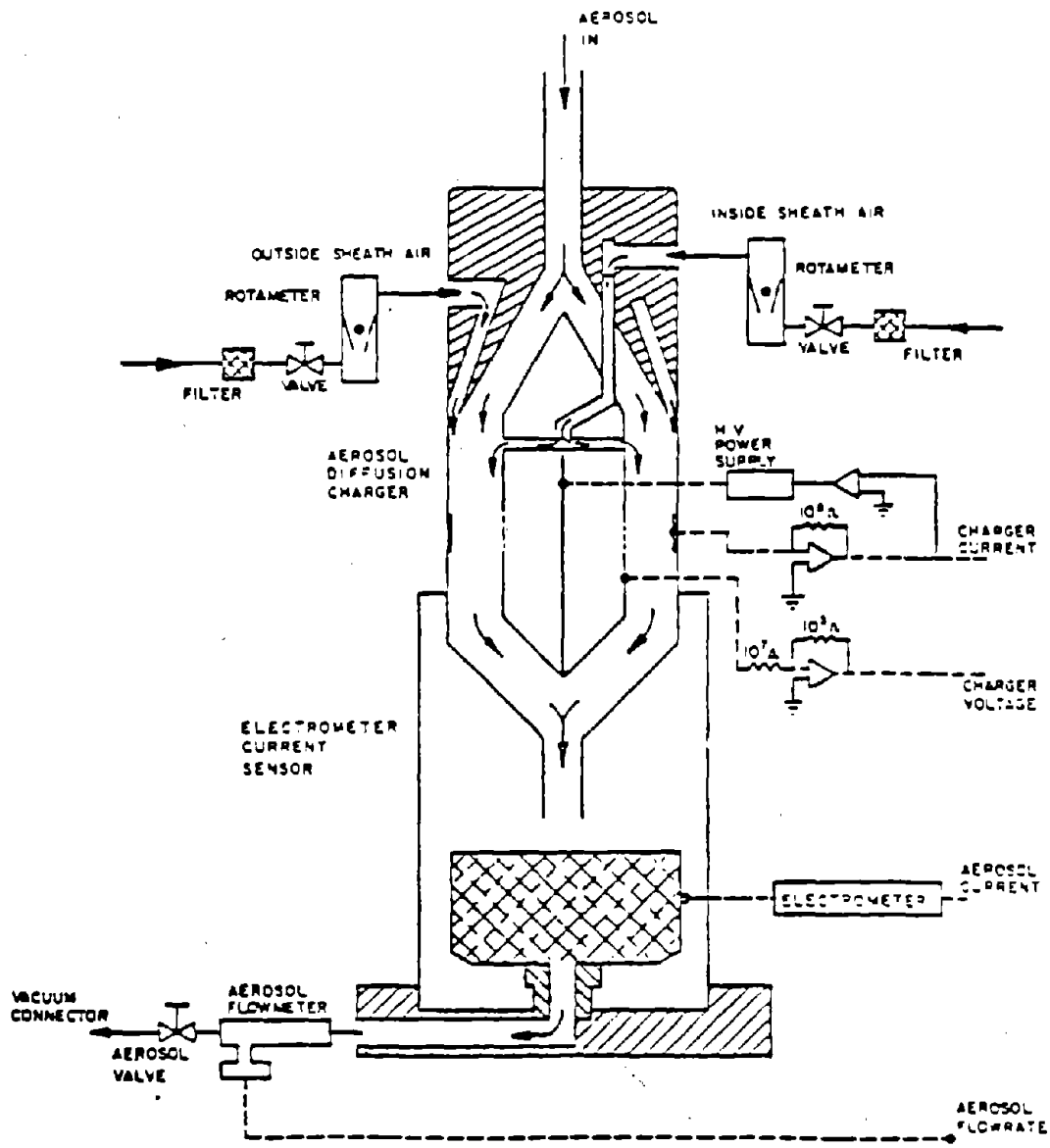

Figure 3.13 Schematic diagram of the electrical aerosol detector

displayed as the aerosol current on the front panel of the instrument. The total air flow rate through EAD is monitored by a thermal mass flow meter and contorlled by a needle valve located downstream of the Faraday cup.

Rubow (1981) performed an extensive evaluation of the sensitivity and amount of particle loss in the aerosol inlet and charger section of the instrument. Further, a detail description of the prototype version of EAD is given by Liu and Lee (1976) and Lee (1977).

3.4 Test Chamber Performance Evaluation Procedure

An extensive evaluation of the performance of the test chamber was conducted prior to the main runs using a polydisperse DOP aerosol containing particles with a mean diameter of 0.5 μm and a σ_g of 1.34 as the test aerosol. The aerosol was generated by the condensation aerosol generator using 8.3% DOP solution and was at the state of Boltzmann charge equilibrium. The electrical aerosol detector and the aerodynamic particle sizer were used to monitor the particle concentration at various stages of the system to determine the amount of particle loss as well as the stability and uniformity of the particle concentration inside the chamber. Meanwhile, the test runs were performed with the 4" filter holder in place holding a 4" Gelman type AE filter, cut out

from a 8X11" filter sheet, as the test filter.

As described previously, the aerosol and clean air flows were assumed to be mixed uniformly in the wake of baffle plates placed specifically for this purpose. The mixed flow was then passed through a flow-straightner structure to eliminate the generated eddies. The resulting flow was assumed to be free of eddies. To verify this assumption, the test aerosol and the clean air supplied from the top of the chamber were introduced to the chamber. The total flow rate was maintained at 50 liters per minute. The upstream probe was then connected to EAD and samples were taken at a fixed location of the probe. The particle concentration measurements were recorded as a function of time by a strip chart recorder. Figure 3.14 shows a strip chart recording of the particle concentration variation with time at about the center of the chamber. As can be seen, there are significant variations in the particle count suggesting that the turbulent eddies generated behind the baffle plates are still present in the flow.

In order to improve the situation, the clean air flow from the top of the chamber was closed and the test aerosol was diluted outside the chamber in a mixing nozzle prior to delivering it to the chamber. The measurements were repeated and the results as shown in Figure 3.15 appear much more stable in comparison with the previous case. It should be

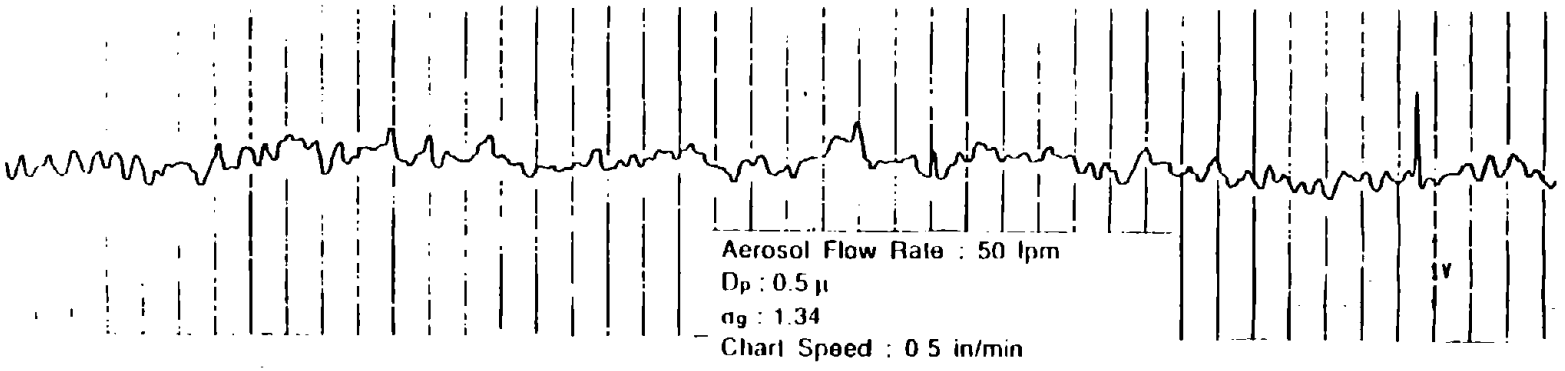

Figure 3.14 EAD recording of variation of particle concentration of a DOP aerosol with time near center of the test chamber when clean air is supplied from top of the chamber

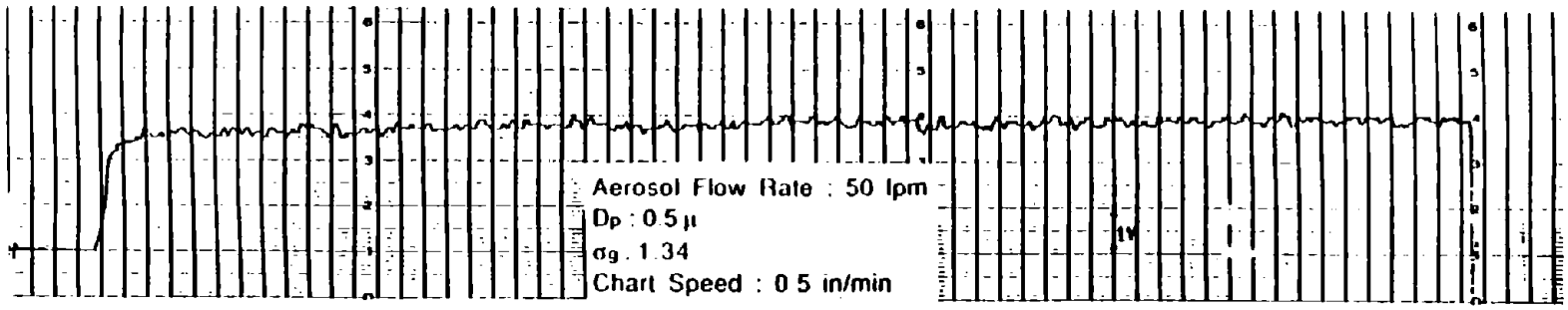

Figure 3.15 EAD recording of variation of particle concentration of a DOP aerosol with time near center of the test chamber when the aerosol and clean air flows are mixed outside the chamber

noted that the occurance of small variations in the concentration measurements is inevitable due to inability to completely eliminate the eddies from the flow. Consequently, it was decided to dilute the aerosol outside the chamber for all the subsequent runs.

In addition, in order to determine the degree of spatial uniformity of the particle concentration across the cross-section of the chamber, the concentration values were measured by CNC at two radial locations of the upstream probe, r = 0.5" and r = 1.5" . The results as illustrated in Figure 3.16 show little difference in the concentration values at the two locations suggesting that the particle concentration is uniform across the chamber upstream of the filter.

It should be mentioned that the aerosol sampling was not performed isokinetically but that seemed to have no appreciable effect on the measurements made in this study as verified by the following experiment. A polydisperse DOP aerosol was generated by the vibrating orifice generator without the electric signal to the oscillator using a 0.1% DOP solution. The aerosol mixed with the dilution air was neutralized in a Kr-85 container before delivering it to the chamber at the rate of 28 liters per minute. The aerosol was then sampled

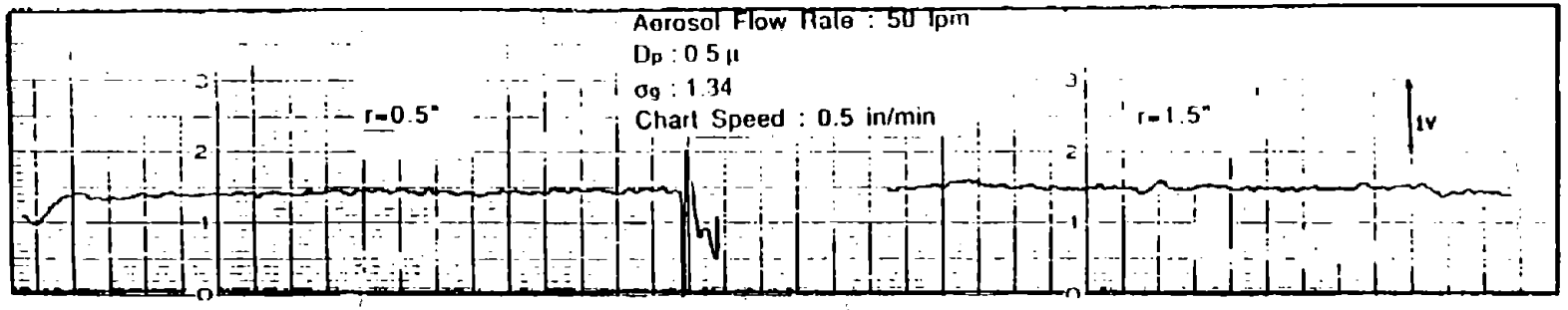

Figure 3.16 CNC recordings of variation of particle concentration of a DOP aerosol with time at two radial locations of the upstream sampling probe

at the chamber inlet as well as at the locations of the upstream and downstream probes in the absence of any kind of filter using the aerodynamic particle sizer. The results expressed in cumulative number distribution are shown in Figure 3.17. Note that the generated aerosol has a bimodal size distribution of particles. The great similarity between the distributions at the three locations testifies to the insignificance of the anisokinetic sampling by the fact that even though, the sampling velocity was nearly the same, the aerosol flow velocities at the three locations were quite different due to the difference in the flow areas. Therefore, the amount of particle loss due to anisokinetic sampling was considered negligible in all the concentration measurements.

Another component of the apparatus which needed to be characterized was the nozzle inside the tube connector mounted on the exit port, as explained previously. The pressure drop across the nozzle was to be correlated against the flow rate. The pressure drop was measured by a pressure transducer (MKS Model 223BD-00010AA-SPCAL; MKS Instruments, Inc., 34 Third Avenue, Burlington, MA 01803) with an operating range of 0 to 5 inch of water. The transducer was connected to a voltmeter (MKS Model PDR-D-1) with a resolution of 1 mv corresponding to 0.0005 inch of water.

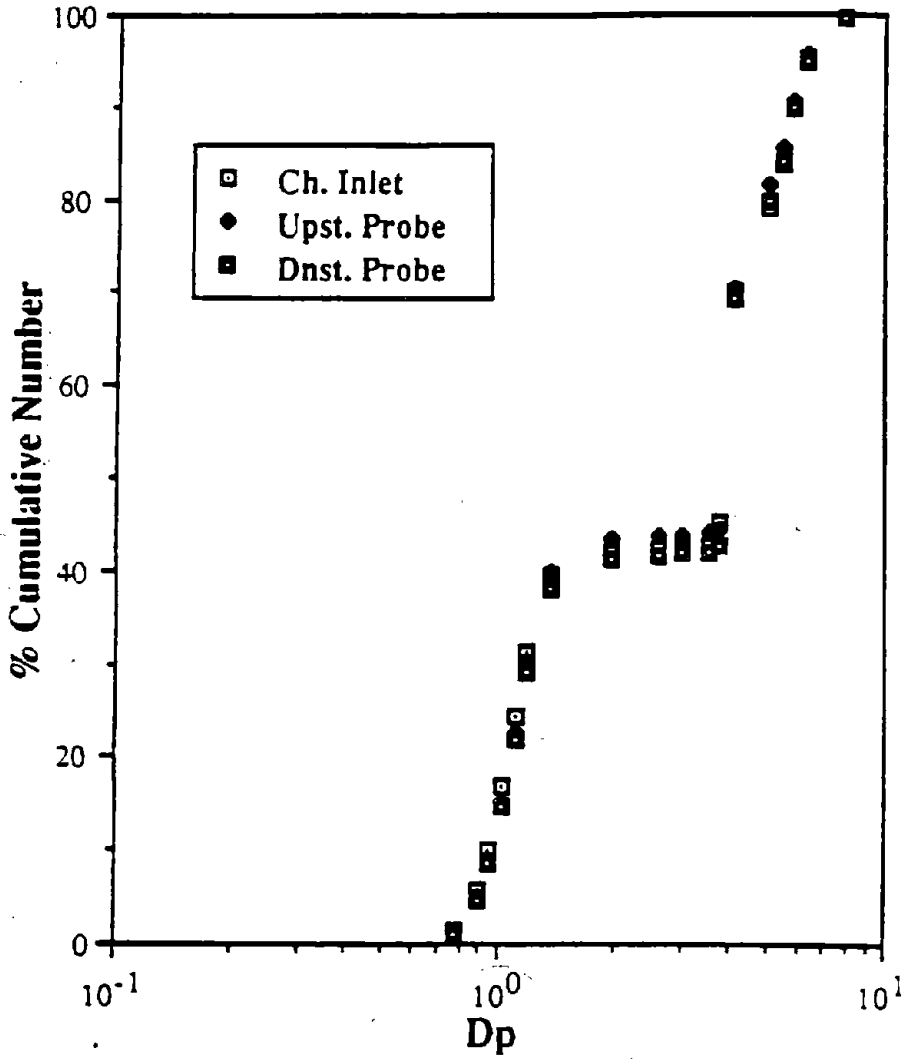

Figure 3.17 APS measurements of size distribution of a polydisperse DOP aerosol at the chamber inlet and locations of the upstream and downstream probes

The flow rate was measured by a rotameter which was calibrated against a standard gas meter over a range of 10 to 70 liters per minute. The measured values of the pressure drop corresponding to different flow rates are plotted in Figure 3.18. Also shown is a plot of the semi-empirical relationship between the pressure drop and flow rate obtained by applying the Bernoulli's equation to the flow in the nozzle. The semi-empirical relationship is

$$Q_t = 9.447 \frac{1}{\sqrt{\rho_a}} \sqrt{\Delta p} \qquad (3.12)$$

where

ρ_a : Air density at atmospheric conditions, lbm/ft^3

Δp : Pressure drop across the nozzle, lbf/ft^2

Q_t : Total flow rate through the nozzle, L/m

The calculated flow rates corresponding to the measured pressure drops were found to be within 5% of the measured values.

Another important feature of the apparatus which was essential to the accuracy of the results was its leak-proof capability. To verify that, all the openings of the test

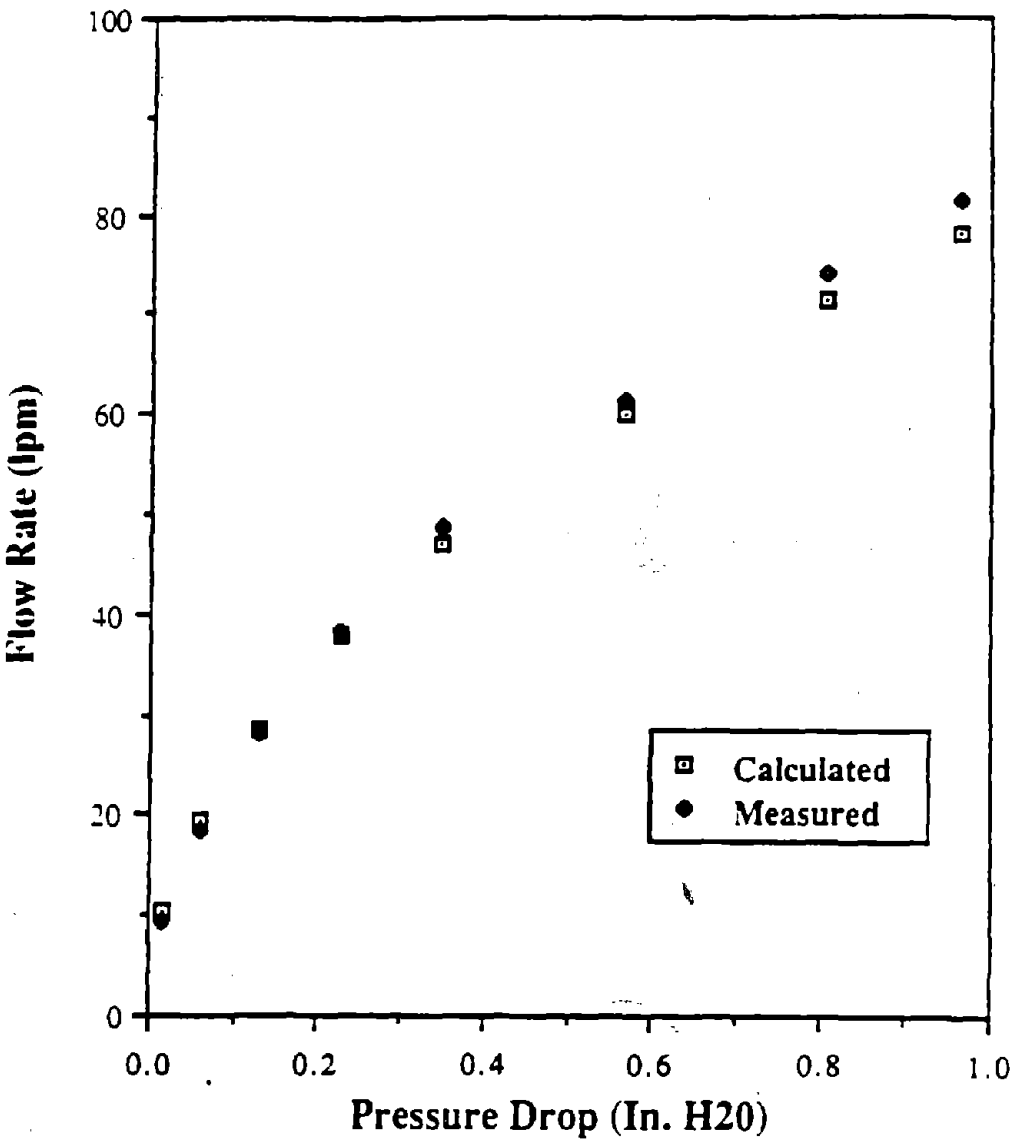

Figure 3.18 Comparison of the calculated and measured values of the aerosol flow rate through the nozzle located at the exit port of the chamber

chamber were plugged with rubber stoppers and the chamber was evacuated by a pump to about 20 inches of mercury. At this time, the pump was turned off and the pressure of the chamber was monitored and recorded as a function of time. No noticeable change in the pressure was observed over a period of three hours.

3.5 Experimental Procedure

The filtration characteristics of five different, commercially-available disposable respirators and a flat filter medium used also in the manufacturing of respirators were to be determined experimentally as a function of the particle size and type (solid or liquid) and flow rate. The respirators were all approved by NIOSH for protection against two or more of hazardous particulates such as dust, mist, fume, and/or asbestos fibers.

A typical experimental run was usually commenced by preparing the monodisperse aerosol generator i.e. the combination of the condensation aerosol generator and electrostatic classifier or the vibrating orifice generator in the case of DOP particles or the combination of a collison atomizer and the electrostaic classifier in the case of NaCl particles. A short period of time was allowed for the generator under consideration to reach at a steady

operation, while its output aerosol line was connected to a high efficiency filter. In the meantime, the respirator selected for testing was glued onto the surface of the face-mask plate by a "hot-melt" type of glue which was applied a few times to obtain a good seal. The plate was then placed inside the chamber. Next, the pressure transducers were zeroed in the absence of any flow in the chamber. At this time, the test chamber was ready for introduction of the monodisperse aerosol to it.

Figure 3.19 shows a schematic diagram of the process. In the case of the electrostatic classifier, the flow rate of the extracted monodisperse aerosol was less than 2 liters per minute and therfore, enough clean air had to be added to the aerosol in a mixing nozzle to increase its flow rate to the desired value of 16, 28, or 48 liters per minute. In the case of the vibrating orifice generator, the desired aerosol flow rate was obtained by simply regulating the dilution air flow valve on the instrument. Note that the flow rate was adjusted such that the pressure drop reading across the nozzle was nearly equal to that obtained from equation (3.12) for a given flow rate. After achieving the desired aerosol flow rate, a short while was allowed for the system to become stable before taking any measurements. Next, the pressure drop across the respirator was recorded

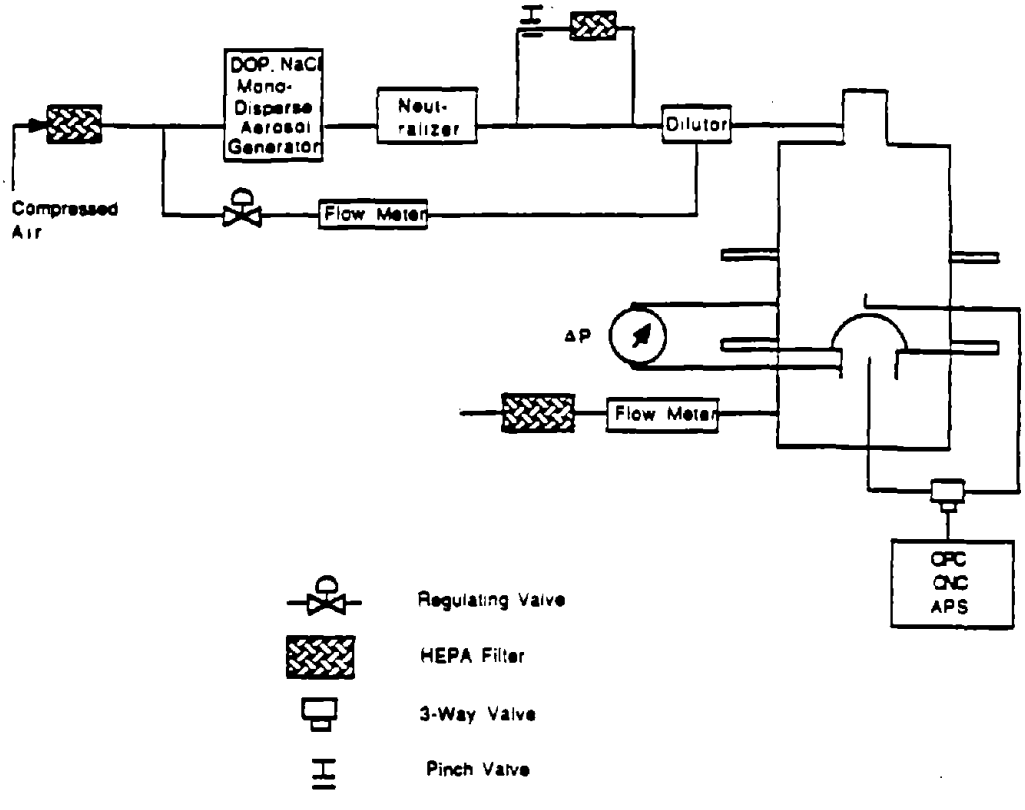

Figure 3.19 Schematic diagram of the process flow

followed by openning the upstream sampling probe line to one or two of the aerosol measuring instruments depending on the size of particles in the aerosol and sensitivity of the instruments. An average of several measurements of particle concentration was recorded as the aerosol particle concentration upstream of the respirator along with a percent variation of the concentration values about the average. The line was then closed by a "pinch" clamp and that of the downstream probe was opened immediately. Similarly, an average of a few measurements downstream of the respirator was recorded also with the percent variation of particle concentration about the average. Next, the upstream concentration was measured once more to determine if there has been any significant change in the previous value during the time taken for the downstream measurements. Very often, the aerosol particle concentration was found to be stable over duration of a complete test but, had that not been the case, the measurements would have been repeated.

The sampling periods for the concentration measurements upstream and downstream of respirator filters were as follows depending on the instrument used : 20 and 200 seconds, respectively, for the upstream and downstream measurements by the condensation nucleus counter and 20 to 60 seconds for the upstream and 5 to 10 minutes for the

downstream measurements by the aerodynamic particle sizer and the laser optical particle counter.

Having completed the concentration measurements of monodisperse particles of one size at above and below the respirator filter, the operating conditions of the aerosol generator and/or the concentration of the particles material in the feed solution were changed to produce monodisperse particles of different size. Once the entire sequence of the particle size was covered, the test was terminated.

It should be mentioned that the same face-mask was used for the entire test and no effect of filter loading such as increasing filter resistance to the aerosol flow was noticed at any time. Nevertheless, when the test was to be repeated at a different flow rate or with particles of different material, a clean respirator was used to eliminate any possible effect of the deposited material on the subsequent test.

As descirbed previously, the electrostatic classifier extracts all particles having equal electric mobility meaning that when a polydisperse aerosol is classified electrically according to the electric mobility of its suspended particles, the supposedly monodisperse aerosol at the exit contains not only singly charged particles of the desired size, but also multiply charged particles of larger size all having the same electric mobility. For the case of

a polydisperse aerosol in bipolar charge equilibrium containing particles smaller than 0.1 μm in diameter, the number of particles carrying two or more units of charge in the output aerosol of the classifier is negligible since over 99% of the particles in this size range carry zero or one uint of charge. Table 3.6 lists the fraction of particles carrying n_p elementary units of charge for several selected particle sizes according to the Boltzmann's charge equilibrium (Pui and Liu (1976)). As can be seen from the table, the fraction of multiply charged particles is not negligible for particles larger than 0.1 μm in diameter. Therefore, when the electrostatic classifier is set to extract monodisperse singly charged particles larger than 0.1 μm in diameter, it will also extract doubly or triply charged particles which have the same electric mobility as the singly charged particles if they happen to exist in the polydisperse feed aerosol. For example, singly charged particles of 0.2 μm diameter have the same electric mobility as doubly charged particles of 0.32 μm diameter.

In the present experiments, in order to reduce the number of charges on particles larger than 0.1 μm in diameter in the polydisperse aerosol produced by the condensation aerosol generator (Figure 3.7), the positions of the heater and neutralizer in the generator were

Table 3.6 Fraction of various size particles carrying np elementary units of charge according to the Boltzmann's charge distribution (Pui and Liu (1976))

Dp,μ	np=-4	-3	-2	-1	0	1	2	3	4
0.01				0.34	99.32	0.34			
0.02				5.23	89.53	5.23			
0.04			0.23	16.22	67.10	16.22	0.23		
0.06		0.01	1.25	21.30	54.88	21.30	1.25	0.01	
0.08		0.08	2.78	23.37	47.53	23.37	2.78	0.08	
0.10		0.26	4.39	24.09	42.52	24.09	4.39	0.26	
0.20	0.32	2.33	9.66	22.63	30.06	22.63	9.66	2.33	0.32
0.40	2.19	5.92	12.05	18.44	21.26	18.44	12.05	5.92	2.19
0.60	3.82	7.41	11.89	15.79	17.36	15.79	11.89	7.41	3.82
0.80	4.83	7.94	11.32	14.00	15.03	14.00	11.32	7.94	4.83
1.00	5.42	8.06	10.71	12.70	13.45	12.70	10.71	8.06	5.42

interchanged. Thus, the output of the atomizer is first neutralized before passing through the heater. The incentive for such a change comes from hypothesis that during the vaporization process in the heater, the multiply charged particles of the charge-equilibrated aerosol, particularly those with more than 2 elementary units of charge, would reach the Rayleigh charging limit. At the Rayleigh limit, the particles become mechanically unstable and split into two or more smaller droplets, each carrying one or two units of charge. Thus, when the vapor condenses, it finds only singly and doubly charged particles. The fraction of doubly charged particles in such a moderately polydisperse aerosol having the same electric mobility as the singly charged particles is small and should not affect significantly the monodispersity of the output aerosol.

Chapter 4

THEORETICAL STUDY

A theoretical study of filtration performance of electret filters composed of rectangular fibers is to be conducted considering the Brownian diffusion, interception, and electrostatic effect as the main particle capture mechanisms. Such study, however, requires knowledge of flow field around a typical rectangular fiber, which is extremely difficult if not impossible to obtain due to the random orientation of fibers, non-uniformity in size and space distribution of fibers in a real filter. Therefore, much simplified representations of a real filter are used for purposes of theoretical studies. The model filter considered in the present work is composed of a staggered array of infinitely long, parallel fibers arranged perpendicular to the fluid flow and was selected mainly because of its simplicity and great success in predicting the performance of mechanical filters composed of circular fibers (Yeh (1972), Lee (1977)). The main feature of this model is its ability to account for the interference effect of neighboring fibers on the flow field around a typical fiber and thus, to incorporate the porosity of real filters in the calculation of the single fiber efficiency and pressure

drop. In addition, in the case of circular fibers, analytical solutions to the problem of viscous flow around a fiber within the model filter are available (Kuwabara (1959), Happel (1959)) and will be presented in this chapter. In the case of rectangular fibers, however, one can only perform a numerical analysis of the flow field at this time since there are no analytical solutions available to the problem of the viscous flow around a rectangular fiber aside from the work of Brown (1984). Brown considered both staggered and rectangular array of symmetrically shaped fibers placed normal to a viscous air flow and obtained a series expression for the stream function by requiring that the rate of dissipation of energy due to viscous drag to be minimal, while satisfying the boundary conditions of the system. But one still has to use a computer or a programmable calculator to calculate the coefficients of the series. Besides, the calculated flow field was found to be not accurate in the region close to the surface of a fiber and thus, may not be suitable for use in calculation of the single fiber efficiency.

The numerical technique which is employed in this study is based on a finite-difference formulation of the flow equations subject to the periodic behavior of the flow within the staggered array model. Once compeleted, the calculation program is used to determine the flow field

around rectangular as well as circular fibers contained in the model filter. In the latter case, the results will be compared with those obtained from the analytical expressions of Kuwabara (1959) for verification of the numerical method. The calculated flow field is then used to determine the single fiber efficiency.

Prior to describing the numerical technique, a brief review of the Kuwabara theory will be given, which will be often referred to in the present study.

4.1 Review of Kuwabara Theory

The theoretical study of viscous fluid flow in a system of staggered array of infinitely long, parallel cylinders (fibers) arranged normal to the flow direction, as shown in Figure 4.1, was considered by Kuwabara (1959). In his approach, Kuwabara argued that the flow field in the system could be divided into identical imaginary cells, each enclosing a fiber, and thus limited the flow analysis to only one cell. Figure 4.2 shows a typical Kuwabara cell model composed of an inner fiber of radius a_f and imaginary outer cylinder of radius a_c such that α, the solid-volume fraction, defined as the ratio of the volume of the fiber to the volume of the cell and given by $\alpha = \frac{a_f^2}{a_c^2}$, is equal to the value of interest. Neglecting fluid inertia forces and

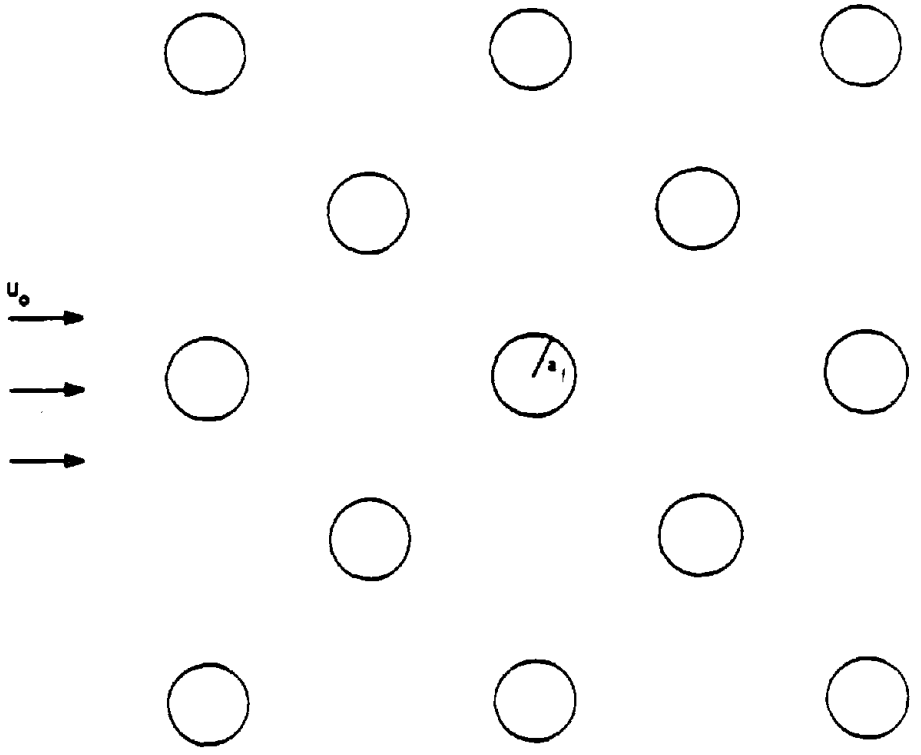

Figure 4.1 Staggered array of cylindrical fibers placed perpendicular to the flow direction

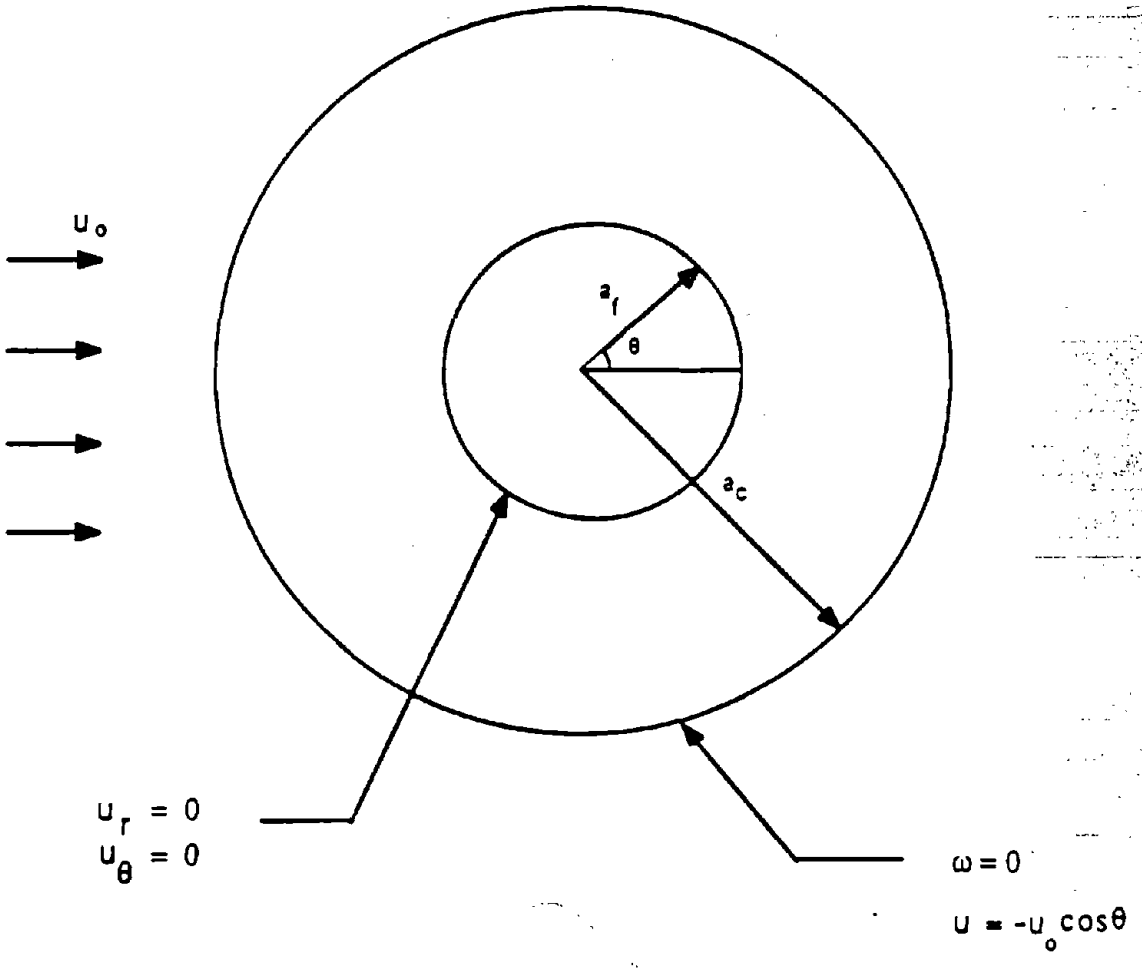

Figure 4.2 Kuwabara cell with assumed Boundary conditions

assuming steady state conditions, Kuwabara described the flow field within the cell by the following equation which is the compressed form of the Stokes' equations expressed in terms of the vorticity, ω, and stream function, ψ,

$$\nabla^2\nabla^2\psi = 0 \tag{4.1}$$

where

$$-\nabla^2\psi = \frac{\partial u_\theta}{\partial r} - \frac{1}{r}\frac{\partial u_r}{\partial \theta} + \frac{u_\theta}{r} = \omega \tag{4.2}$$

$$\nabla^2 = \frac{\partial^2}{\partial r^2} + \frac{1}{r}\frac{\partial}{\partial r} + \frac{1}{r^2}\frac{\partial^2}{\partial \theta^2} \tag{4.3}$$

The fluid velocity components, u_r and u_θ in the directions of r and θ (polar coordinates), respectively, can be obtained from the defining equations of the stream function as,

$$u_r = \frac{1}{r}\frac{\partial \psi}{\partial \theta} \tag{4.4a}$$

$$u_\theta = -\frac{\partial \psi}{\partial r} \tag{4.4b}$$

The boundary conditions assumed by Kuwabara for solution of equation (4.1) are

$$\text{at } r = a_f: \quad u_r = u_\theta = 0 \tag{4.5a}$$

$$\text{at } r = a_c: \quad u_r = -u_o\cos\theta \tag{4.5b}$$

$$\omega = 0 \tag{4.5c}$$

where u_o is the free stream velocity and no-slip condition was assumed on the surface of the fiber. In addition, Kuwabara assumed the vorticity to be zero on the surface of the imaginary cylinder.

A general solution to equation (4.1) is in the form of

$$\psi = \left(\frac{A_k}{r} + B_k r + C_k r \ln r + D_k r^2\right) \sin\theta \qquad (4.6)$$

where A_k, B_k, C_k, and D_k are arbitrary constants which can be determined from the above boundary conditions as follows,

$$A_k = \frac{1}{2K}(1 - 0.5\alpha) \qquad (4.7a)$$

$$B_k = -\frac{1}{2K}(1 - \alpha) \qquad (4.7b)$$

$$C_k = \frac{1}{K} \qquad (4.7c)$$

$$D_k = -\frac{\alpha}{4K} \qquad (4.7d)$$

where K is the hydrodynamic factor given by equation (2.41)

$$K = -0.5 \ln\alpha - \frac{3}{4} - 0.25\,\alpha^2 + \alpha \qquad (2.41)$$

Consequently, the expressions for the velocity components can be obtained from equations (4.4a) and (4.4b) as

$$u_r = \frac{u_o}{2K}\left[2\ln\frac{r}{a_f} - 1 + \alpha + \frac{a_f^2}{r^2}\left(1 - \frac{\alpha}{2}\right) - \frac{\alpha}{2}\frac{r^2}{a_f^2}\right]\cos\theta \qquad (4.8)$$

$$u_\theta = \frac{u_o}{2K}\left[2\ln\frac{r}{a_f} + 1 + \alpha - \frac{a_f^2}{r^2}\left(1 - \frac{\alpha}{2}\right) - \frac{3\alpha}{2}\frac{r^2}{a_f^2}\right]\sin\theta \qquad (4.9)$$

A comparison of the Kuwabara's results with those of others such as Happel's cell model (1959), Kirsch and Fuchs "fan" model (1968), Spielman and Goren (1968) and Lamb's single cylinder model (1932) was conducted by Yeh (1972). He found the Kuwabara analytical results to be in better agreement with his numerical results obtained from the solution of the complete Navier-Stokes equations than the others. Furthermore, the experimental observations of Kirsch and Fuchs (1967) indicated that the Kuwabara theory gave a better prediction of viscous flow over a staggered array of cylinders placed normal to the flow than the Happel theory which is different from the Kuwabara theory only in the treatment of the boundary condition on the imaginary cylinder where Happel assumed the shear stress to be zero.

4.2 A New Approach to Determining Drag on a Cylinder in the Kuwabara Model

The pressure drop, Δp, across a fibrous filter of thickness L_f is equal to product of drag on a unit length of a fiber, F, and total length l_t of fibers contained in a column of unit cross-sectional area of the filter. Thus,

$$\Delta p = F l_t \tag{4.10}$$

where l_t is given by

$$l_t = \frac{\alpha L_f}{\pi a_f^2} \tag{4.11}$$

An expression for F can be obtained from a formulation given by Imai (1951), which is an extension of the Blasius formula to a viscous fluid. Pich (1966) and Yeh (1972) applied the Imai's equation to the Kuwabara cell model and obtained the following:

$$F = \frac{4\pi\mu u_o}{K} \tag{4.12}$$

where μ is the gas kinematic viscosity.

In addition to the Imai's equation, one can also determine the drag on a unit length of a circular fiber by realizing that it is the sum of the shear drag and the form or pressure drag, each expressible in terms of the velocity components. Figure 4.3a shows the shear and normal or pressure stresses on the surface of a circular fiber .

The shear drag is produced by $\tau_{r\theta}$, the only non-zero component of the shear stress tensor for the two dimensional problem under consideration, which is expressed as

$$\tau_{r\theta} = \mu \left[r \frac{\partial}{\partial r} \left(\frac{u_r}{r} + \frac{1}{r} \frac{\partial u_\theta}{\partial \theta} \right) \right]_{surface} \qquad (4.13)$$

where u_r and u_θ are given by equations (4.8) and (4.9), respectively, for the case of the Kuwabara flow field. Having substituted expressions for the velocity components in equation (4.13) and simplifying, one obtains

$$\tau_{r\theta} = \frac{\mu u_o}{K a_f} \left[\frac{3}{2r^3} \left(1 - \frac{\alpha}{2} \right) + \frac{1}{2r} (1 - \alpha) - \frac{1}{r} \ln r - \frac{3\alpha r}{4} \right] \sin\theta \qquad (4.14)$$

the net shear drag, however, is obtained by multiplying the

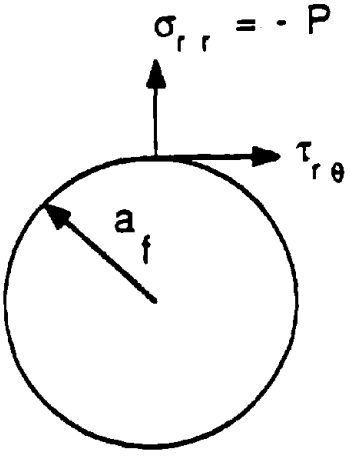

Figure 4.3a Normal and shear stresses on a typical cylindrical fiber

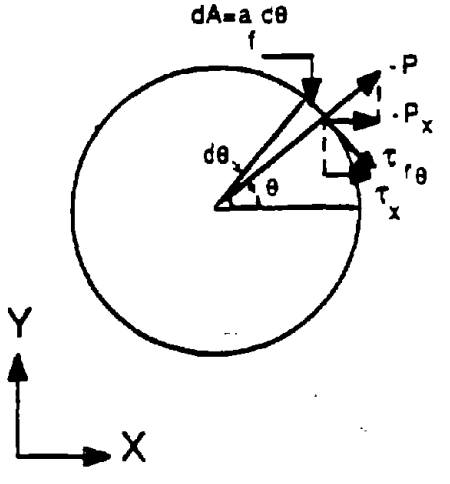

Figure 4.3b Drag-contributing components of the normal and shear stresses acting on an elemental surface area of a cylindrical fiber

x- component of $\tau_{r\theta}$ by an elemental surface area of the fiber (Figure 4.3b) and integrating the result around the surface of the fiber as follows,

$$F_{shear} = \int_0^{2\pi} \tau_{r\theta}\, a_f \sin\theta \, d\theta \qquad (4.15)$$

where F_{shear} is the net shear force acting on the fiber. Substituting equation (4.14) for $\tau_{r\theta}$ in the above equation and carrying out the integration yields

$$F_{shear} = \frac{2\pi\mu u_o}{K} (1 - \alpha) \qquad (4.16)$$

Meanwhile, the other component of the total drag i.e. the form drag is produced from a net pressure force acting on the fiber in a direction opposite to that of the flow. In the case of negligible inertia forces, the pressure function is related to the velocity components through the Stokes' equations by

$$\frac{\partial p}{\partial r} = \mu \left[\frac{\partial^2 u_\theta}{\partial r^2} + \frac{1}{r} \frac{\partial u_\theta}{\partial r} + \frac{1}{r^2} \frac{\partial^2 u_\theta}{\partial \theta^2} \right] \qquad (4.17)$$

and

$$\frac{1}{r} \frac{\partial p}{\partial \theta} = \mu \left[\frac{\partial^2 u_r}{\partial r^2} + \frac{1}{r} \frac{\partial u_r}{\partial r} + \frac{1}{r^2} \frac{\partial^2 u_r}{\partial \theta^2} \right] \qquad (4.18)$$

After substituting for u_r and u_θ from equations (4.8) and (4.9) and performing necessary differentiation and integration operations, pressure is found to be expressed by

$$p = \frac{\mu u_o}{K\, a_f} \left[2r\alpha + \frac{2}{r}\right] \cos\theta + p_\infty \qquad (4.19)$$

where p_∞ is constant of integration. Again, The net pressure force acting along the x-direction is obtained by multiplying the x-component of p by an elemental surface area and integrating the result around the surface of the fiber as follows,

$$F_{form} = \int_0^{2\pi} p\, a_f \cos\theta \, d\theta \qquad (4.20)$$

where F_{form} is the net form drag on the fiber. Substituting for p from equation (4.19) and carrying out the integration gives

$$F_{form} = \frac{2\pi\mu u_o}{K} (1 + \alpha) \qquad (4.21)$$

The total drag is then obtained by simply adding equations (4.16) and (4.21),

$$F = \frac{4\pi\mu u_o}{K} \tag{4.22}$$

which is the same as equation (4.12) obtained from the Imai's formulation.

Although the above approach for determining F is algebraically more involved than using the Imai's formulation, it serves to illustrate the contribution of each component of the drag to the total drag on the fiber. Notice that the form and shear drags are nearly equal for $\alpha<<1$, while for non-negligible values of α, the form drag is always greater than the shear drag.

The drag is often expressed in dimensionless form by the following equation

$$F^* = \frac{F}{\mu u_o} \tag{4.23}$$

where F^* is the dimensionless drag. Substituting for F from equation (4.12) or (4.22) results in the following expression for F^*,

$$F^* = \frac{4\pi}{K} \tag{4.24}$$

This completes the review of the Kuwabara theory. Below, a formulation of the problem of viscous flow in a staggered array of rectangular fibers or any other

symmetrically-shaped fibers based on the assumption of the periodicity of the flow field is presented.

4.3 Formulation of Viscous Fluid Flow in Staggered Array of Rectangular Fibers

Let's consider a system of infinitely long, parallel rectangular fibers arranged staggeredly perpendicular to the direction of flow, as shown in Figure 4.4. After a certain depth from the entrance, the flow is assumed to become periodic, meanning that the flow pattern is repeated after a periodic length along the flow direction. This allows the flow calculations to be limited to a periodic domain such as rectangle ABCD shown in Figure 4.4, since the flow field in each periodic cell is identical. The periodic length, l, in this case is equal to 4h where 2h is the distance between centers of two successive fibers along the flow direction. The flow field in the periodic module ABCD can be obtained from solution of the continuity and Navier-Stokes equations which, for a constant property fluid, are expressed as

$$\frac{\partial u}{\partial x} + \frac{\partial v}{\partial y} = 0 \qquad (4.25)$$

$$\rho \left(u\frac{\partial u}{\partial x} + v\frac{\partial u}{\partial y}\right) = -\frac{\partial p}{\partial x} + \mu\left(\frac{\partial^2 u}{\partial x^2} + \frac{\partial^2 u}{\partial y^2}\right) \qquad (4.26)$$

$$\rho \left(u\frac{\partial v}{\partial x} + v\frac{\partial v}{\partial y}\right) = -\frac{\partial p}{\partial y} + \mu\left(\frac{\partial^2 v}{\partial x^2} + \frac{\partial^2 v}{\partial y^2}\right) \qquad (4.27)$$

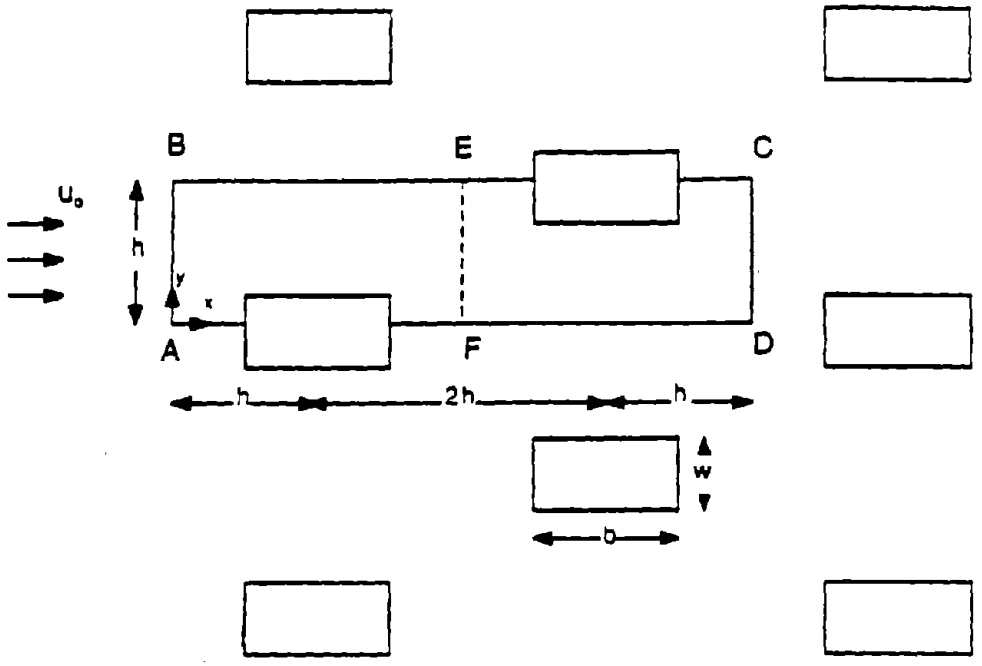

Figure 4.4 Staggered array of rectangular fibers with an aspect ratio of b/w placed perpendicular to the flow direction

where u and v are the velocity components in the x- and y-directions, respectively, p is the pressure, and ρ is the fluid density. The boundary conditions necessary for solving the above set of equations are given by:

on BC and AD :

$$\frac{\partial u}{\partial y} = 0 \qquad (4.28a)$$

$$v = 0 \qquad (4.28b)$$

These equations arise from the symmetry conditions assumed for the x- component of the velocity at the top and bottom boundaries of the domain. Although, there is no explicit information about the velocity components at the inflow and outflow boundaries of the domain, one can write the following equations which result from the assumption of the periodicity of the flow,

$$u(x,y) = u(x+L,y) \qquad (4.29a)$$

$$v(x,y) = v(x+L,y) \qquad (4.29b)$$

where x and y denote respective coordinates of a point on the domain inflow boundary. Also, assuming no-slip condition on the surface of fibers,

on fiber :

$$u = 0 \qquad (4.30a)$$

$$v = 0 \qquad (4.30b)$$

Note that the above boundary conditions are necessary but not sufficient to obtain a solution since they convey no explicit information about the amount of mass flow into or out of the periodic module. Such information, however, can be obtained from the following consideration of pressure. It is apparent that in order for there to be a net mass flow in the positive x- direction, the pressure level must decrease with x. Therefore, pressure does not obey the same type of the periodicity condition as the velocity components. There is, however, another type of periodicity condition for pressure. According to Patankar et al. (1977), pressure in a periodic flow is actually composed of two components; one being periodic, which obeys the same periodicity condition as the velocity components and the other being linear, which reduces linearly in the positive x- direction thus causing the fluid flow. Therefore, the pressure function can be expressed as

$$p(x,y) = P(x,y) - \hat{\beta}x \tag{4.31}$$

where P is the periodic component of pressure such that

$$P(x,y) = P(x+L,y) = P(x+2L,y) = \ldots\ldots\ldots \tag{4.32}$$

and $\hat{\beta}$ is a numerical constant which is regarded as an

assignable parameter, a given value of which will generate mass flow. Thus, in the case of the present problem, an assigned pressure drop of $\hat{\beta}L$ produces some fluid flow in the periodic module at a rate depending on the value of $\hat{\beta}$. Substituting equation (4.31) in equations (4.26) and (4.27) yields

$$\rho \left(u\frac{\partial u}{\partial x} + v\frac{\partial u}{\partial y}\right) = \hat{\beta} - \frac{\partial P}{\partial x} + \mu\nabla^2 u \qquad (4.33)$$

$$\rho \left(u\frac{\partial v}{\partial x} + v\frac{\partial v}{\partial y}\right) = - \frac{\partial P}{\partial y} + \mu\nabla^2 v \qquad (4.34)$$

where ∇^2 in the cartesian coordinate system is given by

$$\nabla^2 = \frac{\partial^2}{\partial x^2} + \frac{\partial^2}{\partial y^2} \qquad (4.35)$$

Equations (4.33) and (4.34) along with the continuity equation (equation (4.25)) constitute a coupled system of partial differential equations which must be solved simultaneously with the boundary conditions given by equations (4.28)-(4.30) and (4.32) for the unknown functions u(x,y), v(x,y), and P(x,y).

It was noted, however, that the flow field in one half of the periodic module ABCD was symmetrical inversion of that in the other half. It is thus possible to halve the domain and consider only one of the half modules, such as module ABEF as shown in Figure 4.4, for the flow as well as

single fiber efficiency calculations. Such consideration yields great savings in computation time and cost. The periodicity conditions are consequently modified as

$$u(x,y) = u(x + \frac{L}{2}, h - y) \tag{4.36a}$$

$$v(x,y) = - v(x + \frac{L}{2}, h - y) \tag{4.36b}$$

$$p(x,y) = p(x + \frac{L}{2}, h - y) \tag{4.36c}$$

notice that the negative sign in equation (4.36b) is included because the y-component of the fluid velocity has opposite directions at the inflow and outflow boundaries of the module ABEF. Also note that the pressure drop necessary for the fluid flow is now $\frac{\hat{\beta} L}{2}$ instead of $\hat{\beta} L$.

It should be noticed that the above formulation is independent of the cross-sectional shape of the fiber and can be applied to rectangular, circular, or any other symmetrically shaped fibers.

A brief review of the numerical technique used in the present study to solve the flow equations is given next.

4.4 Numerical Method

A solution to the partial differential equations expressing the periodic fluid flow around rectangular fibers can be obtained only in a numerical form as an analytical

solution is not currently available. The numerical scheme used in the present study is a finite-difference scheme which involves discretizing the governing differential equations into a number of algebraic equations containing unknown values of the corresponding dependent variables at finite number of locations in the calculation domain, called grids. The descritized equations are then solved simultaneously or iteratively according to a solution algorithm to obtain discrete values of the dependent variables.

The technique used here for discretization of a given differential equation is based on the control-volume formulation which is easy to understand and lends itself to direct physical interpretation. The method is described in detail by Patankar (1980). It basically involves dividing the calculation domain into a number of non-overlapping control volumes, each containing a grid at its center. The differential equation of interest is then integrated over each control volume assuming some mathematical profile for variation of the dependent variable between adjacent grids for evaluation of integrals. The result corresponding to each control volume is an algebraic equation containing unknown values of the dependent variable at the central grid and its immediate neighboring grids.

A detail description of the discretization method and

solution algorithm for solving the resulting equations is given in Appendix B. In addition, details of the calculation program developed for the present study are discussed also in Appendix B.

4.4.1 Viscous Flow Field Around a Rectangular Fiber in Staggered Array Model

Following the control-volume approach as described briefly above, the calculation domain ABEF was divided into several control volumes, as shown in Figure 4.5. The grids are numbered from I = 1 to L1 in the x- direction and from J = 1 to M1 in the y- direction, where L1 amd M1 are integers equal to 36 and 31, respectively for the problem under consideration. Since the boundary conditions are symmetrically inverted at the inflow and outflow boundaries, it is essential to maintain the grid layout symmetric with respect to an imaginary line running parallel to the x-axis through mid-section of the domain. As seen, several control volumes have been placed fairly close to the fiber for more accurate determination of the flow field in the vicinity of the fiber which, in turn, yields more accurate values for the single fiber efficiency. In general, the flow and efficiency calculations were carried out for several values of the filter packing density, fiber aspect ratio, $\frac{b}{w}$,

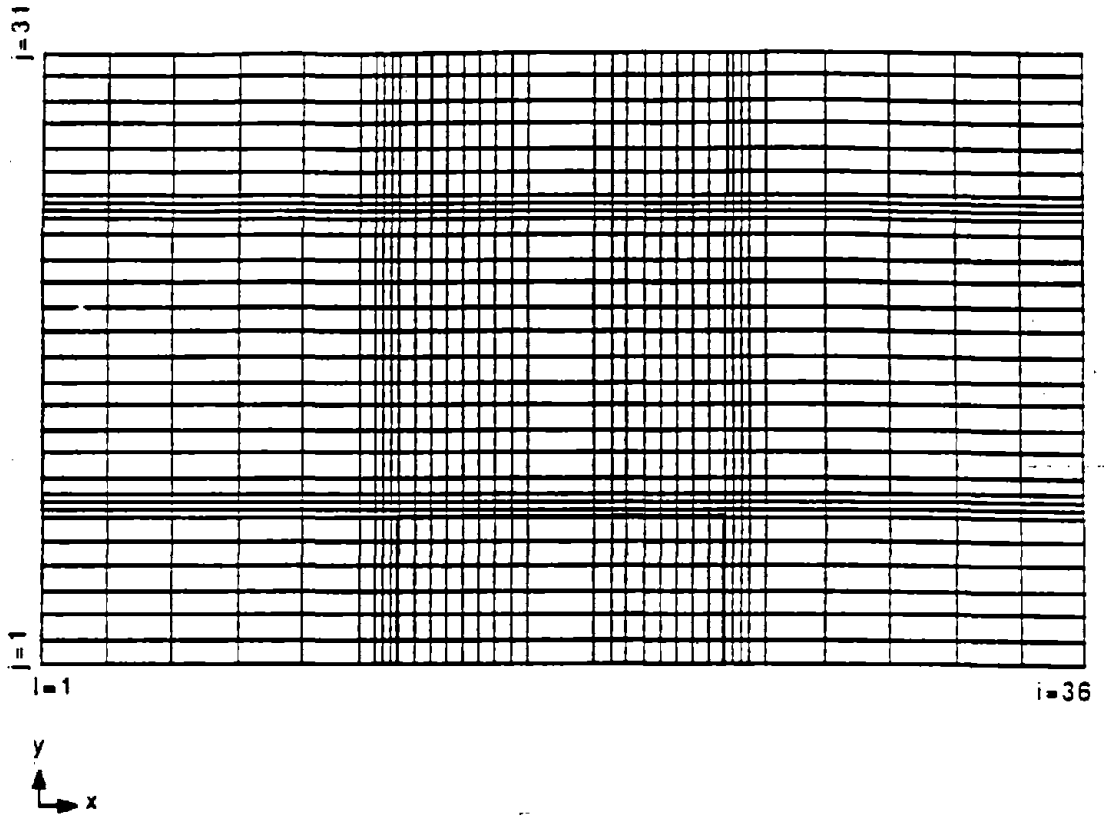

Figure 4.5 Control-volume layout of the calculation domain around half of a rectangular fiber

defind as the ratio of that side of a rectangular fiber which is parallel to the flow direction, b, to that which is normal to the flow direction, w, and other pertinent dimensionless parameters.

A typical flow calculation session usually commenced by specifying a value for $\hat{\beta}$ and allowing the solution algorithm to iteratively calculate values of the velocity components and pressure. The convergance or divergance of the solution depended on the values of the relaxation factors used to retard or expedite the convergance rate and after several test runs with different relaxation factors , a set of values was selected for optimum convergance rate. Figure 4.6 shows a typical calculated flow field around a rectangular fiber with an aspect ratio equal to $\frac{1}{1}$ corresponding to $\hat{\beta} = 600$, $\alpha = 0.08$, and $Re = 0.19$, where Re is the Reynolds number defined as

$$Re = \frac{U_o D_h}{\nu} \tag{4.37}$$

where ν is the fluid kinematic viscosity, U_o is the mean air velocity normal to the inflow boundary, and D_h is the hydraulic diameter of the fiber given by

$$D_h = \frac{2wb}{w + b} \tag{4.38}$$

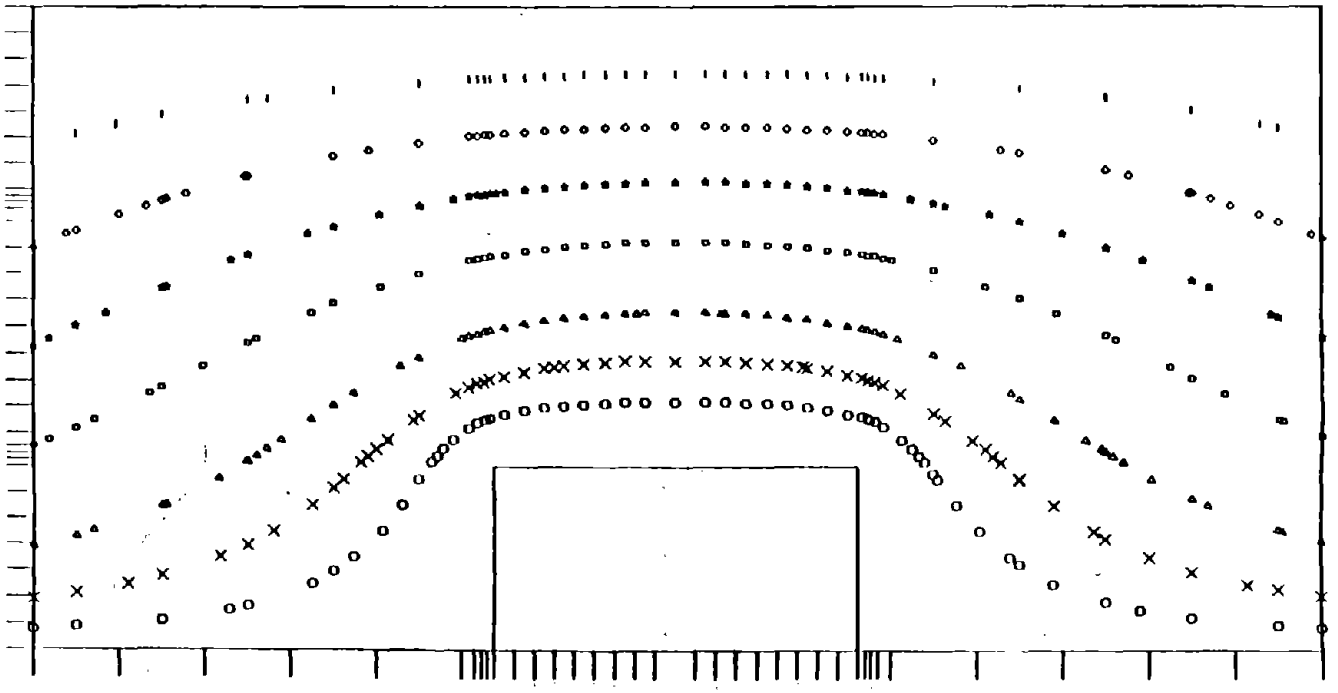

Figure 4.6 Flow streamlines around a rectangular fiber with b/w=1/1 corresponding to β=600, α=0.08, and Re=0.19

Meanwhile, since the pressure drop, Δp, along the domain is caused by the drag on the fiber, one can determine the drag on a unit length of the fiber, F, by multiplying the pressure gradient $\hat{\beta}$ by the domain length and surface area normal to the flow direction as follows,

$$F = \hat{\beta}(L)(h)(1) = \Delta p\ h \tag{4.39}$$

Expressing F in a non-dimensional form according to equation (4.23) yields,

$$F^* = \frac{\Delta p\ h}{\mu U_o} \tag{4.40}$$

the values of F^* for $\alpha = 0.08$ and several values of $\frac{b}{w}$ and Re were obtained and plotted against Re, as shown in Figure 4.7. As can be seen, for $Re \leq 0.2$, the F^* values corresponding to different aspect ratios are almost constant independent of the Reynolds number, while for $0.2 < Re < 1$, the dimensionless drag seems to be a weak but increasing function of the Reynolds number.

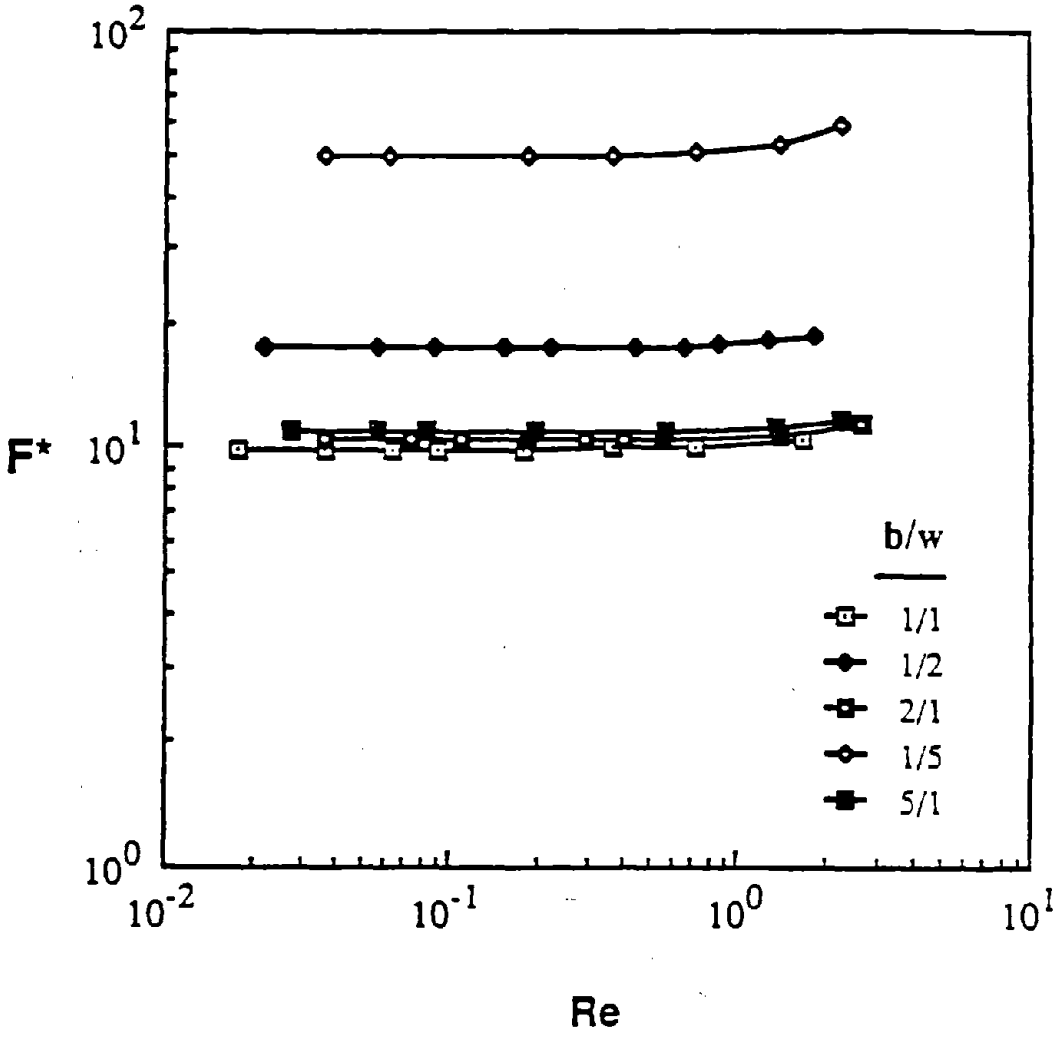

Figure 4.7 Calculated values of the dimensionless drag on rectangular fibers in viscous flows with different Reynolds numbers for α=0.08

4.4.2 Viscous Flow Field Around a Cylindrical Fiber in Staggered array Model

The present numerical method, as mentioned previously, can be applied also to the case of viscous flow in a system composed of staggered array of circular fibers as shown in Figure 4.1. The results of calculations can be then compared with the theoretical predictions of Kuwabara as a means of verifying the accuracy of the numerical method .

Having assumed periodic flow behavior away from the entrance, the flow field calculation could be limited to a periodic module such as that shown in Figure 4.8, which contains half of a circular fiber because of symmetry consideration. The flow equations and boundary conditions associated with this domain are the same as those considered for calculation of the flow field around a rectangular fiber.

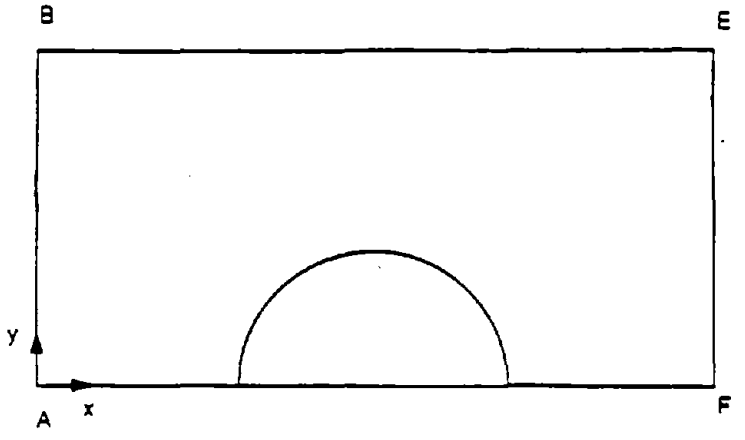

Figure 4.8 Calculation domain considered around half of a cylindrical fiber

As mentioned previously, the numerical technique used in the present study requires dividing the calculation domain into a pre-selected number of control volumes of certain geometry which is compatible with the geometry of the domain and its contents. The obvious choice for the domain under consideration is, of course, a combination of cylindrical and rectangular control volumes. But since, no provision for interaction between two geometrically dissimilar control volumes was considered in the present numerical program, it was decided to use rectangular control volumes for the entire domain including the circular fiber as the conform best to the geometry of the domain as well as rectangular fibers which are of main interest to the present study. This approach, however, requires that the circular boundary of the fiber to be approximated by a "step" model as illustrated in Figure 4.9.

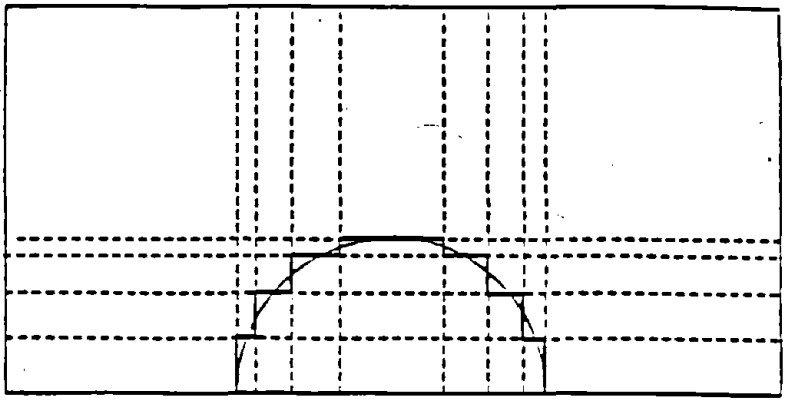

Figure 4.9 "Step" representation of round contour of a half cylinder with a step angle of 11.25 degrees

The steps are basically formed from crossings of the vertical and horizontal faces of control volumes with the surface of the fiber. The model shown in Figure 4.9 is formed with vertical faces crossing the fiber boundary at points having the following angular positions with respect to the forward stagnation point : $1x11.25^{o}$, $3x11.25^{o}$, $5x11.25^{o}$, $7x11.25^{o}$, $9x11.25^{o}$, $11x11.25^{o}$, $13x11.25^{o}$, and $15x11.25^{o}$ and with horizontal faces crossing the fiber at the following angular positions : 0^{o}, $2x11.25^{o}$, $4x11.25^{o}$, $6x11.25^{o}$, and $8x11.25^{o}$. The arbitrary angle of 11.25^{o} is reffered to as the step angle from hereinafter. Note that the vertical and horizontal control volume faces cross the circular fiber at odd and even multipliers of the step angle, respectively. It should be mentioned that the systematic procedure used here is by no means the only method of generating the steps.

Meanwhile, in order to determine the effect of the number of steps used in approximating the circular boundary of a fiber on the calculation results, the step angle was reduced to 5^{o} to obtain a better representation of the fiber contour.

Figures 4.10 and 4.11 illustrate typical calculated flow fields around the same fiber composed of steps corresponding to step angles of 5^{o} and 11.25^{o}, respectively.

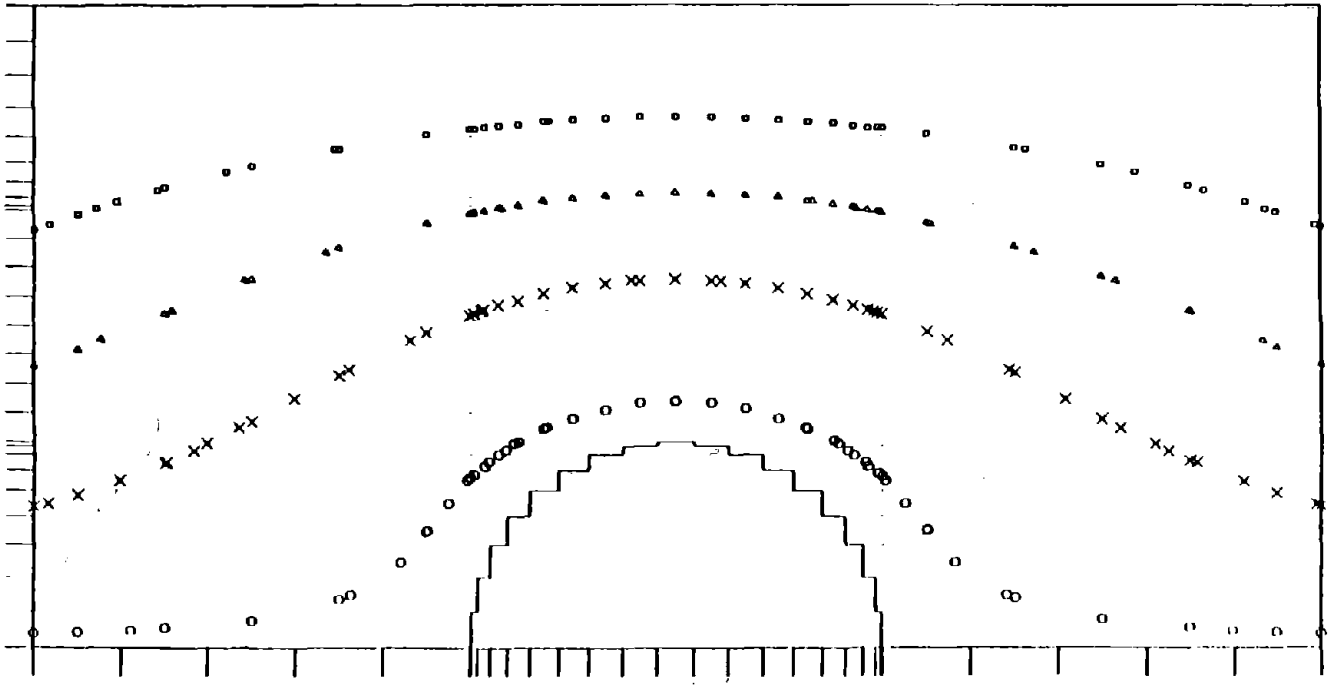

Figure 4.10 Flow streamlines around a cylindrical fiber represented by steps with a step angle of 5 degrees and for β=800 and α=0.08

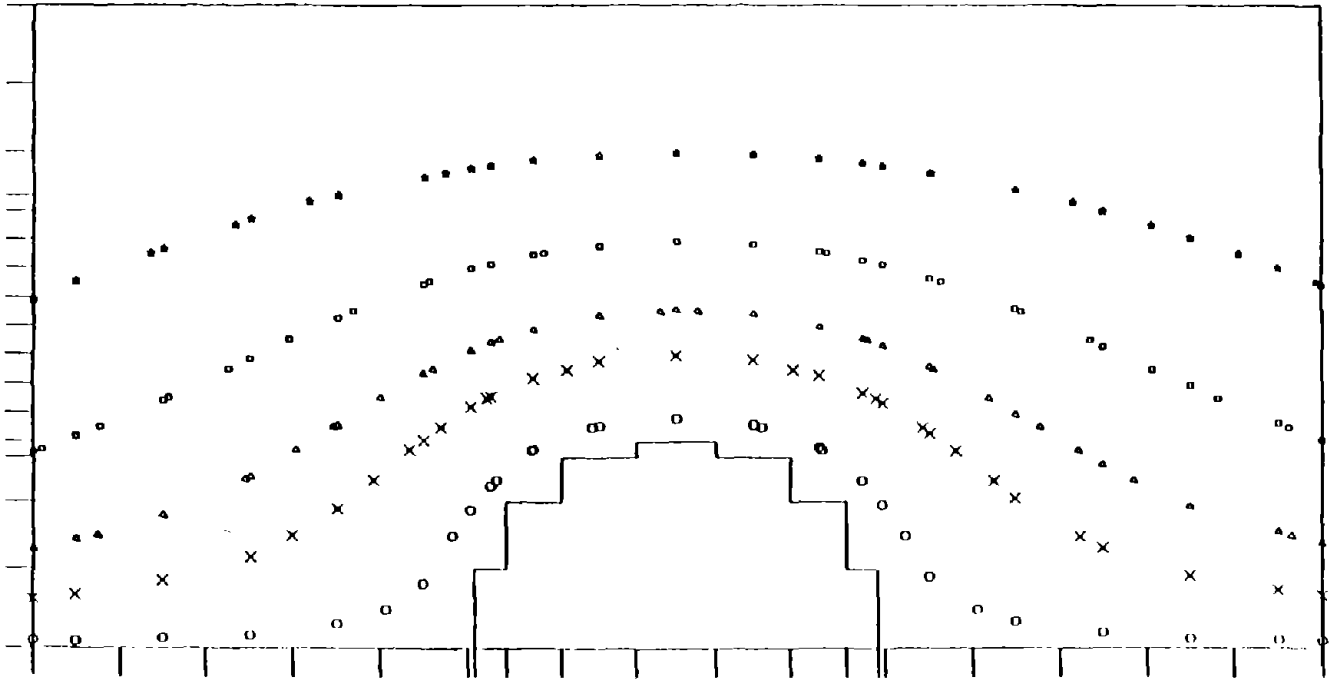

Figure 4.11 Flow streamlines around a cylindrical fiber represented by steps with a step angle of 11.25 degrees and for β=800 and a=0.08

As shown, no apparent differences in the flow fields correponding to the two step angles exist. This agreement is more evident by the plot shown in Figure 4.12 in which values of the dimensionless drag, F^*, as determined from equation (4.40) are plotted against α for both step angles. As seen, the results are in excellent agreement suggesting that the flow field is not sensitive to the number of steps used in approximating the circular fiber. As a matter of fact, in the limit that a circular fiber is approximated by a square (corresponding to a rectangle with an aspect ratio of $\frac{1}{1}$), the calculated values of F^* vs. α (not shown) were found to be in good agreement with those shown in Figure 4.12.

To investigate the relationship between F^* and Re_D, where Re_D is the Reynolds number based on the fiber diameter, the calculations were conducted for several values of Re_D and the results are shown in Figure 4.13. Similar to the case of rectangular fibers, the calculated values of F^* corresponding to $Re_D \leq 0.2$ were found nearly constant independent of Re_D while, for $0.2 < Re_D < 1$, the non-dimensional drag was found to increase slowly as the Reynolds number was increased.

Furthermore, the calculated values of F^* for various values of α and $Re \leq 0.2$ were compared with the theoretical results of Kuwabara as obtained from

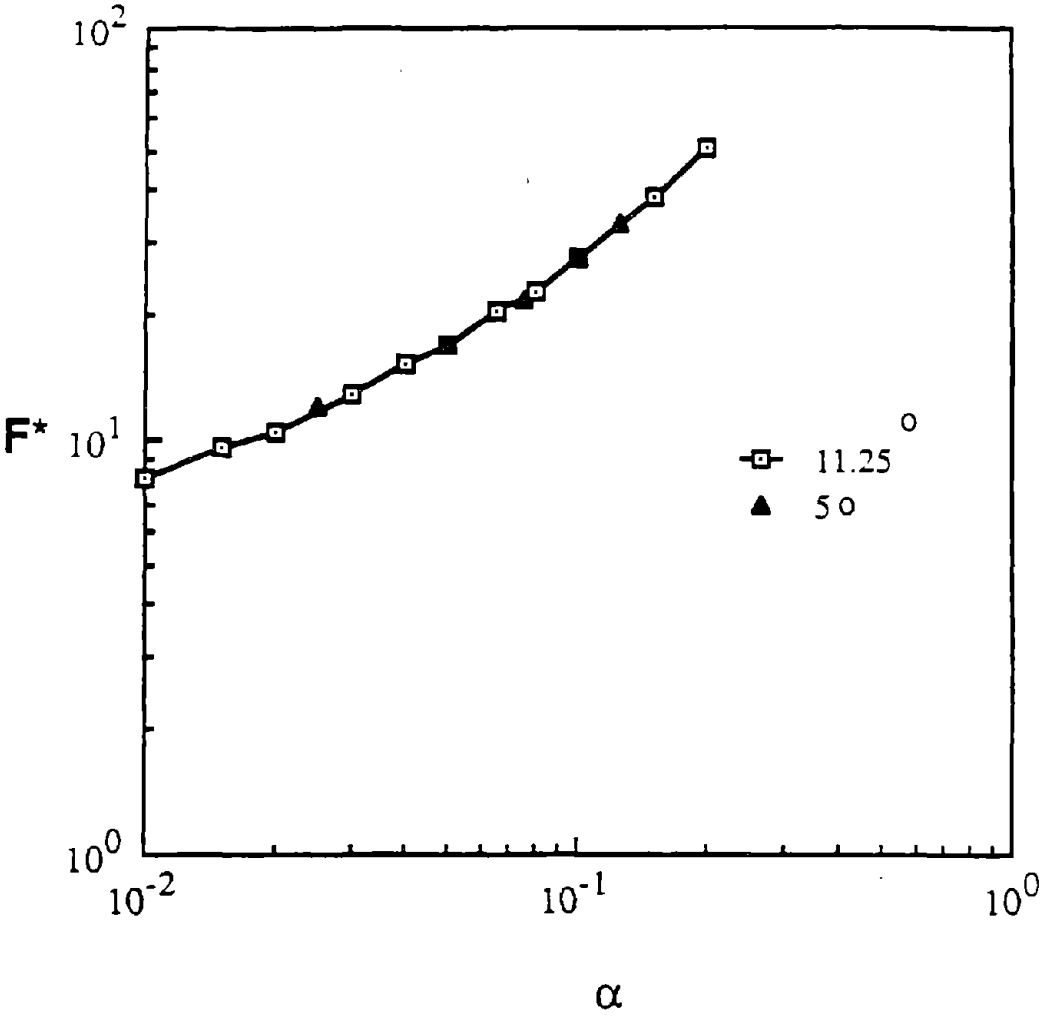

Figure 4.12 Effect of the step angle on the calculated values of the dimensionless drag on cylindrical fibers for several values of α

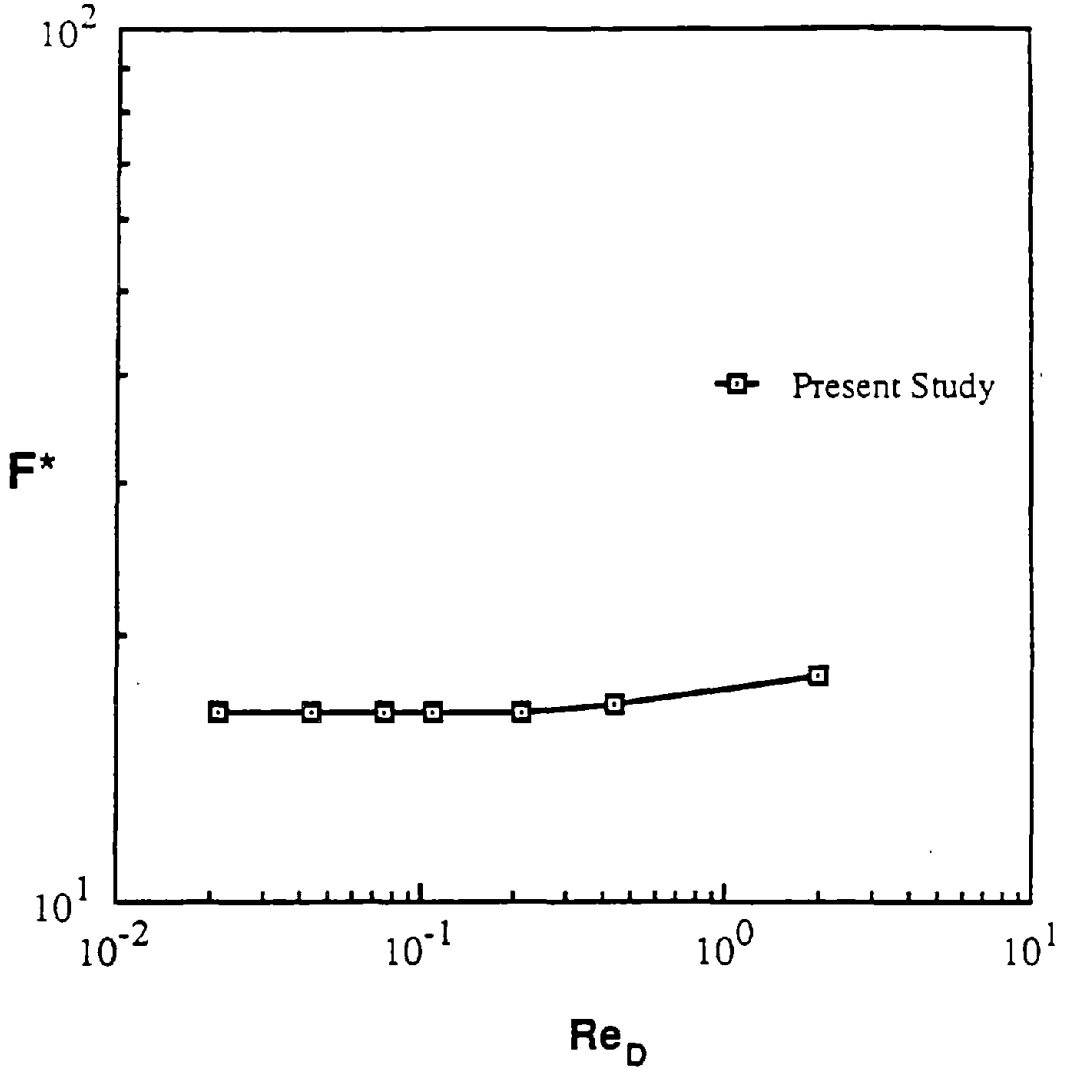

Figure 4.13 Effect of the viscous flow Reynolds number on the calculated values of the dimensionless drag on cylindrical fibers for a=0.05

equation (4.24). In addition, for the sake of comparison, the analytical results of Happel (1959) who obtained similar expression for F^* as that given by equation (4.24) except that his expression for the hydrodynamic factor expressed as following was different from that of Kuwabara (equation (2.41))

$$K = -0.5 \ln\alpha + \frac{\alpha^2}{1 + \alpha^2} - 0.5 \qquad \text{for } \alpha \ll 1 \qquad (4.69)$$

Figure 4.14 shows the comparison between the calculated values of F^* and those obtained from the analytical expression of Kuwabara and Happel. As can be seen, the agreement between the present calculated values and those of Kuwabara is very good, while the Happel's results are noticeably lower than both. The fact that the Kuwabara theory gives a better prediction of the flow field in a staggered array of circular fibers arranged normal to the flow than the Happel theory was verified also by the numerical work of Yeh (1972) and the experimental study of Kirsch and Fuchs (1967). In addition, the good agreement between the present results and those of Kuwabara attests to the accuracy and capability of the numerical technique used in the present study in determining the viscous flow field in a staggered array of symmetrically shaped fibers placed perpendicular to the flow.

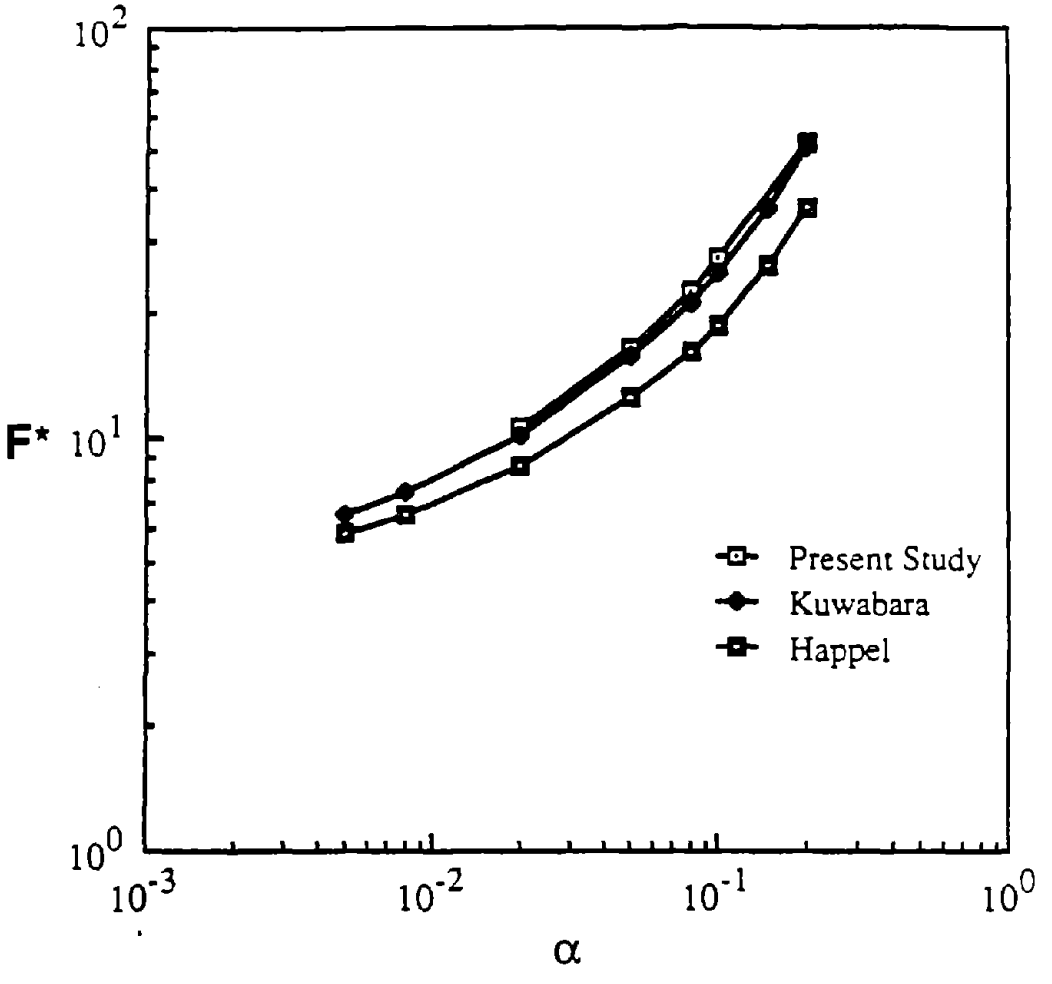

Figure 4.14 Comparison of the numerical and theoretical values of F^* on cylindrical fibers as respectively obtained in the present study and by Kuwabara and Happel

4.5 Dimensional Analysis of Viscous Drag on Rectangular Fibers

Although there is no analytical expression available for the drag on a rectangular fiber, one may obtain a functional relationship between F^* and other relevant dimensionless parameters using the Buckingham π-theorem (1915). The theorem states that in a physical problem including n quantities in which there are m dimensions, the quantities can be arranged into (n-m) independent dimensionless parameters. Let A_1, A_2, A_3, ...,A_n be the quantities involved which, for example, may represent pressure, viscosity, velocity, etc. If all the quantities are known to be essential to the solution of a problem then, there will have to exist some functional relationship between them, i.e.

$$F(A_1,A_2,A_3,\ldots,A_n) = 0 \qquad (4.41)$$

In that case if π_1, π_2, π_3 ,... represent dimensionless groupings of the quantities A_1, A_2, A_3, ..., then with n dimensions involved, an equation of the form

$$f(\pi_1,\pi_2,\pi_3,\ldots,\pi_{n-m}) = 0 \qquad (4.42)$$

can be written.

Let's apply the above theorem to the present problem. The quantities involved are Δp, μ, U_o, ρ, h, w, and b which have the following dimensions,

$$\Delta p : \frac{M}{LT^2} \tag{4.43a}$$

$$\mu : \frac{M}{LT} \tag{4.43b}$$

$$U_o : \frac{L}{T} \tag{4.43c}$$

$$\rho : \frac{M}{L^3} \tag{4.43d}$$

$$h : L \tag{4.43e}$$

$$b : L \tag{4.43f}$$

$$w : L \tag{4.43g}$$

where M, L, and T represent Mass, Length, and Time dimensions, respectively. Then, according to the theorem, there should exist $(7-3) = 4$ independent, dimensionless π parameters which could be formed from the above quantities.

The method of determining π parameters is to select $m = 3$ of the $n = 7$ quantities, with different dimensions, which contain among them the 3 basic dimensions (M, L, and T) and to use them as repeating variables together with one of the other quantities for each π. Let's choose Δp, h, and U_o as the repeating variables, which collectively contain M, L, and T in their dimension. Then, the first π parameter can

be formed as

$$\pi_1 = \Delta p^{x_1} h^{y_1} U_o^{z_1} \mu \tag{4.44}$$

the second one as

$$\pi_2 = \Delta p^{x_2} h^{y_2} U_o^{z_2} w \tag{4.45}$$

and the third and fourth ones as

$$\pi_3 = \Delta p^{x_3} h^{y_3} U_o^{z_3} b \tag{4.46}$$

$$\pi_4 = \Delta p^{x_4} h^{y_4} U_o^{z_4} \rho \tag{4.47}$$

since, by definition, the π's are dimensionless, the exponents of each equation can be determined by requiring that the right side of the equations must be dimensionless as well. Thus, by substituting the dimension of each quantity from equations (4.43a)-(4.43g) in the above equations, one obtains the following

$$M^0L^0T^0 = (ML^{-1}T^{-2})^{x_1} (L)^{y_1} (LT^{-1})^{z_1} (ML^{-1}T^{-1}) \tag{4.48}$$

$$M^0L^0T^0 = (ML^{-1}T^{-2})^{x_2} (L)^{y_2} (LT^{-1})^{z_2} (L) \tag{4.49}$$

$$M^0L^0T^0 = (ML^{-1}T^{-2})^{x_3} (L)^{y_3} (LT^{-1})^{z_3} (L) \tag{4.50}$$

$$M^0L^0T^0 = (ML^{-1}T^{-2})^{x_4} (L)^{y_4} (LT^{-1})^{z_4} (ML^{-3}) \qquad (4.51)$$

collecting the exponents of like dimensions on the right and setting them equal to zero would yield three equations in three unknowns for each parameter, which, when solved, give

$$x_1 = -1 \qquad y_1 = -1 \qquad z_1 = 1 \qquad (4.52)$$

$$x_2 = 0 \qquad y_2 = -1 \qquad z_2 = 0 \qquad (4.53)$$

$$x_3 = 0 \qquad y_3 = -1 \qquad z_3 = 0 \qquad (4.54)$$

$$x_4 = -1 \qquad y_4 = 0 \qquad z_4 = 2 \qquad (4.55)$$

Hence, the π parameters are

$$\pi_2 = \frac{U_o \mu}{\Delta p\, h} \; ; \quad \pi_2 = \frac{w}{h} \; ; \quad \pi_3 = \frac{b}{h} \; ; \quad \pi_4 = \frac{U_o^2 \rho}{\Delta p} \qquad (4.56)$$

which should satisfy the following

$$f\left(\frac{U_o \mu}{\Delta p\, h} \, , \, \frac{w}{h} \, , \, \frac{b}{h} \, , \, \frac{U_o^2 \rho}{\Delta p}\right) = 0 \qquad (4.57)$$

Moreover, the π's can be inverted, raised to any power, and/or multiplied by each other to obtain other forms as long as their number does not change. Thus, after a few simple inversion and multiplication operations on the above

π's, one obtains

$$f(\frac{\Delta p\ h}{U_o\ \mu}\ ,\ \frac{b}{w}\ ,\ \frac{w}{h}\ ,\ \frac{U_o\ \rho\ h}{\mu}) = 0 \qquad (4.58)$$

but according to equation (4.39), the first π parameter in the above equation is the dimensionless drag , F^*, and the fourth π parameter in equation (4.58) is the Reynolds number based on h as follows,

$$Re_h = \frac{\rho\ U_o\ h}{\mu} \qquad (4.59)$$

Therefore, equation (4.58) can be written as

$$f(F^*\ ,\ \frac{b}{w}\ ,\ \frac{w}{h}\ ,\ Re_h) = 0 \qquad (4.60)$$

which can be rearranged and expressed as following

$$F^* = g(\frac{b}{w}\ ,\ \frac{w}{h}\ ,\ Re_h) \qquad (4.61)$$

Meanwhile, the solid volume fraction, α, associated with the calculation domain of interest (Figure 4.4) is given by

$$\alpha = \frac{wb}{4h^2} \qquad (4.62)$$

which can also be written as

$$\alpha = \frac{w^2}{h^2} \cdot \frac{b/w}{4} \tag{4.63}$$

Rearranging the terms in this equation gives

$$\frac{w^2}{h^2} = \frac{4\alpha}{b/w} \tag{4.64}$$

Notice that the square of the second π parameter in equation (4.61) can be replaced by the above expression as follows,

$$F^* = g\left(\frac{b}{w} , \frac{4\alpha}{b/w} , Re_h\right) \tag{4.65}$$

multiplying the first and second π parameters together yields

$$F^* = G\left(\frac{b}{w} , \alpha , Re_h\right) \tag{4.66}$$

Note that the numerical coefficient of the second term in the right side of equation (4.65) has been ignored in the above equation since it has no meaning in this functional relationship. In addition, due to the functional nature of the above expression, replacement of Re_h with Re which is based on the hydraulic diameter of a rectangular fiber should not affect the relationship expressed by

equation (4.66). Therefore,

$$F^* = G(\frac{b}{w} , \alpha , Re) \qquad (4.67)$$

But as explained previously and shown in Figure 4.7, the calculated values of F^* were found to be independent of the Reynolds number for $Re \leq 0.2$. Therefore, the dependence of F^* on Re can be removed from equation (4.67) if the flow calculations are limited to values of the Reynolds number below or in the vicinity of 0.2 . Hence,

$$F^* = H(\frac{b}{w} , \alpha) \qquad \text{if } Re \leq 0.2 \qquad (4.68)$$

This indicates that the dimensionless drag on a rectangular fiber due to the flow of a viscous fluid over the fiber is a function of both the filter packing density and aspect ratio of the fiber in comparison to the case of a cylindrical fiber for which the dimensionless drag is a function of the filter packing density only (equation (4.24)).

A graphical representation of F^* as a function of α for several values of $\frac{b}{w}$ has been obtained and will be presented and discussed later.

4.6 Formulation of the Single Electret Fiber Collection Efficiency

Once the flow field around a typical fiber is known, one can determine the single fiber capture efficiency of particles due to various collection mechanisms. The mechanisms considered in the present study are Brownian diffusion, interception, and electrostatic effect while, the effects of gravity and particle inertia have been neglected. Below, a description of each collection mechanism considered and a procedure for calculating corresponding single fiber efficiency are presented.

4.6.1 Brownian Diffusion

One of the major particle collection mechanisms by fibers of a fibrous filter, especially for submicron particles, is the Brownian diffusion which arises from diffusion of particles towards fibers as a results of their random motion caused by their interaction with molecules of the carrier gas.

Let's consider an infinitesimal control volume across which particles can be transported by convection and diffusion. The general convective-diffusion equation expressing the conservation of number of particles in the

control volume can be written as

$$\frac{\partial N}{\partial t} = - \text{div}(-D \nabla N) - \text{div}\, \bar{u} N - \text{div}(\bar{v}_p - \bar{u}) N \qquad (4.70)$$

where the barred parameters denote vector quantities. In this equation, N is the particle concentration, D is the diffusion coefficient of particles which can be determined from the Einstein's equation assuming Stoke's law for the particle drag

$$D = \frac{f T c}{3\pi\mu d_p} \qquad (4.71)$$

T is the temperature and f is the Boltzmann's constant, $\bar{u}$ is the gas velocity, and $\bar{v}_p$ is the particle velocity which can be different from the gas velocity if the particle is under the influence of external forces such as inertia, gravity, and electrostatic forces, and ∇ is the differential operator. Note that equation (4.70) basically expresses a balance between the rate of accumulation of particles in the control volume as represented by the term on the left and the net rates of particle transport into the control volume due to Brownian diffusion, exchange of fluid of the control volume with surroundings, and particle transport resulting from the relative motion between particles and the ambient as represented, respectively, by the terms on the right side

of the equal sign. Under steady state conditions and in the absence of any external forces, equation (4.70) can be simplified as

$$\nabla \cdot (N\bar{u}) = D \nabla^2 N \tag{4.72}$$

or

$$N(\nabla \cdot \bar{u}) + (\bar{u} \cdot \nabla)N = D \nabla^2 N \tag{4.73}$$

where for the two dimensional cartesian coordinate system considered here, ∇^2 can be expressed as

$$\nabla^2 = \frac{\partial^2}{\partial x^2} + \frac{\partial^2}{\partial y^2} \tag{4.74}$$

but from equation (4.25),

$$\nabla \cdot \bar{u} = 0$$

hence, equation (4.73) can be written as

$$(\bar{u} \cdot \nabla)N = D \nabla^2 N \tag{4.75}$$

or in expanded form as,

$$u\frac{\partial N}{\partial x} + v\frac{\partial N}{\partial y} = D \left(\frac{\partial^2 N}{\partial x^2} + \frac{\partial^2 N}{\partial y^2}\right) \tag{4.76}$$

Note that this equation simply states that the net rate of the particle transport by the gas flow (convection) out of

the control volume is equal to the net rate of particle transport by diffusion into the volume.

If the flow field around a typical fiber is known, one can solve equation (4.76) subject to appropriate boundary conditions to determine the distribution of particle concentration around the fiber, from which the diffusion rate of particles towards the fiber can be calculated. In the case of rectangular fibers, however, one can only obtain a numerical solution since the flow field can not be expressed analytically. Using the same numerical technique used for solution of the flow equations, equation (4.76) can be solved numerically in a calculation module identical to that used for the flow calculations. Referring to module ABEF shown in Figure 4.4, the boundary conditions assumed for the particle concentration are as follows,

inflow boundary : $$N = N_o \qquad (4.77)$$

top and bottom boundaries : $$\frac{\partial N}{\partial y} = 0 \qquad (4.78)$$

outflow boundary : $$\frac{\partial N}{\partial x} = 0 \qquad (4.79)$$

on the fiber : $$N = 0 \qquad (4.80)$$

where N_o is an arbitrary constant. Therefore, a uniform particle concentration is assumed at the domain entrance while, symmetry conditions are assumed at the top and bottom boundaries. Note also the symmetry-like condition considered

at the outflow boundary where there is no information known about the particle concentration. As described by Patankar (1980), the neglect of diffusion at the outflow boundary is a way of eliminating the effect of unknown conditions at that boundary on the rest of the domain. More discussion on the implication of this assumption is given in Appendix C. It should be mentioned also that one could have used a modified periodicity condition for the particle concentration at the inflow and outflow boundaries of the domain but that idea was abondoned here because of introduction of unnecessary complications to the calculation of the single fiber efficiency.

The calculation program for solution of equation (4.76) has been described in Appendix C. To start the calculations, the program requires the input of the previously calculated flow field corresponding to the desired values of the fiber aspect ratio and filter packing density as well as a value for the diffusion coefficient of particles. The calculation of discrete values of particle concentration in the domain under consideration then begins iteratively and continues until a converged solution is attained.

Once the particle concentration profile around the fiber is determined, one can calculate the rate of particle

diffusion to the fiber by using Fick's law,

$$j = - D \frac{\partial N}{\partial n} \tag{4.81}$$

where j is the particle flux defined as the number of particles depositing on the fiber per unit area per unit time, and n is the coordinate pointing in the direction of the vector normal to the fiber surface. Due to the numerical nature of the solution, The value of j for each control volume adjacent to the fiber was approximated by the following equation

$$j = - D \frac{\Delta N}{\Delta n} \tag{4.82}$$

notice that equations (4.81) and (4.82) yield similar results if the concentration profile is linear in proximity of the fiber. In fact, the slope of the calculated concentration profile in the fine mesh around the fiber was found to be constant for the cases where the diffusion boundary layer thickness, δ, was relatively large. For other cases where δ was of the same order of magnitude as the thickness of the fine mesh around the fiber, the calculated concentration profile was found to be non-linear and as a result, the error associated with using equation (4.82) was reflected in the calculated values of the single fiber

efficiency as will be presented and discussed in the next chapter. Of course, one can reduce the magnitude of the error by further shrinking the size and/or increasing the number of the control volumes in the region very close to the fiber, but that, in turn, would retard the convergance rate and increase substantially the computation time and cost.

The total number of particles deposited on the fiber per unit time by diffusion, J, was then determined by

$$J = \sum_{i=1}^{M} j_i A_i \qquad (4.83)$$

where A_i is the surface area of that face of the control volume i which is perpendicular to the normal vector of the fiber, and M is the total number of control volumes adjacent to the fiber. The results, however, are usually expressed in terms of the single fiber capture efficiency defined as

$$\eta_D = \frac{J}{u_o N_o d} \qquad (4.84)$$

where d is a characteristic length depending on the fiber shape. For circular fibers, d is equal to the fiber radius and for rectangular fibers, it is equal to the half width of the fiber or half the side which is facing normal to the

flow direction. The values of η_D for different values of the rectangular fiber aspect ratio, $\frac{b}{w}$; the fiber volume fraction, α ; and the diffusion coefficient, D (or the Peclet number) were calculated and the results will be illustrated and discussed in the next chapter.

4.6.2 Interception

Another important particle capture mechanism is interception which accounts for the finite size of particles. When a particle comes to a distance equal or less than its radius from surface of a fiber, it is intercepted and thus collected by the fiber.

Interception is usually important for a particle size which is neither too small for diffusion nor too large for the inertial impaction to become dominant. Whether or not the interception effect should be considered in the filtration studies is decided based on the value of the interception parameter, N_R, which is defined as

$$N_R = \frac{a_p}{a_f} \tag{4.85}$$

for circular fibers and

$$N_R = \frac{a_p}{w/2} \tag{4.86}$$

for rectangular fibers. For $N_R << 1$, the interception effect is often neglected in the calculation of the over-all fiber collection efficiency. But when considered, the interception effect is usually combined with other collection mechanisms. The resulting filter efficiency will be then due to the simultaneous action of interception and any other collection mechanism considered. However, in the present study, the interception effect for rectangular fibers was treated alone, independent of other collection mechanisms. Meanwhile, in the absence of the Brownian diffusion and external forces, a particle in a gas flow through a filter travels along the fluid streamlines and will come in contact with a fiber if the streamline, along which the particle is travelling, approaches within a distance equal to the particle radius from surface of the fiber. Hence, there must exist a critical streamline below which all particles carried by the gas flow are collected by the fiber and above which particles travel around the fiber and are not intercepted by the fiber. Figure 4.15 shows the situation pictorially. The collection efficiency of the fiber due to interception, η_R, is then simply the ratio of the gas flow rate confined between the critical and

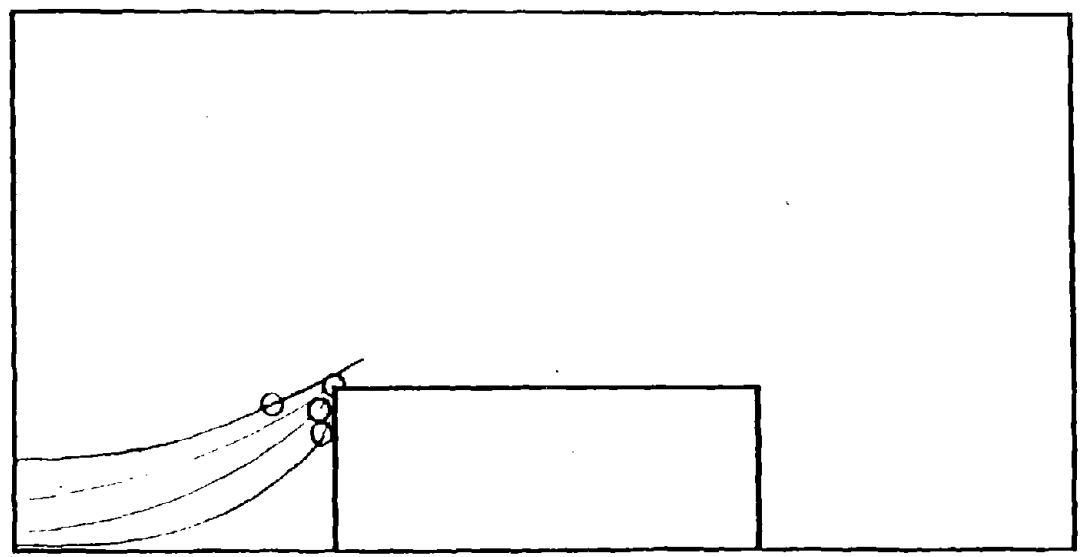

Figure 4.15 Interception of particles of diameter a_p by a rectangular fiber as they come to within a distance of one particle radius from surface of the fiber

stagnation streamlines determined as the difference between values of the stream function associated with the two streamlines to the total flow rate intercepted by the fiber, had the flow not been deflected by the presence of the fiber. Thus, η_R can be written as

$$\eta_R = \frac{2\psi_{cr}}{U_o w} \tag{4.87}$$

where ψ_{cr} is the streamline value of the critical streamline having assumed a zero value for the stagnation streamline.

To determine ψ_{cr} from the numerical results for the flow field around a rectangular fiber, let's consider Figure 4.16 illustrating the familiar calculation domain with the fiber enclosed by an imaginary rectangular cell which is the locus of points being one particle radius away from surface of the fiber. Notice that the cell has two 90^o arcs with their centers located at two corners of the fiber.

The critical streamline must then come tangent to the cell at two points which are more likely to be on the arcs. The plan is therefore to calculate the flow rate between the stagnation streamline and several locations on the imaginary cell including the arcs and choose the maximum flow rate as the value for the critical streamline.

Although, the fluid velocity components on the cell can be approximated from the calculated flow field obtained in the

absence of the imaginary cell, but the results will be more accurate if the flow calculations are repeated with the presence of the imaginary cell taken into account.

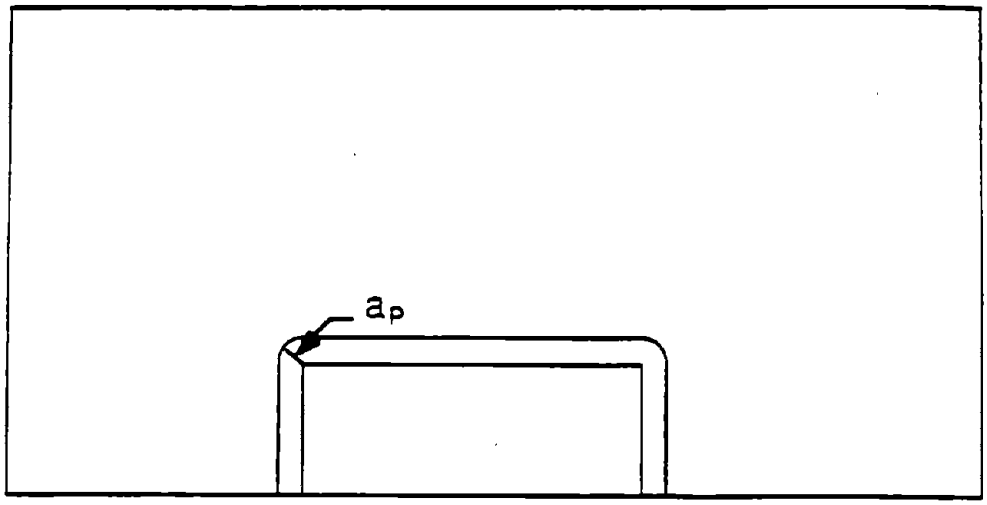

Figure 4.16 Imaginary interception region around a rectangular fiber, which is one particle radius from surface of the fiber

This, of course, requires the circular arcs to be approximated by steps as described previously in the case of flow calculations around circular fibers. Figure 4.17 shows the left arc as approximated by steps. A step angle of 11.25^{o} was used for generating the steps.

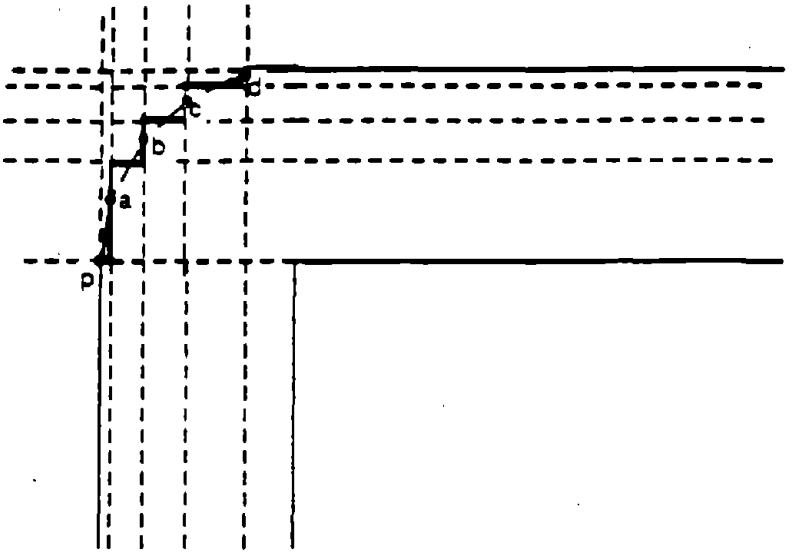

Figure 4.17 "Step" representation of particle interception arc of radius a_p with a step angle of 11.25 degrees

The flow field was calculated for $Re < 0.2$ and several values of N_R, α, and $\frac{b}{w}$. The calculated velocity components in the x- direction were used to determine the volume flow rate confined between the stagnation streamline and each one of the points a, b, c, and d on the arc. The maximum flow rate was often found to correspond to point c and at times to point b depending on the fiber aspect ratio and value of N_R. The angular positions of points b and c on the arc are 3×11.25^{o} and 5×11.25^{o}, respectively, as measured clockwise from point P.

It should be mentioned that a more precise calculation of the value of the limiting streamline and its location on the arcs requires the use of finer steps in approximating the arcs which, in turn, will increase greatly the computation time. But due to the small radius of curvature of the arcs, an increase in number of steps is unlikely to improve the results by any significant amount.

The calculation of the single fiber efficiency due to interception was made for several rectangular fibers with $\frac{b}{w}$ ranging from $\frac{1}{2}$ to 10 and for $0.1 \leq N_R < 1$ and α = 0.04, 0.08, and 0.16. The results are presented and discussed in the next chapter.

4.6.3 Electrostatics

As described previously, electret fibers are best characterized by their rectangular cross-section and bipolar charges on two opposite sides of the rectangle. The charges are not the so called "free" charges but instead are permanent dipoles induced during manufacturing as explained previously. The electric field intensity function in and around a typical electret fiber can be obtained from the solution of the Poisson's equation using the specified surface charge distribution as one of the boundary conditions. Such approach, however, is mathematically quite

complicated and as a result until recently, almost all studies involving electret fibers have been experimental and any theoretical work such as that of Brown (1981) on the electret fibers considers circular instead of rectangular fibers since the viscous flow and electric fields around a cylinder with permanent dipoles are known. Recently, however, the Japanese investigators (Emi etal. (in press)) have started both experimental and theoretical work on electrostatic collection efficiency of rectangular electret fibers. Their approach to expressing the electric field intensity around an electret fiber was to approximate the effect of bipolar charges by that of many line charges of both polarities placed uniformly along two opposite sides of the fiber. The electric field intensity around the fiber was then assumed to be equal to the vectorial sum of intensity of all line charges. Meanwhile, the flow field around the fiber was approximated by that around an isolated elliptic body with zero thickness for which analytical solutions are available. The results of the Japanese work were presented in Chapter 2.

The concept of approximating the electric field intensity around an electret fiber by that due to the net effect of several line charges of both polarities was also used in the present study to determine the electrostatic single fiber efficiency due to Coulombic and inductive

interactions between paticles and the electret fiber.

It should be mentioned, however, that the effect of the polarization field within the fiber on its surrounding electric field is completely neglected and therefore, the dielectric constant of the fiber does not play any role in the formulation of the electric field intensity around the fiber as presented below. Although, such consideration limits the application of the results to the real problems but, as a first order approximation, it will provide some insight into the collection capabilities of electret fibers due to electrostatic forces.

The present study, however, differs from the theoretical study of Japanese in two aspects. One is that the flow field used in the present study is indeed that around a rectangular fiber as opposed to the approximated flow field used by the Japanese. The second difference is the inclusion of the interference effect of neighboring fibers on the flow field around a typical fiber in the present study in contrast with the isolated-fiber model considered by the Japanese. It should be emphasized that the interfernce effects were considered only in the flow field calculations and were not taken into account in the formulation of the electric field around a typical fiber .

Figure 4.18 shows the cross-section of an electret

fiber with positive and negative line charges representing the polarized charges on two opposite surfaces of the fiber.

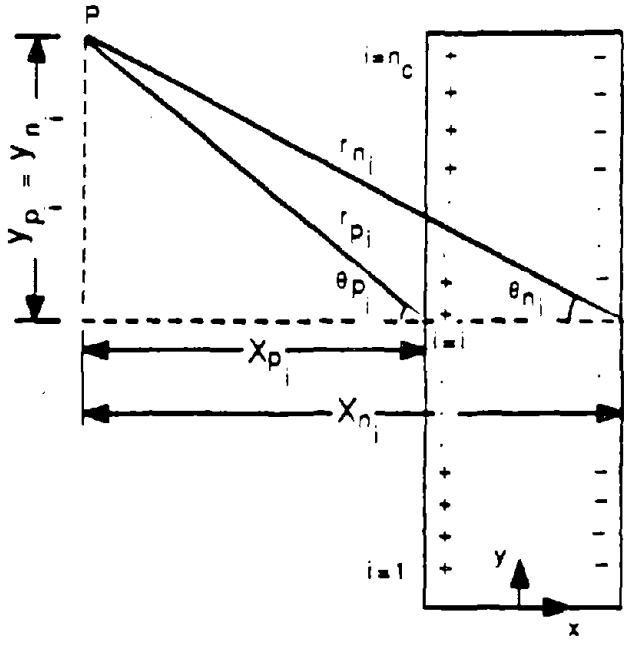

Figure 4.18 Distribution of dipoles on an electret fiber, approximated by pairs of positive and negative line charges

The radial electric field intensity, E_{r_i}, at a point due to the combined effect of a pair of positive and negative line charges as designated by i can be written as

$$E_{r_i} = \frac{Q}{2\pi\epsilon_o r_{p_i}} - \frac{Q}{2\pi\epsilon_o r_{n_i}} \qquad (4.88)$$

where ϵ_o is the permittivity of free space, Q is the amount of charge per unit length of each line charge, and r_{p_i} and

r_{n_i} are shown in Figure 4.18. The angular field intensity around a line charge is zero due to symmetry consideration. Since, a more appropriate coordinate system for the present problem is the cartesian coordinate system, it is best to express the electric field intensity in terms of its cartesian components, E_{x_i} and E_{y_i}, as follows

$$E_{x_i} = \frac{Q}{2\pi\epsilon_o r_{p_i}} \cos\theta_p - \frac{Q}{2\pi\epsilon_o r_{n_i}} \cos\theta_n \tag{4.89}$$

$$E_{y_i} = \frac{Q}{2\pi\epsilon_o r_{p_i}} \sin\theta_p - \frac{Q}{2\pi\epsilon_o r_{n_i}} \sin\theta_n \tag{4.90}$$

where angles θ_p and θ_n are also shown in Figure 4.18. Using simple trignometry relations, the above equations can be written as

$$E_{x_i} = \frac{Qx_{p_i}}{2\pi\epsilon_o r^2_{p_i}} - \frac{Qx_{n_i}}{2\pi\epsilon_o r^2_{n_i}} \tag{4.91}$$

$$E_{y_i} = \frac{Qy_{p_i}}{2\pi\epsilon_o r^2_{p_i}} - \frac{Qy_{n_i}}{2\pi\epsilon_o r^2_{n_i}} \tag{4.92}$$

where

$$r^2_{p_i} = x^2_{p_i} + y^2_{p_i} \tag{4.93a}$$

$$r^2_{n_i} = x^2_{n_i} + y^2_{n_i} \tag{4.93b}$$

with x and y distances shown in Figure 4.18. Considering the

effect of all line charges, the components of the net electric field intensity, E_x and E_y , at the point under consideration can be written as

$$E_x = \sum_{i=1}^{n_c} \left[\frac{Qx_{p_i}}{2\pi\epsilon_o r_{p_i}^2} - \frac{Qx_{n_i}}{2\pi\epsilon_o r_{n_i}^2}\right] \tag{4.94}$$

$$E_y = \sum_{i=1}^{n_c} \left[\frac{Qy_{p_i}}{2\pi\epsilon_o r_{p_i}^2} - \frac{Qy_{n_i}}{2\pi\epsilon_o r_{n_i}^2}\right] \tag{4.95}$$

where n_c is the total number of line charges of each polarity assumed on the fiber. Equations (4.94) and (4.95) describe the electric field intensity around a typical electret fiber whose surface bipolar charge distribution is approximated by several line charges of both polarities.

Having obtained the electric field intensity function, one can determine the magnitude of electrostatic forces acting on charged or uncharged particles approaching an electret fiber.

In the case of a charged particle, the electric force on the particle is Coulombic given by the following vectorial expression

$$\bar{F}_C = q\bar{E} \tag{4.96}$$

where q is the particle charge and $\bar{F}_C$ is the Coulombic force

Expressing the above equation in terms of its x- and y-components gives

$$F_{C_x} = qE_x \tag{4.97}$$

$$F_{C_y} = qE_y \tag{4.98}$$

where F_{C_x} and F_{C_y} are components of the Coulombic force in the x- and y- directions and E_x and E_y are given by equations (4.94) and (4.95), respectively.

In the case of an uncharged particle in an inhomogeneous electric field, the particle becomes polarized and is attracted towards region of higher intensity, i.e., towards the fiber. The electrostatic force acting on the particle, in general, is given by

$$\bar{F}_I = \frac{\pi D_p^3 \epsilon_o}{4} \cdot \frac{\kappa - 1}{\kappa + 2} \nabla (E^2) \tag{4.99}$$

where $\bar{F}_I$ is the induced force, D_p and κ are the particle diameter and dielectric constant, respectively, and $\nabla = \hat{i}\frac{\partial}{\partial x} + \hat{j}\frac{\partial}{\partial y}$ is the differential operator with $\hat{i}$ and $\hat{j}$ denoting the unit vectors in the x- and y- directions, respectively. Expressing the above equation in terms of its components and substituting for E_x and E_y from equations (4.94) and (4.95), respectively, results in the following

expresssions for the induction force components, F_{I_x} and F_{I_y}

$$F_{I_x} = \sum_{i=1}^{n_c} - \frac{Q^2 D_p^3}{8\pi\epsilon_o} \frac{\kappa - 1}{\kappa + 2} \left[\frac{x_{p_i}}{r_{p_i}^4} - \frac{x_{n_i}}{r_{n_i}^4}\right] \qquad (4.100)$$

$$F_{I_y} = \sum_{i=1}^{n_c} - \frac{Q^2 D_p^3}{8\pi\epsilon_o} \frac{\kappa - 1}{\kappa + 2} \left[\frac{y_{p_i}}{r_{p_i}^4} - \frac{y_{n_i}}{r_{n_i}^4}\right] \qquad (4.101)$$

But the electrostatic forces are not the only forces acting on a particle carried by the fluid flow around an electret fiber as other external forces such as inertia, gravity, and drag may be significant also. However, The influence of particle inertia and gravity were neglected in the present study. Thus, under steady state conditions, the electrostatic force acting on a particle is balanced by the drag on the particle as follows,

$$\bar{F}_C = \bar{F}_d \qquad (4.102)$$

for the case of a charged particle and

$$\bar{F}_I = \bar{F}_d \qquad (4.103)$$

for the case of an uncharged particle.

The drag on a particle, $\bar{F}_d$, can be expressed by the

following equation assuming Stoke s' law for the particle drag,

$$\bar{F}_d = \frac{3\pi\mu D_p}{c} (\bar{u} - \bar{v}_p) \qquad (4.104)$$

where $\bar{u}$ is the fluid velocity, and $\bar{v}_p$ is the particle velocity which is different from $\bar{u}$ due to the influence of electrostatic forces. Again, expressing $\bar{F}_d$ in terms of its components yields

$$F_{dx} = \frac{3\pi\mu D_p}{c} (u - v_{px}) \qquad (4.105)$$

$$F_{dy} = \frac{3\pi\mu D_p}{c} (v - v_{py}). \qquad (4.106)$$

where v_{px} and v_{py} are components of the particle velocity in the x- and y- directions, respectively .

Equating like components of the drag and electrostatic forces according to equations (4.102) and (4.103) for charged and uncharged particles and solving for the components of the particle velocity for each case, one obtains the following relationships. For the case of a charged particle,

$$v_{px} = u - \sum_{i=1}^{n_c} \frac{Qqc}{6\pi^2\epsilon_o\mu D_p} \left[\frac{x_{p_i}}{r_{p_i}^2} - \frac{x_{n_i}}{r_{n_i}^2}\right] \qquad (4.107)$$

$$v_{py} = v - \sum_{i=1}^{n_c} \frac{Qqc}{6\pi^2\epsilon_o\mu D_p} \left[\frac{y_{p_i}}{r_{p_i}^2} - \frac{y_{n_i}}{r_{n_i}^2}\right] \qquad (4.108)$$

while, for the case of an uncharged particle,

$$v_{px} = u - \sum_{i=1}^{n_c} \frac{Q^2 D_p^2 c}{24\pi^2\epsilon_o\mu} \frac{\kappa - 1}{\kappa + 2} \left[\frac{x_{p_i}}{r_{p_i}^4} - \frac{x_{n_i}}{r_{n_i}^4}\right] \qquad (4.109)$$

$$v_{py} = v - \sum_{i=1}^{n_c} \frac{Q^2 D_p^2 c}{24\pi^2\epsilon_o\mu} \frac{\kappa - 1}{\kappa + 2} \left[\frac{y_{p_i}}{r_{p_i}^4} - \frac{y_{n_i}}{r_{n_i}^4}\right] \qquad (4.110)$$

Considering the number of parameters involved in equations (4.107)-(4.110), it is best to express the equations in non-dimensional form by introducing the following parameters

$$u^* = \frac{u}{U_o} \qquad v_{px}^* = \frac{v_{px}}{U_o}$$

$$v^* = \frac{v}{U_o} \qquad v_{py}^* = \frac{v_{py}}{U_o}$$

$$x^* = \frac{x}{w} \qquad y^* = \frac{y}{w} \qquad r^* = \frac{r}{w} \qquad (4.111)$$

where * quantities are dimensionless. Substituting the above in equations (4.107)-(4.110) and simplifying, one obtains

$$v^*_{px} = u^* - N_C \cdot \sum_{i=1}^{n_c} \left[\frac{x^*_{p_i}}{r^{*2}_{p_i}} - \frac{x^*_{n_i}}{r^{*2}_{n_i}}\right] \tag{4.112}$$

$$v^*_{py} = v^* - N_C \cdot \sum_{i=1}^{n_c} \left[\frac{y^*_{p_i}}{r^{*2}_{p_i}} - \frac{y^*_{n_i}}{r^{*2}_{n_i}}\right] \tag{4.113}$$

for charged particles and

$$v^*_{px} = u^* - N_I \cdot \sum_{i=1}^{n_c} \left[\frac{x^*_{p_i}}{r^{*4}_{p_i}} - \frac{x^*_{n_i}}{r^{*4}_{n_i}}\right] \tag{4.114}$$

$$v^*_{py} = v^* - N_I \cdot \sum_{i=1}^{n_c} \left[\frac{y^*_{p_i}}{r^{*4}_{p_i}} - \frac{y^*_{n_i}}{r^{*4}_{n_i}}\right] \tag{4.115}$$

for uncharged particles. In these equations, N_C and N_I are dimensionless force parameters expressing the ratio of coulombic and induction forces, respectively, to the drag force and are defined as

$$N_C = \frac{Qqc}{6\pi^2\epsilon_o\mu D_p w U_o} \tag{4.116}$$

$$N_I = \frac{Q^2 D_p^3 c}{24\pi^2\epsilon_o\mu w^3 U_o} \frac{\kappa - 1}{\kappa + 2} \tag{4.117}$$

In addition, the dimensionless particle velocity components

can be written in terms of differential rate of particle displacement as follows,

$$v^*_{px} = \frac{dx^*_p}{dt^*} \tag{4.118}$$

$$v^*_{py} = \frac{dy^*_p}{dt^*} \tag{4.119}$$

where $t^* = \frac{t}{w/U_o}$ and x^*_p and y^*_p are dimensionless coordinates of the position of a particle in the space around an electret fiber at a given time.

Equations (4.118) and (4.119) along with equations (4.112) and (4.113) or (4.114) and (4.115), depending on the charging state of the particle under consideration, constitute the particle trajectory equations which can be integrated with respect to the dimensionless time parameter to determine the position of the particle with respect to the fiber. One can then determine whether or not the particle is captured by the fiber and thereby calculate the single fiber collection efficiency due to the influence of electrostatic forces. To carry on such calculations, however, requires knowledge of the flow field around a rectangular fiber which was obtained numerically in the present study for various aspect ratios of the fiber. Considering the familiar calculation domain ABEF as shown in

Figure 4.4, the calculated velocity components corresponding to given values of the fiber aspect ratio and filter packing density are used to integrate the particle trajectory equations by the Runga-Kutta method. A detailed description of the Runga-Kutta method and the program developed for the particle trajectory calculations is presented in Appendix D.

A typical trajectory calculation can be briefly described as follows: a particle is introduced into the calculation domain from a known location on the inflow boundary of the domain. Its displacement in the domain can be followed by the results of succesive integrations of its trajectory equations. Consequently, the particle either collides with the fiber or leaves the domain uncaptured. Hence, there must exist a critical trajectory such that all particles entering the domain at y-coordinates below that of the critical trajectory will be captured by the fiber whereas, those entering the domain at locations above the starting y-coordinate of the critical trajectory will not be captured. It is the objective of the present study to determine the starting y-coordinate of the critical trajectory for given values of the parameters involved.

The electrostatic single fiber efficiency can be then defined as

$$\eta_E = \frac{2y_c}{w} \qquad (4.120)$$

where η_E is the single fiber efficiency due to electrostaic forces and y_c is the starting y-coordinate of the particle critical trajectory. Notice that y_c can not be determined exactly but it can be approximated with great accuracy as the average of starting y-coordinates of two particle trajectories corresponding to the cases of capture and no-capture.

The results of the single fiber efficiency calculations for both Coulombic and Induced force interactions are presented and discussed in the next chapter.